THERMAL INSTABILITIES IN THE SOLAR CORONA
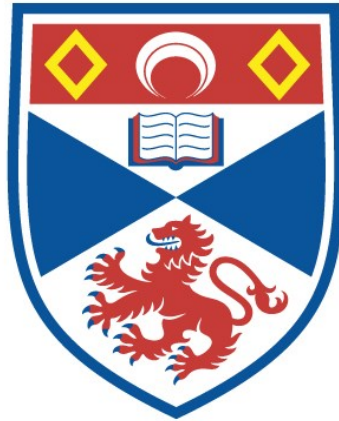
Richard C. Ireland

A Thesis Submitted for the Degree of PhD
at the
University of St Andrews

1995

Thermal Instabilities in the Solar Corona.

Richard C. Ireland.

Thesis submitted for the degree of Doctor of Philosophy of the
University of St. Andrews.
June 27th 1994.

Abstract

In this thesis, several problems relating to thermal instabilities in the solar corona are examined. Chapter 1 gives a brief description of the Sun and corresponding events with particular attention focused on prominences, their formation and eruption. Various problems concerning thermal instabilities are then tackled in the later Chapters.

In Chapter 2, the basic MHD equations are introduced and a physical description of the thermal instability mechanism given. The MHD equations are linearised in a uniform, infinite medium and the basic instability criteria obtained.

Chapter 3 investigates the normal mode spectrum for the linearised MHD equations for a cylindrical equilibrium. This spectrum is examined for zero perpendicular thermal conduction, with both zero and non-zero scalar resistivity. Particular attention is paid to the continuous branches of this spectrum, or continuous spectra. For zero resistivity there are three types of continuous spectra present, namely the Alfvén, slow and thermal continua. It is shown that when dissipation due to resistivity is included, the slow and Alfvén continua are removed and the thermal continuum is shifted to a different position (where the shift is independent of the exact value of resistivity). The 'old' location of the thermal continuum is covered by a dense set of nearly singular discrete modes called a quasi-continuum, for equilibria with the thermal time scale much smaller than the Alfvén time scale. This quasi-continuum is investigated numerically and the eigenfunctions are shown to have rapid spatial oscillating behaviour. These oscillations are confined to the most unstable part of the equilibrium based on the Field criterion and may be the cause of fine structure in prominences.

In Chapter 4, the normal mode spectrum for the linearised MHD equations is examined for a plasma in a cylindrical equilibrium. The equations describing these normal modes are solved numerically using a finite element code. In the ideal case the Hain-Lüst equation is expanded and a WKB solution obtained for large axial wave numbers. This is compared to the numerical solutions. In the non-ideal case, the ballooning equations describing localised modes are manipulated in an arcade geometry and a dispersion relation derived. It is illustrated that as the axial wave number k is increased, the fundamental thermal and Alfvén modes can coalesce to form overstable magnetothermal modes. The ratio between the magnetic and thermal terms is varied and the existence of the magnetothermal modes examined. The corresponding growth rates are predicted by a WKB solution to the ballooning equations. The interaction of thermal and magnetic instabilities and the existence of these magnetothermal modes may be significant in the eruption of prominences into solar flares.

Chapter 5 extends the work presented in Chapter 4 to include the effects of line-tying in a coronal arcade. The ballooning equations which were introduced in Chapter 4 are manipulated to give a dispersion relation. This relation is a quadratic in the square of the azimuthal wave number m if parallel thermal

conduction is neglected and a cubic in m^2 if parallel conduction is included. Rigid wall boundary conditions are applied to this dispersion relation. This dispersion relation is then solved numerically subject to these boundary conditions and the solutions plotted. Unfortunately the expression for the thermal continuum in line-tied arcades is required since the thermal continuum must play an important role in the proceedings. This calculation is left for future work.

From the results obtained, it can be seen that the thermal instability can play a major part in prominence formation and destruction. The thermal instability may help create the prominence. Resistivity and perpendicular thermal conduction can cause of the observed fine scale structure. Finally, a neighbouring thermal instability may trigger a magnetic instability that causes the prominence to erupt.

Contents

Declarations

In accordance with the regulations of the University of St. Andrews as of June 1994,

1. I, Richard Clive Ireland, hereby certify that this thesis has been composed by myself, that it is a record of my own work and that it has not been accepted in partial or complete fulfilment of any other degree or professional qualification.

   Signed: Date: 5/9/94

2. I was admitted to the Faculty of Science of the University of St. Andrews under Ordinance General No 12 in October 1990 and as a candidate for the degree of Ph.D. on the same date.

   Signed: Date: 5/9/94

3. I hereby certify that the candidate has fulfilled the conditions of the Resolution and Regulations appropriate to the Degree of Ph.D.

   Signed: Date: 5/9/94

4. In submitting this thesis to the University of St. Andrews I understand that I am giving permission for it to be made available for use in accordance with the regulations of the University Library for the time being in force, subject to any copyright vested in the work not being affected thereby. I also understand that the title and abstract will be published and that a copy of the work may be made and supplied to any *bona fide* library or research worker.

Acknowledgements

Chapter 1

A Brief Description of the Sun

...and the silly American said to me, just as we were coming up to this roundabout, 'Do these things understeer or oversteer?' and I said, 'Well I'll show you on this roundabout. You can make it understeer like this, (and we went round the first roundabout), or you can make it oversteer like this.' And he was completely silent after that!

-Tim Fry, demonstrating Hillman Imp handling to the Americans.

1.1 Introduction

In this Chapter, a brief description of the Sun and corresponding events is presented with particular attention focused on prominences and their formation. Various problems relating to prominences are then tackled in the later Chapters. Throughout the history of astrophysics, the Sun has been widely regarded as an uninteresting object, particularly in comparison with beauty of the many galaxies and constellations visible in the night sky. In 350 BC Theophrastus, a pupil of Aristotle, observed a sunspot with the naked eye but, it was not until 1843, that Schwabe proposed the existence of an eleven year cycle for the frequency of sunspot occurrence. It is fair to say that before the 18th century, little was known about the Sun.

Since then, the Sun has been of great interest to many astronomers and astrophysicists. In particular, during the last 50 years numerous discoveries have been made. Many satellites have been launched (for example Skylab) for the purpose of observing the Sun and more are being planned (SOHO, for example).

The Sun is studied for several reasons. Firstly, the Sun is the nearest star to Earth, at an average distance of 1.50×10^{11}m or 93 million miles, and knowledge gained from it can be applied to other more distant stars. The Sun's vast amount of energy is produced by many nuclear fusion reactions within its core and investigating these reactions may lead to fusion machines on Earth, producing almost limitless amounts of clean, cheap energy. The interaction of the solar wind and the Earth's magnetic field is important, not only in the formation of the beautiful aurora in the northern and southern hemispheres, but also in predicting geomagnetic sub-storms that can play havoc with electricity networks and the navigation systems in ships and aircraft.

1.2 Observations

Recent photographs (see, for example, Priest, 1982) have shown many fascinating and varied events occurring on and near the Sun. These pictures should convince both astronomers and astrophysicists alike that the Sun is not the boring object that many people once thought. Indeed, it is an object of

great beauty and mystery certainly worthy of study. The next few paragraphs describe the Sun in more detail including some of the more spectacular events.

The Sun is about 4.5×10^9 years old, has a mass of 1.99×10^{30}kg, a radius of 6.96×10^8m and consists of a massive ball of plasma held and compressed by self gravity. This plasma is composed of about 90% hydrogen, 10% helium, and 0.1% of other elements such as carbon, nitrogen and oxygen.

Two sections may be distinguished in the Sun: the interior (the main body) and an external atmosphere; both are described below.

1.2.1   The Interior Structure

The overall interior structure of the Sun comprises of a central core, a radiative zone and a convection zone. The core is thought to have a temperature of 1.6×10^7K and a density of 1.6×10^5kg m^{-3}, high enough to sustain the thermonuclear reactions which generate 99% of the Sun's energy. Most of this energy is in the form of heat and light that is eventually radiated into space. The energy produced by the core is transported through the radiative and convection zones where the plasma's temperature drops to 6,600K and its density to 4×10^{-4}kg m^{-3}.

1.2.2   The Outer Atmosphere

The Sun's outer atmosphere is divided up into three different regions; the photosphere, chromosphere and the corona. The lowest layer is the photosphere, it is from here that most of the Sun's visible light escapes. The photosphere is 5×10^5m thick, has an average number density of 10^{23}m^{-3} and a temperature that decreases from 6,000K at the bottom to 4,300K where it meets the chromosphere. When observed at high resolution it appears to be covered with irregular cobble stone type shapes, called granular cells, that are in continual motion. Granular cells have a diameter ranging between 700km and 1,500km and lifetimes of between 7 and 10 minutes. Supergranular cells are also found on the photosphere. These are very irregular in shape, and are much larger than granular cells typically having diameters ranging from 2.0×10^4km to 5.4×10^4km, (Leighton *et al.*, 1962). Therefore, at any given time there are approximately 5,000 of these cells visible on the solar surface. Supergranular cells have a lifetime of about 20 hours, (Simon and Leighton, 1964). At the boundaries of these cells the magnetic field exceeds 30G. At the junction of three cells the magnetic field strength can be as high as 1-2kG. More details on solar granulation may be found in Bray and Loughhead (1967).

Above the photosphere is the chromosphere. The chromosphere is 2.5×10^6m thick. It has a temperature of 4,300K which increases monotonically with height to 10^6K. Many fine scale structures can be found within the chromosphere, for example spicules and fibrils, which will be described in more detail later.

Above the chromosphere is the corona, which cannot under normal circumstances be seen through the visible light emitted from the photosphere. It can, however be seen by the naked eye during solar eclipses. The corona stretches from the top of the chromosphere to Earth and beyond. The quiet corona, corresponding to solar minimums, has an average electron number density of several times 10^{14}m^{-3} and a temperature of about 10^6K, falling off with distance from the Sun. (The temperature in the solar wind actually increases further, but in a sense temperature here loses its meaning).

1.3   Features of the Sun

In this Section, various interesting properties of the Sun will be discussed. Within the solar atmosphere several areas may be found where there is a larger amount of magnetic flux present than in the

surroundings. These areas are called active regions and play an important part in many solar phenomena. Perhaps the most well known features found on the Sun are sunspots. These are observed in the photosphere, within a mature active region.

There are two areas associated with sunspots, a central area, the umbra and an outer region, the penumbra. Sunspots are much cooler than the surrounding plasma. The umbra generally has a temperature of about 4,100K and the penumbra 5,500K, (Wormell, 1936). Sunspots have very high magnetic fields associated with them. Most have a field strength ranging between 1-2kG, but they can occasionally exceed 4kG. The magnetic field strength increases with the area of the spot and the darker the spot, the stronger the field. Sunspots are generally found in pairs which gradually drift apart from one another, up to a distance of about 1.5×10^5km. For more details of sunspots, see Bray and Loughhead (1964).
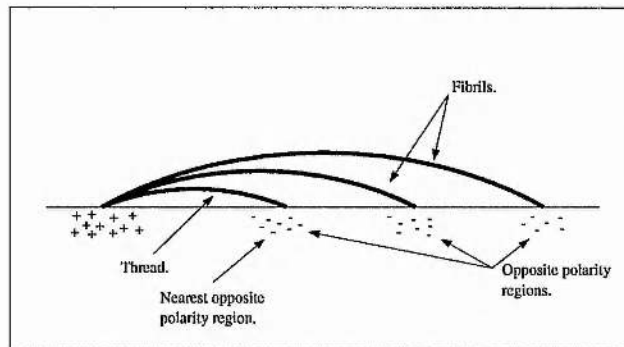
Figure 1.1: The difference between fibrils and threads. Notice that threads link the nearest opposite polarity regions directly, whereas fibrils span regions of opposite polarity before re-joining the photosphere.

Fibrils can sometimes be seen in Hα on the disk, within the chromosphere. These are long, thin, dark threads and are usually found near and at the edges of the active regions. An average fibril has a length of 15,000km, a width of 2,000km and is suspended at a height of 2,000km above the photosphere. Threads can also be seen in the chromosphere. They differ from fibrils in that threads link the nearest oppositely charged polarity regions directly, whereas fibrils span an enhanced network of like polarity before re-joining the photosphere, (Foukal, 1971a,b). This difference between fibrils and threads is illustrated in Figure 1.1.

Quantity	Spicules	Fibrils	Threads
Length	10,000km	15,000km	3,000-100,000km
Width	1,000km	2,000km	2,000km
Height		4,000km	2,000-4,000km
Lifetimes	8-15min	1-20min	>5min
Electron density	5×10^{10}-2×10^{11}m^{-3}	$> 10^{11}$m^{-3}	
Temperature	16,000K	$> 25 \times 10^3$K	
Internal motion	25km s^{-1}	20-30km s^{-1}	20-30km s^{-1}
Internal field	25-50G	>100G	>100G

Table 1.1: Typical values for spicules, fibrils and threads (from Foukal, 1971b).

Spicules also constitute a major part of the fine structure found in the chromosphere. Spicules are small plasma jets that can be seen in Hα within the chromosphere. They are usually cylindrical or cone-

shaped objects that rise to a height of about 1,000km, with an ascending speed ranging from 20km s^{-1} (Schmidt, 1974) to about 25km s^{-1}, (Michard, 1974). A typical spicule will have a diameter of about 900km, a temperature of 15,000K and an electron density of 10^9m^{-3}. Spicules are therefore much cooler and denser in comparison to the plasma surrounding them. Generally about 80 spicules are found per supergranular cell. The average sizes of fibrils, threads and spicules, according to Foukal (1971b), are shown in Table 1.1.

Occasionally, solar flares may be observed. These must surely rate as the most violent and beautiful events occurring within the solar system. Simply put, a flare is a rapid brightening seen in Hα. Flares usually form in the low chromosphere (invariably within active regions) and consist of a flash phase and a main phase. In the flash phase, the intensity of the emission increases rapidly over a period of about 5 minutes, whereas in the main phase, the intensity slowly decreases and takes from about an hour or so up to a day. The energy given off by a flare is approximately 10^{22}J for a small flare to 3×10^{25}J for a large flare. This energy is thought to come from the stressed magnetic field.

But perhaps the most amazing and spectacular observation has to be that of the prominence, described in the next Section.

1.4   Prominence Observations

The prominence is a remarkable solar feature. It may very loosely be defined as an object in either the chromosphere or corona that is denser and cooler than its surroundings. The prominences considered here will usually be found in the corona. Typically, prominences have a temperature about a hundred times lower and a density about a hundred to a thousand times higher than the corresponding coronal values.

Relation to sunspots	Place of origin	
	In the corona	Below the corona
Associated with sunspots	Rain Funnels Loops	Surges Puffs
Not associated with sunspots	Coronal rain Tree trunks Hedgerows Suspended clouds Mounds	Spicules

Table 1.2: The Menzel and Evans classification of prominences.

Several attempts have been made to classify prominences. In the past they have been categorised as moving and non-moving prominences (de Jager, 1959). Menzel and Evans (1953) grouped them according to whether they were associated with sunspots or not and to whether they appeared to originate in or below the corona (see Table 1.2). As can be seen in Table 1.2, prominences occur in many different shapes and sizes which makes classification difficult. The classification most recently used, divides prominences into two distinct groups, namely active region prominences and quiescent prominences.

1.4.1   Active Region Prominences

Active region prominences occur within active regions and are normally associated with flares. They are dynamic structures, usually moving with violent motions. This type of prominence is very unstable and tends to last from about a few minutes to a maximum of a few hours. Typical active region prominences are surges, sprays and loop prominences. The magnetic field strength in an active region prominence ranges from 20-100G and an average active region prominence will have an electron density of about 10^{17}m^{-3}.

1.4.2   Quiescent Prominences

Quiescent prominences are stable and can last from a few days to many months. A typical quiescent prominence will have a temperature of about 7,000K, an electron density of 10^{17}m^{-3} and a magnetic field strength of 5G. They are about 2×10^5km long, 5×10^4km high and have a width of 6,000km. These values are, however, only averages based upon observed prominences. More general ranges are given in Table 1.3. It should also be noted that the values for the temperature, density and magnetic field strength are not uniform and will vary within the prominence. When quiescent prominences are viewed end on, an area less bright than the average inner corona is seen. This darker area presumably consists of less dense plasma and is called a coronal cavity. Often a helmet streamer is also found above the prominence. The mass of a quiescent prominence is not accurately known, but it is thought to be about one tenth the total mass of the corona (Schmieder, 1990). Within and around the prominence many motions are observed. Within the prominence, Doppler shift has shown that the plasma moves with a downward velocity in the vertical threads ranging from 15-35km s^{-1}, although nearer the top of the prominence coarser knots move more slowly with speeds of about 0.5km s^{-1}.

Quantity	Range
Electron density	10^{16}-10^{17}m^{-3}
Central temperature	5,000-8,000K
Length	60,000-600,000km
Height	15,000-100,000km
Width	4,000-15,000km
Magnetic field strength	3-30G

Table 1.3: Typical ranges for quiescent prominence values.

However, Doppler images reveal that the plasma velocities are, in general, steadily upward with speeds between 1-3km s^{-1}, except at the feet of a hedgerow prominence where speeds may reach 10km s^{-1} either up or down (Zirker, 1989). Schmieder *et al.* (1988) reported downward velocities having a speed of <2.5km s^{-1}, a time scale of 5 minutes and suggested that the motions may be due to either plasma moving along twisted magnetic field lines or an instability triggering off waves along the filament. In one study of a quiescent prominence, Simon *et al.* (1986) suggested that the vertical motions were quicker than the horizontal ones. They deduced that the horizontal speeds were about a third of the vertical ones. Around a prominence, plasma is also observed to be in motion. Using Doppler images, Engvold *et al.* (1985) noticed that plasma rises up one leg of the arcade supporting the prominence and falls down the other at speeds of 5-15km s^{-1}.

Generally, the length scales for active region prominences tend to be smaller than those for quiescent prominences by a factor of about 3-4. The magnetic field strength tends to be greater by a factor of about ten. The density is similar to that found in quiescent prominences. Many quiescent prominences

reach down to the chromosphere and beyond in a series of regularly spaced feet (about 30Mm apart) which are located at supergranular boundaries.

1.4.3 Magnetic fields associated with Quiescent Prominences

Since quiescent prominences are denser than the corresponding corona and are suspended above the photosphere, there has to be a support mechanism associated with them. Generally it is thought that the magnetic field surrounding the prominence can supply the necessary upward force that prevents the prominence from dropping down to the solar surface. A detailed description of this will be given later. In this Section, the observed magnetic field is discussed. The magnetic field has so far been measured using two different methods based on the Zeeman and Hanle effects respectively. These are not discussed here, but, details may be obtained in Tandberg-Hanssen (1974) and Kim (1990), respectively. Prominences are formed above the polarity inversion line which separates the two oppositely charged areas of a bipolar region (Babcock and Babcock, 1955) and is shown in Figure 1.2. This polarity inversion line will also be found between the edge of the two main polarity regions of an active region or at the edge of an active region where it meets a neighbouring region of opposite charge.

Observations have shown that the magnetic field cuts the main axis of the prominence at an angle ranging from $15°$ (Tandberg-Hanssen and Anzer, 1970) to $25°$ (Leroy et al., 1983). The magnetic field strength is usually found to increase with height (Rust, 1967), although Kim (1990) found that for prominences lying north-south along a line of longitude, the magnetic field strength decreases with height. For the case in which the magnetic field strength increases with height, the gradient ranges from 0.6×10^{-4}G km^{-1} for younger prominences to about 1.6×10^{-4}G km^{-1} for long lived prominences (Leroy, 1977). Rust (1967) found that in most quiescent prominences, the average positive gradient was 1.0×10^{-4}G km^{-1} and Leroy et al. (1983) found a gradient of 0.5×10^{-4}G km^{-1}. The magnetic field strength associated with a prominence increases slightly during the prominence's lifetime. However, this field is generally found to be stable from day to day (Leroy, 1977).
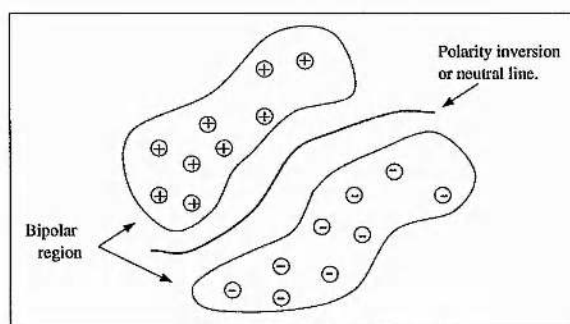
Figure 1.2: The polarity inversion line that separates the two oppositely directed magnetic regions found in a bipolar region.

Two types of magnetic field configurations are associated with quiescent prominences, namely normal polarity and inverse polarity. Both of these configurations feature a closed arcade of magnetic field lines overlying the prominence which connects the two regions of opposite polarity magnetic fields either side of the prominence. The difference between the two is that in an inverse polarity prominence, the magnetic field lines pass through the prominence in the opposite direction to the overlying arcade, whereas in a normal polarity prominence the magnetic field lines pass through the prominence in the same direction as the overlying magnetic field line arcade. Examples of the magnetic field line configurations for a normal polarity prominence and an inverse polarity prominence are illustrated in Figures 1.3(a) and

1.3(b), respectively. Notice that in a normal polarity prominence, there is a dip in the magnetic field. Without this dip, the plasma would drain away down the magnetic field lines. The curvature and magnetic pressure in both these magnetic structures provides the necessary upward force to support the prominence against gravity.

In a study involving 256 low to medium latitude prominences by Leroy *et al.* (1984), it was observed that prominences with a maximum height lower than 30,000km had a magnetic field that was of the normal polarity type. The magnetic field was inclined at 20° to the main axis of the prominence and had an average strength of 20G. For prominences that had a maximum height larger than 30,000km the magnetic field configuration was that of inverse polarity. For these prominences, the magnetic field was found to be inclined at 25° to the prominence main axis and had a field strength ranging from 5-10G. It was also observed that out of 120 prominences found in the polar crown none were of the normal polarity type.
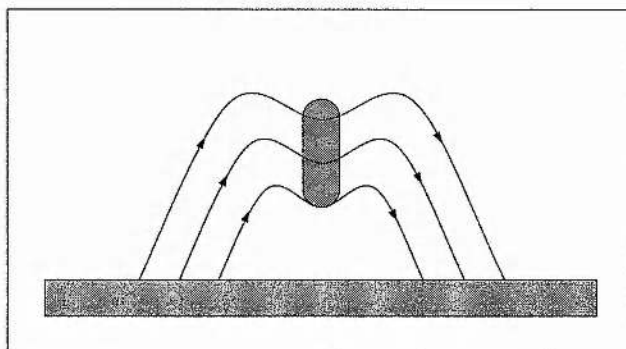
Figure 1.3(a): The field line structure found in normal polarity prominences.
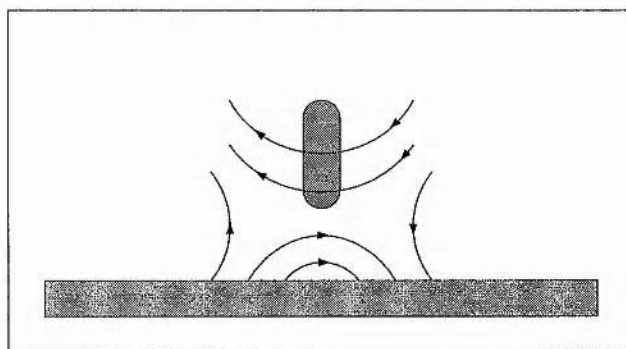
Figure 1.3(b): The field line structure found in inverse polarity prominences.

An interesting point to note here is that in inverse polarity prominences the magnetic field completely surrounds the prominence, keeping it cool relative to the hot corona. This is due to the anisotropic nature of thermal conduction.

1.5 Fine Structure within a Prominence

All observed quiescent prominences have a fine structure associated with them. This fine structure appears to consist of thin bright threads and knots. These threads have a typical length of 5,000km,

with the first indication of the thickness given by Dunn (1960). He estimated that the thickness of these threads was 300km or less. Since then, various authors have also estimated the thickness of these threads, for example, Engvold (1976) suggested that the widths ranged between 400-1,500km. Some of the estimates are given in Table 1.4. From the values of thread width given in Table 1.4, it can be seen that the size of the threads appears to range from a few hundred km to about 1,500km. Leroy *et al.* (1983) suggested that many quiescent prominences have a filling ratio of about 0.10. It was observed by Engvold (1976) that the sizes of some threads and smaller prominence fine scale structures increase with height, this means that the threads are not necessarily of constant width down the prominence.

Engvold (1976) observed diffuse bright knots within a quiescent prominence with a size of around 1,500-5,000km. These were usually stationary for 2-10 minutes before descending with speeds of about 15-35km s^{-1}. However, in a bright quiescent prominence with lots of fine structure, he found that these bright knots were very difficult to observe. He also noticed that when using exceptionally high resolution frames, bright knots would occasionally form long strings. Using different frames, he noticed that the same features appeared as uniform bright threads. This suggests that the possible distinctive feature between threads and knots was due to the spatial resolution of the observations and that bright knots were the basic unit of fine structure within a quiescent prominence. However, the dimensions of the fine scale structure are not accurately known. Indeed it is quite possible, that more fine scale structures will be revealed within a quiescent prominence as the resolution of the observations is further increased.

Orrall and Zirker (1961) found that there was no change in the shape and brightness of the fine scale structure associated with a quiescent prominence over a time scale of around 10^{4}s and that fine structure may last for 10^{5}s or longer. Engvold (1976) noticed that some threads could be seen for one hour or longer and that bright knots could be observed for about 8 minutes. It was also recorded that the process of condensation and subsequent destruction of the prominence's fine scale structure appeared to take place over a very short time scale compared to the lifetime of the regions where a prominence may exist.

Thickness of thread (in km)	Author	Year
< 300	Dunn	1960
400-1,500	Engvold	1976
1,000	Leroy *et al.*	1983
< 200	Zirker and Koutchmy	1990

Table 1.4: Some observed values for the thickness of fine structure within quiescent prominences.

Material is often seen slowly streaming down these threads at speeds of around 1km s^{-1} and Malville (1976) recorded speeds of less than 10km s^{-1}. It is interesting to note that these speeds are less than the free-fall speed. The mass lost due to this flow and also the flow through the prominence's feet is relatively large. This mass must somehow be replaced, or the prominence would drain away very quickly.

Towards the end of their lifetime, many quiescent prominences erupt into solar flares. Just before this occurs, the prominence is seen to oscillate. This could be a consequence of magnetothermal instabilities, where magnetic and thermal instabilities interact (see Chapter 4).

1.6 Prominence Formation

From the observations of prominences described earlier, it may be apparent that six conditions are associated with the formation of quiescent prominences (Martin, 1990). These conditions are: opposite

polarity magnetic fields either side of the prominence, an overlying magnetic field line arcade, transverse fields, fibrils aligned with the magnetic field in the chromosphere and parallel to the long axis of the prominence, converging fields and cancelling fields. It should be noted that these conditions are not independent and that none of these conditions by themselves are sufficient for a quiescent prominence to form.

Often, after a quiescent prominence has erupted, another prominence is observed in the same location, indicating that many of the above conditions are still present long after the original quiescent prominence has been destroyed.

As remarked earlier, quiescent prominences are denser and cooler than the surrounding plasma and have a mass of about one tenth of the total corona. One question arises as to how this amount of plasma can be concentrated in a relatively small region of the corona. Three distinct mechanisms have been proposed, namely ballistic injection, siphon and thermal instability. In the first, ballistic injection, plasma is propelled upwards from the chromosphere. However, it is unlikely to happen in practise due to the frequency of prominences observed and the conditions needed for prominence formation. In the siphon mechanism, the plasma pressure at the top of the loop decreases. This sucks up the plasma from the chromosphere to the top of the loop. The disadvantage of these two mechanisms is, that for a perfectly conducting plasma, the magnetic field lines move with the plasma (by the frozen in theorem) destroying the magnetic field structure associated with the prominence, unless the siphon or injection is along the field lines. The thermal instability mechanism is the most likely candidate for prominence formation. This happens when a condensation is driven by the plasma's optically thin radiation. A detailed description of the thermal instability mechanism is given in Chapter 2. It accounts not only for prominence formation, but also for the coronal cavity seen above the prominence. It is also possible that the thermal instability may induce the siphon. Thus, these two mechanisms can combine.

1.7   Thesis Aims

The aim of this thesis is to investigate thermal instabilities in the solar corona, since it may play an important part in the formation of prominences and the associated fine scale structure. Many quiescent prominences erupt into solar flares and a possible mechanism is proposed and discussed. This thesis is concerned about linear theory only, in a cylindrical equilibrium. The equilibrium is taken to be the Gold-Hoyle equilibrium profile because of its simplicity and the corresponding results are well known. This equilibrium is perturbed and the equations describing normal modes obtained.

In Chapter 2 the MHD equations are introduced and described in detail. The thermal instability mechanism is discussed physically and the conditions for isobaric, isochoric and isentropic instability derived for an infinite, uniform plasma.

Chapter 3 considers the thermal instability in a cylindrical geometry. The equations for normal modes in an infinite, one-dimensional cylinder are derived and the normal mode spectrum investigated. The normal mode spectrum consists of both discrete modes and continuous bands. These continuous spectra are examined with various dissipative effects included. Neglecting dissipative effects there are three types of continuous spectra namely Alfvén, slow and thermal continua. However, when finite, scalar resistivity is included it is shown that the continuous spectra consist of only the thermal continuum. For a cool form of the Gold-Hoyle equilibrium profile the most unstable quasi-continuum mode is examined as resistivity is varied. It is found that the length scales generated scale as the coefficient of resistivity to the power one quarter similar to the length scales generated by perpendicular thermal conduction. Dissipation due to resistivity and perpendicular thermal conduction could therefore be the cause of the observed fine scale structure seen within prominences.

Chapter 4 investigates the interaction of magnetic and thermal instabilities using the same geometry as in Chapter 3. For certain values of the ratio of the thermal to Alfvén time scales it is found that these

instabilities can combine to form overstable wave or magnetothermal modes. The ballooning equations, for an arcade with zero resistivity and zero perpendicular thermal conduction, were manipulated to form a dispersion relation. A WKB analysis was performed to predict the growth rate of the magnetic instability for large values of the axial wave number. The oscillations observed just before a flare occurs may be due to magnetothermal modes. Thus, it may be possible that a neighbouring thermal instability might trigger a magnetic instability and be the cause of prominences erupting into solar flares.

The magnetic field lines considered in Chapters 3 and 4 have been of infinite length. This is not very a realistic situation, so Chapter 5 examines the effects of line-tying on the thermal instability. This is when the magnetic field lines are of finite length and anchored in the photosphere. The method of solution is outlined, however the effect of line-tying on the thermal continuum is not known, so the study is incomplete. This is left for future work.

Chapter 2

The Thermal Instability Mechanism

*I did everything that I could think of to the brink of disaster and I did
not lose control of the Imp for even a heart-stopping fraction of a second.
It took impossible corners at ridiculous speeds, it stopped on skating-rink
surfaces where no car could have stopped. It might have been running on railway
lines for all the notice it took of a lifetime of murderous driving that I
inflicted...*

-Daily Mail review on the Imp.

2.1 Introduction

In this Chapter, the basic MHD equations are presented and the thermal instability mechanism discussed.
The MHD equations are linearised and the basic instability criteria for a uniform, infinite medium
obtained.

For any plasma, an energy loss-gain function per unit mass may be defined which describes how the
plasma is heated and how it cools. Let the cooling of the plasma be denoted by C and the heating of
the plasma be denoted by H. Then the energy loss-gain function per unit mass may be defined as

$$\rho \mathcal{L} \;=\; C - H, \tag{2.1}$$

where the heat gain is defined as a negative loss. For most plasmas, $\mathcal{L}$ will depend on the usual
thermodynamic quantities, such as temperature; it may also depend upon the chemical composition of
the plasma, its surroundings and also upon the magnetic field. The basic thermal instability mechanism
can therefore be stated as follows. Assume that as the temperature drops the loss-gain function $\mathcal{L}$ is
positive. Consider a small decrease in temperature. This corresponds to an energy loss since $\mathcal{L} > 0$ and
so the plasma cools, thus causing a further reduction in the temperature. Hence, an initial perturbation
in the plasma's temperature will grow in time. Since, without any additional heating, the plasma
cannot return to its initial state, an instability will result. The first approximation of the solar corona
is to model it as a hot hydrogen plasma. Parker (1953) stressed that the radiation of ionised metallic
impurity elements had to be included in the energy loss-gain function. Since the solar corona has a
high temperature and a low density, this radiation is assumed to be optically thin. Several authors have
calculated the energy radiated away from the plasma due to this optically thin radiation (McWhirter
et al., 1975 and Raymond and Smith, 1977). An analytical fit to the radiation calculated by Raymond
and Smith (1977) was made by Rosner *et al.* (1978) and is described by

$$C \;=\; \chi n^2 T^\alpha \;=\; \tilde{\chi} \rho^2 T^\alpha \;=\; \bar{\chi} p^2 T^{\alpha-2}, \tag{2.2}$$

where χ and α are piecewise constant functions of temperature and n is the ion number density. The values of χ and α are given in Table 2.1.

$\log_{10} T$	α	$\log_{10} \chi$
< 3.89063	11.7	-82.9
3.89063 - 4.30195	6.15	-61.307
4.30195 - 4.575	0	-34.85
4.575 - 4.9	2	-44.0
4.9 - 5.4	0	-34.2
5.4 - 5.77	-2	-23.4
5.77 - 6.315	0	-34.94
6.315 - 7.60457	-2/3	-30.73
> 7.60457	0.5	-39.602

Table 2.1: The piecewise constant values of α and χ in the optically thin radiation term in the energy equation. (After Rosner *et al.*, 1978).

As can be seen in the form of the plasma cooling given by Equation (2.2), whenever $\alpha < 0$, a temperature drop will result in an increase in cooling and hence a thermal instability. Notice also the effect of the plasma's density on the thermal instability. This can drive the thermal instability, since whenever the plasma's density increases, so too will the cooling. The most common type of thermal instability found in the solar corona is the isobaric instability criteria. This is when the instability evolves at constant pressure, since the plasma has time to set up flows to balance out the change in pressure. This may also induce siphons, see Chapter 1. The thermal instability mechanism continues until the plasma reaches a temperature of around 7,000K where $\alpha = 6.15$. The plasma's radiation becomes optically thick and thermal stability is achieved. It is therefore easy to understand how the thermal instability mechanism is a likely candidate for the formation of prominences in the solar corona.

2.2   The Basic MHD Equations

The basic equations used throughout this thesis are the standard equations of resistive magnetohydrodynamics (or MHD) in which gravity, viscosity and rotational effects are neglected. The dynamic evolution of the plasma is governed by the continuity equation, the momentum equation and the induction equation

$$\frac{\partial \rho}{\partial t} + \rho \nabla \cdot \mathbf{v} + \mathbf{v} \cdot \nabla \rho \;=\; 0, \tag{2.3}$$

$$\rho \left[\frac{\partial \mathbf{v}}{\partial t} + (\mathbf{v} \cdot \nabla) \mathbf{v} \right] \;=\; -\nabla p + \frac{1}{\mu} (\nabla \times \mathbf{B}) \times \mathbf{B}, \tag{2.4}$$

$$\frac{\partial \mathbf{B}}{\partial t} \;=\; \nabla \times (\mathbf{v} \times \mathbf{B}) - \nabla \times (\eta \nabla \times \mathbf{B}), \tag{2.5}$$

where $\mathbf{v}$, μ and $\mathbf{B}$, represent the plasma's velocity, magnetic permeability ($= 4\pi \times 10^{-7}$ henry m^{-1}) and magnetic induction (usually referred to as the magnetic field), respectively. The magnetic diffusivity η is temperature-dependent and is given by (Priest, 1982)

$$\eta \;=\; \eta(T) \;=\; \frac{1}{\mu\sigma} \;=\; 5.2 \times 10^7 \log \Lambda \; T^{-3/2} \mathrm{m}^2 \; \mathrm{s}^{-1}, \tag{2.6}$$

where σ is the electrical conductivity and $\log \Lambda$ is the Coulomb logarithm. The plasma pressure p, density ρ and temperature T are related by the ideal gas law

$$p \;\; = \;\; \frac{\mathcal{R}}{\widetilde{\mu}} \rho T, \tag{2.7}$$

where $\mathcal{R}$ is the gas constant ($= 8.3 \times 10^3$) and $\widetilde{\mu}$ is the mean molecular weight (which has been taken to be unity for simplicity). The energetics are governed by an energy equation, of the form

$$\frac{\rho^\gamma}{\gamma - 1} \left[\frac{\partial}{\partial t} \left(\frac{p}{\rho^\gamma} \right) + (\mathbf{v} \cdot \nabla) \left(\frac{p}{\rho^\gamma} \right) \right] \;\; = \;\; \nabla \cdot (\kappa \nabla T) - \rho \mathcal{L} (\rho, T) + \frac{\eta}{\mu} |\nabla \times \mathbf{B}|^2, \tag{2.8}$$

where γ is the adiabatic index ($= 5/3$), κ the thermal conduction tensor and $\mathcal{L}$ the generalised energy loss function per unit mass with energy gains defined as negative losses. In the energy loss function, an optically thin radiative loss term and an unspecified coronal heating function H are included. The anisotropic thermal conduction term is rewritten in terms of the coefficients of heat conduction parallel ($\kappa_\parallel$) and perpendicular ($\kappa_\perp$) to the magnetic field

$$\nabla \cdot (\kappa \nabla T) \;\; = \;\; \mathbf{B} \cdot \nabla \left(\kappa_\parallel \frac{\mathbf{B} \cdot \nabla T}{B^2} \right) + \nabla \cdot \left(\kappa_\perp \frac{\mathbf{B} \times (\nabla T \times \mathbf{B})}{B^2} \right), \tag{2.9}$$

where for sufficiently strong fields (Braginskii, 1965)

$$\kappa_\parallel \;\; = \;\; \kappa_\parallel (T) \;\; \approx \;\; 1.8 \times 10^{-10} (\log \Lambda)^{-1} T^{2.5} \mathrm{Wm}^{-1}\mathrm{K}^{-1}, \tag{2.10}$$

and

$$\kappa_\perp \;\; = \;\; \kappa_\perp (\rho, T, B) \;\; \approx \;\; 8.2 \times 10^{-33} (\log \Lambda)^2 n^2 B^{-2} T^{-3} \kappa_\parallel, \tag{2.11}$$

where n the number density. In these formulae n is measured in m^{-3}, temperature in Kelvin and the magnetic field in Tesla. Typically in the solar corona $\log \Lambda \approx 22$ and $\kappa_\perp \approx 10^{-12} \kappa_\parallel$. Parallel thermal conduction is mainly due to the plasma's electrons, whilst perpendicular thermal conduction is the result of the plasma's ions. The magnetic field must further satisfy the condition

$$\nabla \cdot \mathbf{B} \;\; = \;\; 0. \tag{2.12}$$

The electric current density $\mathbf{j}$ has been eliminated from Equations (2.4), (2.5) and (2.8). It may be calculated using Ampère's law

$$\mathbf{j} \;\; = \;\; \frac{1}{\mu} \nabla \times \mathbf{B}. \tag{2.13}$$

The electric field $\mathbf{E}$ can then be evaluated using the simplified Ohm's law providing the plasma's magnetic field and velocity have been found

$$\mathbf{E} \;\; = \;\; -\mathbf{v} \times \mathbf{B} + \mathbf{j}/\sigma. \tag{2.14}$$

In summary, the continuity, momentum, induction and energy equations together with the ideal gas law determine $\mathbf{v}$, $\mathbf{B}$, ρ, p and T subject to the condition that the magnetic field is divergence free.

2.3   A Physical Description of the Thermal Instability Mechanism

In this Section a physical description of the thermal instability mechanism is given. The behaviour of the thermal instability will depend upon several characteristic time scales of the plasma. Usually in the solar corona, the sound time scale is much shorter than the radiative (or thermal instability) time scale. This means that the plasma can respond and set up flows to equalise any pressure drop that results from a decrease in temperature. Hence, as the thermal instability occurs, the plasma can smooth out pressure gradients and the instability evolves isobarically. However, around temperatures of 10^5K, the radiative time scale can be much less than the sound time scale. The plasma does not have time to set up any flows to equalise the pressure decrease and consequently the thermal instability evolves isochorically. These two cases can be readily seen in the analysis in Section 2.4.

The next question that arises is concerned with why the solar corona exists at all especially since the above argument suggests that it is always thermally unstable. This can be answered by the fact that the effects of thermal conduction have so far been neglected. There are two time scales associated with thermal conduction when a magnetic field is included. These correspond to thermal conduction perpendicular and parallel to the equilibrium magnetic field, see Equations (2.10) and (2.11). The time scale corresponding to perpendicular thermal conduction is much greater than that for parallel thermal conduction which is very effective at equalising out any temperature variations along magnetic field lines. The parallel thermal conduction time scale is proportional to the square of the length of the field line and thus is very efficient at stabilising the thermal mode over short distances. Thus, for a thermal instability to form in the solar corona, it is necessary to have either long field lines so that the conduction time scale is much larger than the radiative time scale, or an initial disturbance that gives a zero perturbation in the parallel conduction term.

So far, linear theory has been discussed along with temperature decreases. Equally possible are situations where the plasma temperature increases. However, in the non-linear case, only a temperature drop is likely to occur in practice since, in Equation (2.10) any increase in temperature results in a greater value for parallel thermal conduction thus smoothing out the temperature increase.

2.4   Thermal Instability in a Uniform Infinite Medium

In this Section, the thermal instability in a uniform, infinite plasma is considered and the instability criteria derived. The procedure used is identical to that first used by Field (1965). The standard MHD equations (2.3), (2.4), (2.5), (2.7) and (2.8) with the magnetic diffusivity η set equal to zero, are linearised ($\rho = \rho_0 + \rho_1$, etc.) about an infinite, uniform ($\rho_0 = $ constant, etc.), static ($\mathbf{v}_0 = 0$) equilibrium to give

$$\frac{\partial \rho_1}{\partial t} + \rho_0 \nabla \cdot \mathbf{v}_1 = 0, \tag{2.15}$$

$$\rho_0 \frac{\partial \mathbf{v}_1}{\partial t} = -\nabla p_1 + \frac{1}{\mu} \left(\nabla \times \mathbf{B}_1 \right) \times \mathbf{B}_0, \tag{2.16}$$

$$\frac{\partial \mathbf{B}_1}{\partial t} = \nabla \times \left(\mathbf{v}_1 \times \mathbf{B}_0 \right), \tag{2.17}$$

$$p_1 = \frac{p_0}{\rho_0} \rho_1 + \frac{p_0}{T_0} T_1, \tag{2.18}$$

and

$$\frac{1}{(\gamma-1)}\frac{\partial p_1}{\partial t} = \frac{\gamma p_0}{(\gamma-1)\rho_0}\frac{\partial \rho_1}{\partial t} - \rho_0 \left(\frac{\partial \mathcal{L}}{\partial \rho}\right)_T \rho_1 - \rho_0 \left(\frac{\partial \mathcal{L}}{\partial T}\right)_\rho T_1$$

$$+ \mathbf{B}_0 \cdot \nabla \left[\frac{\kappa_\parallel}{B_0^2}\mathbf{B}_0 \cdot \nabla T_1\right] + \nabla \cdot \left[\frac{\kappa_\perp}{B_0^2}\mathbf{B}_0 \times (\nabla T_1 \times \mathbf{B}_0)\right]. \tag{2.19}$$

For a uniform plasma, the equilibrium energy equation becomes

$$\mathcal{L}(\rho_0, T_0) = 0. \tag{2.20}$$

This defines the heating function as a constant given by

$$H = \rho_0 h = \tilde{\chi}\rho_0^2 T_0^\alpha. \tag{2.21}$$

Because the plasma is infinite in all directions, normal mode solutions may be obtained by letting all the perturbed quantities behave like

$$\rho_1 = \rho' \exp i (\mathbf{k} \cdot \mathbf{r}) e^{st}, \tag{2.22}$$

where ρ' is a constant, $\mathbf{k}$ is the wave vector and s is the growth rate. As can be seen, whenever $\mathrm{Re}(s) > 0$, $\exp(st)$ becomes large and the perturbations grow in time. Hence an instability will form whenever $\mathrm{Re}(s) > 0$. Therefore, the method used to find the instability criteria will be to derive the dispersion relation and locate the positive roots. The linearised equations (2.15)-(2.19) become

$$\frac{1}{\gamma-1}sp' - \frac{\gamma p_0 s}{(\gamma-1)\rho_0}\rho' + \rho_0 \left(\frac{\partial \mathcal{L}}{\partial T}\right)_\rho T' + \rho_0 \left(\frac{\partial \mathcal{L}}{\partial \rho}\right)_T \rho' + k_\parallel^2 \kappa_\parallel T' + k_\perp^2 \kappa_\perp T' = 0, \tag{2.23}$$

$$s\mathbf{B}' + i\mathbf{B}_0 (\mathbf{k} \cdot \mathbf{v}') - iB_0 k_\parallel \mathbf{v}' = \mathbf{0}, \tag{2.24}$$

$$\frac{p'}{p_0} - \frac{\rho'}{\rho_0} - \frac{T'}{T_0} = 0, \tag{2.25}$$

$$s\rho' + i\rho_0 \mathbf{k} \cdot \mathbf{v}' = 0, \tag{2.26}$$

and

$$s\rho_0 \mathbf{v}' + i\mathbf{k}p' + \frac{i}{\mu}(\mathbf{B}_0 \cdot \mathbf{B}')\mathbf{k} - \frac{i}{\mu}B_0 k_\parallel \mathbf{B}' = \mathbf{0}, \tag{2.27}$$

where $k_\parallel$ and $k_\perp$ are wave numbers parallel and perpendicular to the equilibrium magnetic field defined by

$$k_\parallel = \frac{\mathbf{B}_0 \cdot \mathbf{k}}{B_0}, \quad \text{and} \quad k_\perp^2 = k^2 - \left(\frac{\mathbf{B}_0 \cdot \mathbf{k}}{B_0}\right)^2. \tag{2.28}$$

Taking the scalar product of Equations (2.24) and (2.27) with $\mathbf{B}_0$ and $\mathbf{k}$ yields

$$s\mathbf{B}' \cdot \mathbf{B}_0 + iB_0^2 (\mathbf{k} \cdot \mathbf{v}') - iB_0 k_\parallel \mathbf{B}_0 \cdot \mathbf{v}' = 0, \tag{2.29}$$

$$\mathbf{k} \cdot \mathbf{B}' = 0, \tag{2.30}$$

$$s\rho_0 \mathbf{B}_0 \cdot \mathbf{v}' + i\left(\mathbf{k} \cdot \mathbf{B}_0\right) p' \;=\; 0, \tag{2.31}$$

and

$$s\rho_0 \mathbf{k} \cdot \mathbf{v}' + ik^2 p' + \frac{i}{\mu}\left(\mathbf{B}_0 \cdot \mathbf{B}'\right) k^2 - \frac{i}{\mu} B_0 k_\parallel \left(\mathbf{k} \cdot \mathbf{B}'\right) \;=\; 0. \tag{2.32}$$

Substituting Equation (2.30) into Equation (2.32) and eliminating $\mathbf{v}' \cdot \mathbf{B}_0$ in Equation (2.29) using Equation (2.31) produces the following two equations

$$s\rho_0 \mathbf{k} \cdot \mathbf{v}' + ik^2 p' + \frac{i}{\mu}\left(\mathbf{B}_0 \cdot \mathbf{B}'\right) k^2 \;=\; 0, \tag{2.33}$$

and

$$\rho_0 s^2 \mathbf{B}' \cdot \mathbf{B}_0 + i\rho_0 s B_0^2 \left(\mathbf{k} \cdot \mathbf{v}'\right) - B_0^2 k_\parallel^2 p' \;=\; 0. \tag{2.34}$$

Taking the vector cross product of Equation (2.24) with $\mathbf{B}_0$ and then taking the scalar product with $\mathbf{k}$ gives

$$s\mathbf{B}' \times \mathbf{k} \cdot \mathbf{B}_0 \;=\; iB_0 k_\parallel \mathbf{v}' \times \mathbf{k} \cdot \mathbf{B}_0. \tag{2.35}$$

Taking the cross product of Equation (2.27) with $\mathbf{k}$ and then taking the scalar product with $\mathbf{B}_0$ gives

$$s^2 \rho_0 \mathbf{v}' \times \mathbf{k} \cdot \mathbf{B}_0 \;=\; \frac{i}{\mu} B_0 k_\parallel s \mathbf{B}' \times \mathbf{k} \cdot \mathbf{B}_0. \tag{2.36}$$

Eliminating $\mathbf{B}' \times \mathbf{k} \cdot \mathbf{B}_0$ from Equation (2.35) using Equation (2.36) gives

$$\left[s^2 + \frac{\left(\mathbf{k} \cdot \mathbf{B}_0\right)^2}{\mu \rho_0} \right] \mathbf{v}' \cdot \mathbf{k} \times \mathbf{B}_0 \;=\; 0. \tag{2.37}$$

Equation (2.37) shows that the $\mathbf{k} \times \mathbf{B}_0$ component of the perturbed velocity decouples from the other perturbed velocities and has the frequency of a pure Alfvén wave.

Equations (2.23), (2.25), (2.26), (2.33) and (2.34) are five equations in the five unknowns $\mathbf{B}' \cdot \mathbf{B}_0$, $\mathbf{k} \cdot \mathbf{v}'$, p', T' and ρ'. Hence, for a non-trivial solution the determinant of the coefficients must vanish, yielding the dispersion relation

$$s^5 + \frac{1}{C_v \rho_0}\left[\kappa_\parallel k_\parallel^2 + \kappa_\perp k_\perp^2 + \rho_0 \left(\frac{\partial \mathcal{L}}{\partial T}\right)_\rho \right] s^4 + k^2 \left(c_s^2 + v_A^2\right) s^3$$

$$+ \frac{k^2 \left(c_i^2 + v_A^2\right)}{C_v \rho_0}\left[\kappa_\parallel k_\parallel^2 + \kappa_\perp k_\perp^2 + \rho_0 \left(\frac{\partial \mathcal{L}}{\partial T}\right)_\rho - \frac{c_i^2 \rho_0^2}{T_0 \left(c_i^2 + v_A^2\right)}\left(\frac{\partial \mathcal{L}}{\partial \rho}\right)_T \right] s^2 + c_s^2 k^2 \frac{\left(\mathbf{k} \cdot \mathbf{B}_0\right)^2}{\mu \rho_0} s$$

$$+ \frac{c_i^2 k^2}{C_v \rho_0} \frac{\left(\mathbf{k} \cdot \mathbf{B}_0\right)^2}{\mu \rho_0}\left[\kappa_\parallel k_\parallel^2 + \kappa_\perp k_\perp^2 + \rho_0 \left(\frac{\partial \mathcal{L}}{\partial T}\right)_\rho - \frac{\rho_0^2}{T_0}\left(\frac{\partial \mathcal{L}}{\partial \rho}\right)_T \right] \;=\; 0, \tag{2.38}$$

where c_s is the sound speed, c_i is the isothermal sound speed and v_A is the Alfvén speed defined by

$$c_s^2 \;=\; \frac{\gamma p_0}{\rho_0}, \qquad c_i^2 \;=\; \frac{p_0}{\rho_0}, \qquad v_A^2 \;=\; \frac{B_0^2}{\mu \rho_0}, \tag{2.39}$$

and where C_v is the specific heat at constant volume given by

$$C_v = \frac{\mathcal{R}}{\tilde{\mu}(\gamma - 1)}. \tag{2.40}$$

Since the Alfvén modes have decoupled, it follows that Equation (2.38) represents the two fast modes, two slow modes and the thermal mode. It should be noted that in other geometries the Alfvén modes would not generally decouple and the dispersion relation would be a polynomial of degree 7 in s. Neglecting all the non-adiabatic terms in Equation (2.38) yields

$$s\left(s^4 + k^2\left(c_s^2 + v_A^2\right)s^2 + k^2 c_s^2\frac{(\mathbf{k}\cdot\mathbf{B}_0)^2}{\mu\rho_0}\right) = 0. \tag{2.41}$$

From Equation (2.41) it can be seen that the thermal mode has collapsed into the origin and that the usual dispersion relation for ideal fast and slow magnetoacoustic waves is obtained.

To investigate thermal instabilities, the roots of the dispersion equation (2.38) are examined. A thermal instability will occur whenever a root satisfies $\mathrm{Re}\,(s) > 0$. Equation (2.38) is a fifth order polynomial and, providing that $\mathbf{k}\cdot\mathbf{B}_0 \neq 0$, will have at least one positive real root whenever

$$\kappa_\parallel k_\parallel^2 + \kappa_\perp k_\perp^2 + \rho_0\left(\frac{\partial\mathcal{L}}{\partial T}\right)_\rho - \frac{\rho_0^2}{T_0}\left(\frac{\partial\mathcal{L}}{\partial\rho}\right)_T < 0 \qquad \text{(for } \mathbf{k}\cdot\mathbf{B}_0 \neq 0). \tag{2.42}$$

If $\mathbf{k}\cdot\mathbf{B}_0 = 0$, the last two terms in Equation (2.38) vanish and $k_\parallel = 0$. Thus Equation (2.38) simplifies and has at least one positive real solution whenever

$$\kappa_\perp k_\perp^2 + \rho_0\left(\frac{\partial\mathcal{L}}{\partial T}\right)_\rho - \frac{c_i^2\rho_0^2}{T_0\left(c_i^2 + v_A^2\right)}\left(\frac{\partial\mathcal{L}}{\partial\rho}\right)_T < 0 \qquad \text{(for } \mathbf{k}\cdot\mathbf{B}_0 = 0). \tag{2.43}$$

Equations (2.42) and (2.43) are the isobaric instability criteria first derived by Field (1965). Notice that there are different instability criteria depending on whether $\mathbf{k}\cdot\mathbf{B}_0 = 0$ or $\mathbf{k}\cdot\mathbf{B}_0 \neq 0$ or $\mathbf{k} = \mathbf{0}$. The surface on which $\mathbf{k}\cdot\mathbf{B}_0 = 0$ is called the mode rational surface. Field (1965) also showed that the fast and slow magnetoacoustic waves can become overstable. To derive this criterion, the dispersion relation given by Equation (2.38) is rearranged to give

$$\left(s^4 + k^2\left(c_s^2 + v_A^2\right)s^2 + k^2 c_s^2\frac{(\mathbf{k}\cdot\mathbf{B}_0)^2}{\mu\rho_0}\right)\left(s + \frac{1}{C_v\rho_0}\left[\kappa_\parallel k_\parallel^2 + \kappa_\perp k_\perp^2 + \rho_0\left(\frac{\partial\mathcal{L}}{\partial T}\right)_\rho\right]\right)$$

$$-\frac{c_i^2 k^2}{C_v\rho_0}\left((\gamma-1)\left[\kappa_\parallel k_\parallel^2 + \kappa_\perp k_\perp^2 + \rho_0\left(\frac{\partial\mathcal{L}}{\partial T}\right)_\rho\right] + \frac{\rho_0^2}{T_0}\left(\frac{\partial\mathcal{L}}{\partial\rho}\right)_T\right)\left(s^2 + \frac{(\mathbf{k}\cdot\mathbf{B}_0)^2}{\mu\rho_0}\right) = 0. \tag{2.44}$$

Following Field (1965), the growth rate is expanded as

$$s = s_0 + s_1 + \dots, \tag{2.45}$$

where s_0 satisfies the dispersion relation for the fast and slow magnetoacoustic waves given by

$$s_0^4 + k^2\left(c_s^2 + v_A^2\right)s_0^2 + k^2 c_s^2\frac{(\mathbf{k}\cdot\mathbf{B}_0)^2}{\mu\rho_0} = 0, \tag{2.46}$$

and where

$$s_1 \sim O\left(\frac{1}{C_v\rho_0 c_s}\left[\kappa_\parallel k_\parallel^2 + \kappa_\perp k_\perp^2 + \rho_0\left(\frac{\partial\mathcal{L}}{\partial T}\right)_\rho\right], \frac{\rho_0}{C_v T_0 c_s}\left(\frac{\partial\mathcal{L}}{\partial\rho}\right)_T\right). \tag{2.47}$$

Substituting the growth rate expansion given by Equation (2.45) into the dispersion relation given by Equation (2.44) and using Equation (2.46) gives the first order correction s_1 as

$$s_1 = -\frac{\frac{c_s^2}{C_v \rho_0} \left((\gamma - 1) \left[\kappa_\parallel k_\parallel^2 + \kappa_\perp k_\perp^2 + \rho_0 \left(\frac{\partial \mathcal{L}}{\partial T} \right)_\rho \right] + \frac{\rho_0^2}{T_0} \left(\frac{\partial \mathcal{L}}{\partial \rho} \right)_T \right) \left(s_0^2 + \frac{(\mathbf{k} \cdot \mathbf{B}_0)^2}{\mu \rho_0} \right)}{2\gamma \left(c_s^2 + v_A^2 \right) \left(s_0^2 + \frac{2c_s^2}{(c_s^2 + v_A^2)} \frac{(\mathbf{k} \cdot \mathbf{B}_0)^2}{\mu \rho_0} \right)}. \qquad (2.48)$$

Notice that if $\mathbf{k} \cdot \mathbf{B}_0 = 0$, Equation (2.48) reduces to

$$s_1 = -\frac{c_s^2}{2C_v \rho_0 \gamma (c_s^2 + v_A^2)} \left((\gamma - 1) \left[\kappa_\parallel k_\parallel^2 + \kappa_\perp k_\perp^2 + \rho_0 \left(\frac{\partial \mathcal{L}}{\partial T} \right)_\rho \right] + \frac{\rho_0^2}{T_0} \left(\frac{\partial \mathcal{L}}{\partial \rho} \right)_T \right), \qquad (2.49)$$

the growth rate for the fast modes which (for $\mathbf{k} \cdot \mathbf{B}_0 = 0$) have a frequency ω given by

$$\omega^2 = k^2 \left(c_s^2 + v_A^2 \right). \qquad (2.50)$$

It can be seen that the growth rate s_1 is positive (so that the wave modes are overstable) whenever

$$(\gamma - 1) \left[\kappa_\parallel k_\parallel^2 + \kappa_\perp k_\perp^2 + \rho_0 \left(\frac{\partial \mathcal{L}}{\partial T} \right)_\rho \right] + \frac{\rho_0^2}{T_0} \left(\frac{\partial \mathcal{L}}{\partial \rho} \right)_T < 0. \qquad (2.51)$$

This is called the isentropic instability criterion. Finally, setting $\mathbf{k}$ equal to zero (which corresponds to $\rho' = 0$) in Equation (2.38), gives the isochoric instability criterion

$$\left(\frac{\partial \mathcal{L}}{\partial T} \right)_\rho < 0. \qquad (2.52)$$

The wave numbers $k_\parallel$ and $k_\perp$ are both real hence the terms $\kappa_\parallel k_\parallel^2$ and $\kappa_\perp k_\perp^2$ are both positive. Considering these terms in the instability equations (2.42), (2.43) and (2.51), it can be seen that the thermal conducting terms are stabilising. In summary, Equations (2.42) and (2.43) represent the isobaric instability criteria and Equations (2.51) and (2.52) represent the isentropic and isochoric instability criteria respectively.

Chapter 3

The Thermal Continuum in Coronal Loops

As must by now be apparent, we think that the Imp admirably fulfils
this family fun-car role, though it has never enjoyed the success it
deserves. Although conceived more than ten years ago, it still surpasses
many more recent models in the smoothness of its four cylinder engine, the
slickness of its gear change and in the precision of its steering and handling.
    -Review of the Imp in Motor Magazine.

3.1 Overview

In this Chapter, the normal mode spectrum for the linearised MHD equations is investigated for a cylindrical equilibrium. This spectrum is examined for zero perpendicular thermal conduction, with both zero and non-zero scalar resistivity. Particular attention is paid to the continuous branches of this spectrum, or as they are more commonly called, the continuous spectra. For zero resistivity there are three types of continuous spectra present, namely the Alfvén, slow and thermal continua. It is shown that when dissipation due to resistivity is included, the slow and Alfvén continua are removed and the thermal continuum is shifted to a different position (where the shift is independent of the exact value of resistivity). The 'old' location of the thermal continuum is covered by a dense set of nearly singular discrete modes called a quasi-continuum. The quasi-continuum is investigated numerically and the eigenfunctions are shown to have rapid spatial oscillating behaviour. These oscillations are confined to the most unstable part of the equilibrium based on the Field criterion described in Chapter 2 and may be the cause of fine structure in prominences.

3.2 Introduction

The effect of finite, temperature-dependent, scalar resistivity on the thermal continuum is studied in this Chapter. Following the approach used by Van der Linden and Goossens (1991), the normal mode spectrum of the linearised MHD equations is investigated for both zero and non-zero resistivity.

This spectrum can consist of both discrete sub-spectra and continuous sub-spectra. In ideal MHD there are essentially three distinct modes, namely the fast and slow magnetoacoustic modes and the Alfvén modes. When the initial equilibrium state is uniform, these modes describe the oscillations of the plasma. However, the properties of these oscillations are quite different. For example, the fast mode can propagate almost isotropically but Alfvén modes can only transport energy along the direction of

the equilibrium magnetic field. In the limit of large perpendicular wave number, propagation of the slow mode across the field is similarly restricted. In this case, these two modes are unable to communicate information with the plasma on either side of the oscillating field line. For example, a slow mode can propagate along the field to equalise any pressure variations resulting from some initial disturbance, but it cannot equalise pressure variations across the field in an easy manner.

When the initial state is no longer uniform, both the slow mode frequency (or the 'cusp' frequency) in the infinite $k_\perp$ limit and the Alfvén frequency may vary from field line to field line. Because there is no interaction with neighbouring field lines, each field line can oscillate at its own characteristic frequency. This non-uniformity yields a continuous variation of the local values of these frequencies and hence, gives rise to two continuous spectra. In addition to these continuous spectra, there may be discrete sub-spectra corresponding to global Alfvén and slow modes. Investigation of the linearised ideal MHD equations demonstrates that there is a mobile regular singularity at the position where the frequency of the disturbance matches either the local Alfvén or cusp frequency (Goedbloed, 1983). The eigenfunctions are consequently singular at this position. This has led to the conjecture that, when the normal mode decomposition of an arbitrary external disturbance contains 'normal modes' lying within a continuum then the amplitude of the disturbance will become extremely large at the singularities as energy is pumped in from the disturbance to the singularity. Including any dissipation mechanism results in damping of the steep gradients created at this point and the energy is dissipated. Thus, energy can be propagated into the system in the form of wave disturbances and deposited at the resonant layer, where the ideal modes become singular. Resonant absorption of MHD waves due to resonance in either Alfvén or slow mode continuous spectra has been suggested by several authors (for example, Ionson, 1978; Hollweg, 1987a,b; Poedts, Goossens and Kerner, 1989) as a mechanism for heating the solar corona. The existence of such a heating mechanism is due to the anisotropic nature of ideal Alfvén and slow MHD waves.

Recently, Van der Linden, Goossens and Goedbloed (1991) proved the existence of another continuous spectrum which results from the anisotropic nature of heat transport in an optically thin, highly magnetised plasma. Thermal conduction is orders of magnitude more efficient at conducting heat along magnetic field lines than across the field. In addition, optically thin plasma radiation does not transport energy to neighbouring plasma and consequently is incapable of smoothing out cross field variations. The characteristics of the Alfvén and slow mode continuous spectra are therefore present when the non-ideal thermal terms are also included. Van der Linden and Goossens (1991) and Van der Linden (1991) investigated the properties of this 'thermal' continuum in more detail in both planar and cylindrical geometries. In particular, they showed that due to the existence of the thermal continuum, the isobaric thermal instability criterion, derived by Field (1965) for a uniform medium, can be extended to general equilibria.

It is interesting to note that the resonant absorption produced by the Alfvén and slow-mode continua is dependent upon a continual driving of the system by an external source. Normally, it is assumed that disturbances are generated in the convection zone and propagate into the corona. However, a different scenario is possible with thermal effects included. It is now possible that the initial disturbance can trigger an instability in the corona and generate singular behaviour and hence short length scales in the corona, without the need to continually drive the system from outside. Waves impinging on such a small-scale structure will be damped more easily than in the absence of such structure.

The singular nature of the eigenfunctions is normally removed when some dissipation mechanism is included. When resistivity is included as the dissipation mechanism, both the Alfvén continuum and slow continuum are strongly affected (Goedbloed, 1983; Kerner et al., 1985; Poedts, Goossens and Kerner, 1990). The continuous spectrum is replaced by a set of discrete normal modes with complex eigenvalues (including the so-called 'quasi-modes', which are defined in Section 3.4), with a resultant damping of the modes. It has been shown that the resonant absorption mechanism is most efficient

when the frequency of the incoming waves matches the frequency of these global modes. Driving at the quasi-mode frequencies yields very efficient heating (Poedts, Goossens and Kerner, 1990).

Hermans *et al.* (1988) investigated how the slow mode continuum is modified by isotropic thermal conduction. Instead of removing the continuum, isotropic thermal conduction leads to a shift of the slow mode continuum to lower values, the so-called 'isothermal' slow mode continuum.

Van der Linden and Goossens (1991) showed that realistic values of perpendicular thermal conduction have only a small effect on the growth rates predicted by the expression for the thermal continuum, but, that the continuous spectrum is replaced by a dense set of discrete ('quasi-continuum') modes. These quasi-continuum modes exhibit a strong localisation about the previous singular surfaces. They are 'nearly singular' in the sense that the amplitude is large but finite there. For realistic (classical) values of perpendicular thermal conduction the singular mode characteristics and polarisations are still clearly recognisable. Since perpendicular thermal conduction has no significant influence on the growth rates of the most unstable thermal instability, it does not affect the validity of the generalised isobaric instability criterion. It was also noted by Van der Linden and Goossens (1991), that the quasi-continuum branch is continued as an infinite branch of discrete modes below the continuum range, accumulating at $-\infty$ on the real s axis.

The aim of this Chapter is to investigate how the thermal continuum is modified by dissipation due to temperature-dependent, scalar resistivity. Section 3.3 derives the equations describing normal modes and Section 3.4 investigates the basic continuous spectra. The modifications to these continuous spectra due to resistivity and perpendicular thermal conduction are presented in Section 3.5 and applied to a simple cylindrical equilibrium. Section 3.6 presents the numerical results for non-zero resistivity and Section 3.7 summarises the results.

3.3   Basic equations for normal modes

The basic equations used in this Chapter are the standard equations of magnetohydrodynamics in which gravity, viscosity and rotational effects are neglected,

$$\frac{\partial \rho}{\partial t} + \rho \nabla \cdot \mathbf{v} + \mathbf{v} \cdot \nabla \rho = 0, \tag{3.1}$$

$$\rho \left[\frac{\partial \mathbf{v}}{\partial t} + (\mathbf{v} \cdot \nabla) \mathbf{v} \right] = -\nabla p + \frac{1}{\mu} (\nabla \times \mathbf{B}) \times \mathbf{B}, \tag{3.2}$$

$$\frac{\partial \mathbf{B}}{\partial t} = \nabla \times (\mathbf{v} \times \mathbf{B}) - \nabla \times (\eta \nabla \times \mathbf{B}), \tag{3.3}$$

$$p = \frac{\mathcal{R}}{\tilde{\mu}} \rho T, \tag{3.4}$$

$$\frac{\rho^\gamma}{\gamma - 1} \left[\frac{\partial}{\partial t} \left(\frac{p}{\rho^\gamma} \right) + (\mathbf{v} \cdot \nabla) \left(\frac{p}{\rho^\gamma} \right) \right] = \nabla \cdot (\kappa \nabla T) - \rho \mathcal{L} (\rho, T) + \frac{\eta}{\mu} \left| \nabla \times \mathbf{B} \right|^2, \tag{3.5}$$

where all the symbols are defined in Chapter 2.

3.3.1   The general equilibrium equations

The equilibrium configuration used is a static, one-dimensional, infinite, cylindrical plasma, having a magnetic field with axial and azimuthal components depending upon r such that $\nabla \cdot \mathbf{B} = 0$ is identically satisfied. Hence,

$$\mathbf{B}_0 = \left(0, B_{\theta 0}(r), B_{z0}(r) \right). \tag{3.6}$$

All the equilibrium quantities are assumed to be dependent upon the radial distance r only. The momentum equation (3.2) and the energy equation (3.5) consequently become

$$\frac{d}{dr}\left[p_0 + \frac{B_0^2}{2\mu}\right] = -\frac{B_{\theta 0}^2}{\mu r}, \tag{3.7}$$

$$\frac{1}{r}\frac{d}{dr}\left[r\kappa_\perp \frac{dT_0}{dr}\right] + \frac{\eta}{\mu}\left[\left(\frac{dB_{z0}}{dr}\right)^2 + \frac{1}{r^2}\left(\frac{d}{dr}(rB_{\theta 0})\right)^2\right] = \rho_0 \mathcal{L}(\rho_0, T_0). \tag{3.8}$$

The magnetic field diffusion in the equilibrium is neglected because this evolves more slowly than the thermal instability. This implies that the analysis must be restricted to phenomena with time scales that are significantly shorter than the diffusion time scale. Bearing this in mind, the ohmic heating term in Equation (3.8) is likely to be negligible. Once a form for the equilibrium magnetic field has been chosen, Equation (3.7) can be used to find the pressure profile. Then, in theory, Equation (3.8) determines the equilibrium temperature profile T_0 (and hence, using the ideal gas law Equation (3.4), the density profile ρ_0) providing $\mathcal{L}$ is known. Unfortunately no satisfactory form for the coronal heating function h has so far been given. The solution is therefore work the other way round. A realistic temperature profile is chosen and it is assumed that the heating function is such that Equation (3.8) is satisfied. It is also assumed that perturbations of the heating term do not contribute in the linearised equations.

3.3.2   The Gold-Hoyle equilibrium profile

The Gold-Hoyle profile (Gold and Hoyle, 1960) has been used by many authors. In this Chapter, it is force free, isothermal and thus also has a constant density:

$$B_{\theta 0} = B_c \frac{cr}{1 + c^2 r^2}, \qquad \rho_0 = \rho_c,$$

$$B_{z0} = B_c \frac{1}{1 + c^2 r^2}, \qquad p_0 = \beta_c B_c^2/\mu. \tag{3.9}$$

where ρ_c, B_c and β_c represent the values of density, magnetic field strength and plasma beta at the centre of the cylinder axis respectively, while r is the dimensionless radial co-ordinate ranging from 0 to 1, scaled to the radius R of the outer plasma boundary and c a variable parameter which determines the distance at which the external boundary is located. In this work c is taken to be 20, equivalent to placing the boundary of the cylinder at a distance of twenty times the typical loop radius. Three specific types of Gold-Hoyle equilibria are used, each having the same plasma beta ($\beta_c = 0.002$) and density ($\rho_c = 1.6726 \times 10^{-12}$kg m^{-3}), but having different temperatures (and hence magnetic field strengths), and different outer plasma boundaries. In the cold profile, $B_c = 10$G with $R = 10^8$m, while in the cool profile, $B_c = 22.5$G with $R = 10^8$m and in the hot profile, $B_c = 67$G with $R = 10^9$m. The corresponding temperatures are then evaluated using the formula $T_c \equiv \tilde{\mu}B_c^2/(\mathcal{R}\mu\rho_c)$, which gives $T_0 \approx 5.7 \times 10^4$K, 2.9×10^5K and 2.6×10^6K, respectively. In all three equilibrium profiles, the coronal heating function h is constant per unit mass.

3.3.3   Linear perturbations

The standard MHD equations (3.1)-(3.5) are linearised about this equilibrium ($\rho = \rho_0 + \rho_1$, etc.) and the perturbed magnetic field is replaced by a vector potential

$$\mathbf{B}_1 = \nabla \times \mathbf{A}_1, \tag{3.10}$$

thus satisfying $\nabla \cdot \mathbf{B} = 0$ identically. This is substituted into the linearised induction equation which is then integrated to give

$$\frac{\partial \mathbf{A}_1}{\partial t} = \mathbf{v}_1 \times \mathbf{B}_0 - \eta (T_0) \nabla \times (\nabla \times \mathbf{A}_1) - (\nabla \times \mathbf{B}_0) \frac{d\eta}{dT} T_1. \tag{3.11}$$

A gauge function could in principle be added to Equation (3.11). However, the extra degree of freedom it introduces is of no use here. It is therefore set equal to zero. Normal mode solutions are obtained by letting all the perturbed quantities behave like

$$\rho_1 = \rho' (r) \exp [i (m\theta + kz)] e^{st}. \tag{3.12}$$

Introducing velocity components v'_r perpendicular to the flux surface and $v'_\perp$ and $v'_\parallel$ in the flux surface but perpendicular and parallel to the equilibrium magnetic field respectively given by

$$v'_\parallel = \frac{1}{B_0} (B_{\theta 0} v'_\theta + B_{z0} v'_z), \tag{3.13}$$

$$v'_\perp = \frac{1}{B_0} (B_{z0} v'_\theta - B_{\theta 0} v'_z), \tag{3.14}$$

and dropping the '0' subscripts for ease of writing, it is found that the linearised equations for temperature-dependent scalar resistivity become

$$s\rho' = -\frac{1}{r}\frac{d}{dr}(r\rho v'_r) - \frac{i\rho f}{B}v'_\parallel - \frac{i\rho g}{B}v'_\perp, \tag{3.15}$$

$$s\rho v'_r = -\frac{d}{dr}\left[\frac{p}{T}T' + \frac{p}{\rho}\rho' - \frac{ig}{\mu}A'_r - \frac{B_\theta}{\mu}\frac{dA'_z}{dr} + \frac{B_z}{\mu r}\frac{d}{dr}(rA'_\theta)\right]$$
$$- \frac{2ikB_\theta}{\mu r}A'_r + \frac{kf}{\mu}A'_\theta + \frac{2B_\theta}{\mu r}\frac{dA'_z}{dr} - \frac{mf}{\mu r}A'_z, \tag{3.16}$$

$$s\rho r B i v'_\perp = \frac{pgr}{T}T' + \frac{pgr}{\rho}\rho' + \frac{mB^2}{\mu r}\frac{d}{dr}(rA'_\theta) + \frac{kB^2 r}{\mu}\frac{dA'_z}{dr} - \frac{B^2 r}{\mu}\left(\frac{m^2}{r^2} + k^2\right)iA'_r$$
$$+ \frac{1}{\mu}\left(\frac{B_\theta B_z}{r} + B_z\frac{dB_\theta}{dr} - B_\theta\frac{dB_z}{dr}\right)(krA'_\theta - mA'_z), \tag{3.17}$$

$$s\rho B i r v'_\parallel = \frac{frp}{T}T' + \frac{frp}{\rho}\rho' - kr\frac{dp}{dr}A'_\theta + m\frac{dp}{dr}A'_z, \tag{3.18}$$

$$sA'_r = Bv'_\perp - \frac{im\eta}{r^2}\frac{d}{dr}(rA'_\theta) - \eta\left(\frac{m^2}{r^2} + k^2\right)A'_r - ik\eta\frac{dA'_z}{dr}, \tag{3.19}$$

$$sA'_\theta = -B_z v'_r + \eta\frac{d}{dr}\left[\frac{1}{r}\frac{d}{dr}(rA'_\theta)\right] - im\eta\frac{d}{dr}\left(\frac{A'_r}{r}\right) + \frac{km\eta}{r}A'_z - k^2\eta A'_\theta + \frac{d\eta}{dT}\frac{dB_z}{dr}T', \tag{3.20}$$

$$sA'_z = B_\theta v'_r - \frac{ik\eta}{r}\frac{d}{dr}(rA'_r) + \frac{\eta}{r}\frac{d}{dr}\left(r\frac{dA'_z}{dr}\right) - \frac{m^2\eta}{r^2}A'_z + \frac{mk\eta}{r}A'_\theta - \frac{1}{r}\frac{d\eta}{dT}\frac{d}{dr}(rB_\theta)T', \tag{3.21}$$

$$s\rho C_v T' = -\rho C_v \frac{dT}{dr} v_r' - \frac{p}{r}\frac{d}{dr}(rv_r') - \frac{ipf}{B}v_\parallel' - \frac{ipg}{B}v_\perp'$$

$$+ \frac{d\kappa_\perp}{dr}\frac{dT'}{dr} + \frac{\kappa_\perp}{r}\frac{d}{dr}\left(r\frac{dT'}{dr}\right) - \left[\left(\frac{m^2}{r^2}+k^2\right)\kappa_\perp + \frac{f^2}{B^2}(\kappa_\parallel-\kappa_\perp)\right]T'$$

$$- \left(\mathcal{L}+\rho\left(\frac{\partial\mathcal{L}}{\partial\rho}\right)_T\right)\rho' - \rho\left(\frac{\partial\mathcal{L}}{\partial T}\right)_\rho T' + \frac{f}{rB^2}(\kappa_\parallel-\kappa_\perp)\frac{dT}{dr}(rkA_\theta'-mA_z')$$

$$+ \frac{1}{r}\frac{d}{dr}\left[\left(r\frac{\partial\kappa_\perp}{\partial\rho}\rho' + r\frac{\partial\kappa_\perp}{\partial T}T' - 2rB_\theta\frac{\partial\kappa_\perp}{\partial B^2}\frac{dA_z'}{dr} + 2B_z\frac{\partial\kappa_\perp}{\partial B^2}\frac{d}{dr}(rA_\theta') - 2irg\frac{\partial\kappa_\perp}{\partial B^2}A_r'\right)\frac{dT}{dr}\right]$$

$$+ \frac{2\eta}{\mu}\frac{dB_z}{dr}\left[\frac{km}{r}A_z' - k^2A_\theta' + \frac{d}{dr}\left(\frac{1}{r}\frac{d}{dr}(rA_\theta')\right) - im\frac{d}{dr}\left(\frac{A_r'}{r}\right)\right]$$

$$+ \frac{2\eta}{r^2\mu}\frac{d}{dr}(rB_\theta)\left[ik\frac{d}{dr}(rA_r') - \frac{d}{dr}\left(r\frac{dA_z'}{dr}\right) + \frac{m^2}{r}A_z' - mkA_\theta'\right]$$

$$+ \frac{1}{\mu}\frac{d\eta}{dT}\left[\left(\frac{dB_z}{dr}\right)^2 + \frac{1}{r^2}\left(\frac{d}{dr}(rB_\theta)\right)^2\right]T', \tag{3.22}$$

$$p' = \frac{p}{T}T' + \frac{p}{\rho}\rho', \tag{3.23}$$

where

$$f = \frac{mB_\theta}{r} + kB_z, \qquad g = \frac{mB_z}{r} - kB_\theta, \qquad C_v = \frac{\mathcal{R}}{\widetilde{\mu}(\gamma-1)}. \tag{3.24}$$

3.4 Basic Continuous Spectra

The normal mode spectrum of the linearised MHD equations can consist of both discrete sub-spectra and continuous sub-spectra which are investigated here for a one-dimensional cylindrical plasma.

3.4.1 Continuous spectra in the ideal case

To obtain the continuous spectra for a perfectly conducting cylindrical plasma, the non-ideal terms in Equations (3.15)-(3.23) are neglected. The resulting equations are then transformed to give

$$\frac{d}{dr}\left[\frac{rN}{r^2D}\frac{d}{dr}(rv_r')\right] + \left[-\frac{1}{r}\left(s^2\rho+\frac{f^2}{\mu}\right) - \frac{d}{dr}\left(\frac{B_\theta^2}{\mu r^2}\right) + \frac{4k^2B_\theta^2}{\mu^2 r^3 D}(B^2s^2\rho+\gamma pf^2)\right.$$

$$\left. - \frac{d}{dr}\left(\frac{2kB_\theta g}{\mu r^2 D}\left(s^2\rho\left(\gamma p+\frac{B^2}{\mu}\right)+\frac{\gamma pf^2}{\mu}\right)\right)\right](rv_r') = 0, \tag{3.25}$$

where

$$N = \left(s^2\rho+\frac{f^2}{\mu}\right)\left[s^2\rho\left(\gamma p+\frac{B^2}{\mu}\right)+\frac{\gamma pf^2}{\mu}\right], \tag{3.26}$$

and

$$D = s^4\rho^2 + \left(k^2+\frac{m^2}{r^2}\right)\left[s^2\rho\left(\gamma p+\frac{B^2}{\mu}\right)+\frac{\gamma pf^2}{\mu}\right]. \tag{3.27}$$

Equation (3.25) is the Hain-Lüst equation first derived by Hain and Lüst (1958). The Hain-Lüst equation (3.25) yields important information about the layout of the ideal normal mode spectrum. The mobile regular singular points in the Hain-Lüst equation correspond to continuous spectra, see Goedbloed (1983). These singularities are given by $N = 0$. Hence, either

$$s^2 \rho + \frac{f^2}{\mu} = 0, \tag{3.28}$$

or

$$s^2 \rho \left(\gamma p + \frac{B^2}{\mu} \right) + \frac{\gamma p f^2}{\mu} = 0. \tag{3.29}$$

Equation (3.28) represents the Alfvén continuum and Equation (3.29) represents the slow mode continuum. The zeros given by $D = 0$ are also important in ideal MHD. These are given by

$$s^2 = -\frac{1}{2\rho} \left(k^2 + \frac{m^2}{r^2} \right) \left(\gamma p + \frac{B^2}{\mu} \right) \left[1 \pm \sqrt{1 - \frac{4 \gamma p f^2}{\mu} \left(k^2 + \frac{m^2}{r^2} \right)^{-1} \left(\gamma p + \frac{B^2}{\mu} \right)^{-2}} \right]. \tag{3.30}$$

The growth rate s is imaginary in Equations (3.28)-(3.30). These imaginary growth rates ($s^2 \equiv -\omega^2$) are equivalent to four frequencies ω_A, ω_s, ω_1 and ω_2, where ω_1 and ω_2 correspond to the plus and minus signs of the square root in Equation (3.30) respectively.

Originally, it was first thought by Grad (1973) that the two solutions (or frequencies) given by Equation (3.30) defined two more continua. He concluded that for a perfectly conducting, cylindrical plasma, the spectrum of the MHD equations contained four distinct continua. However, Appert, Gruber and Vaclavik (1974) rewrote the Hain-Lüst equation (3.25) as a system of two first-order ordinary differential equations which had singularities given only by $N = 0$. They therefore concluded that the zeros corresponding to $D = 0$ were apparent singularities and did not correspond to continuous spectra. Goedbloed and Sakanaka (1974) went a stage further and showed that the two frequencies ω_1 and ω_2 represented regions of non-monotonicity. (These frequencies separate the regions of Sturmian and anti-Sturmian behaviour of the discrete sub-spectra, see later.)

So far, the discrete sub-spectra has yet to be addressed. It has been shown (see Goedbloed, 1984 and references therein) that the three MHD waves (Alfvén and the fast and slow magnetoacoustic waves) can be split into five sets of discrete sub-spectra. It has also been shown (see, for example, Goedbloed, 1983, 1984) that discrete Alfvén and slow modes accumulate at the tips of the Alfvén the slow mode continua respectively, while the fast modes accumulate at infinity. The discrete Alfvén modes found below the Alfvén continuum exhibit Sturmian behaviour (the frequency of the modes monotonically increases with wave number) while the discrete Alfvén modes found above the Alfvén continuum are anti-Sturmian (the frequency of the modes monotonically decreases with wave number). A similar result also holds for the discrete slow modes found above and below the slow mode continuum, while the fast modes are Sturmian (for details, see Goedbloed, 1984).

The complete layout of the ideal MHD spectrum can now be assessed for a general equilibrium with weak inhomogeneities. This yields distinct frequencies for ω_1, ω_2, ω_A and ω_s. The Alfvén and slow mode continua therefore do not overlap. The complete spectrum is shown in Figure 3.1. It is important to note that the exact layout of the normal mode specrum depends on the equilibrium considered. It is possible to generate a complete axis of continua and have no discrete sub-spectra, see later. It is also possible that for some equilibria, one or more branches of the discrete sub-spectra may be absent. Under some circumstances, unstable Alfvén modes may be present, see Chapter 4.

There is still one more situation that has to be addressed. This usually occurs at the plasma interface, but can also happen whenever the equilibium density tends to zero. The frequency of the Alfvén continuum is given by

$$\omega_A = \pm\sqrt{\frac{f^2}{\mu\rho}}, \tag{3.31}$$

and so as $\rho \to 0$, $\omega_A \to \infty$. Hence, the Alfvén continuum contains the fast discrete sub-spectra as quasi-modes.
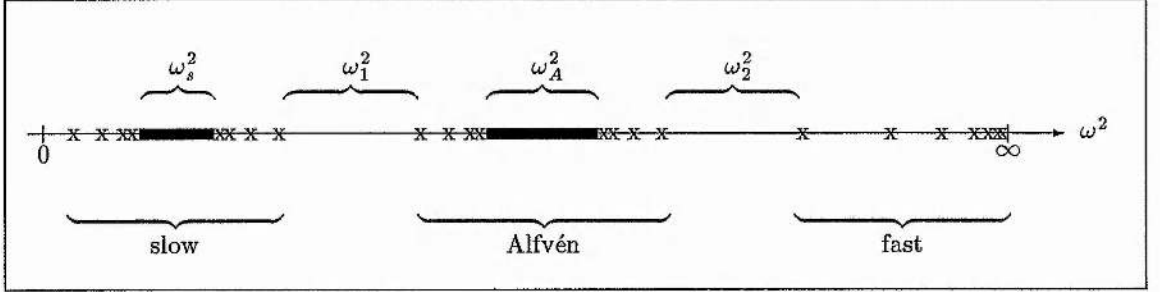
Figure 3.1: The typical layout of the ideal MHD normal mode spectrum for a general equilibrium with weak inhomogeneities. The frequencies ω_1 and ω_2 are the imaginary parts of the growth rates ($\omega^2 \equiv -s^2$) defined by Equation (3.30) and ω_s and ω_A are the Alfvén the slow mode continua frequencies, respectively. (After Goedbloed *et al.*, 1973).

Notice that the slow mode continuum contains both the Alfvén and fast sub-spectra as $\rho \to 0$ or if $\gamma p + B^2/\mu \to 0$. In addition, if there is a point in the equilibrium where $f \equiv \mathbf{k} \cdot \mathbf{B}_0 = 0$, then both the Alfvén and the slow mode continua both have minima at $\omega_A^2 = \omega_s^2 = 0$. In this case, the whole of the ω axis is covered by continua. In this situation, both the Alfvén and the slow mode continua overlap and a complicated problem arises.

Finally, it should also noticed that there is no continuous spectrum along the real s axis in ideal MHD.

3.4.2 Continuous spectra for zero perpendicular thermal conduction and zero resistivity

It has been demonstrated by Van der Linden and Goossens (1991) that for zero perpendicular thermal conduction and zero resistivity, Equations (3.15)-(3.23) can be transformed into the following second-order ordinary differential equation

$$\frac{d}{dr}\left[F\left(r\right) \frac{d}{dr}\left(rv_r'\right) \right] + G\left(r\right)\left(rv_r'\right) = 0, \tag{3.32}$$

where

$$F\left(r\right) = \left(s^2\rho + \frac{f^2}{\mu} \right) \frac{rC_t}{C}, \tag{3.33}$$

$$G\left(r\right) = \frac{1}{r}\left(s^2\rho + \frac{f^2}{\mu} \right) + \frac{d}{dr}\left(\frac{B_\theta^2}{\mu r^2} \right) + \frac{4k^2 f^2 p B_\theta^2}{\mu^2 rCT}\left[sp - \rho^2 \left(\frac{\partial \mathcal{L}}{\partial \rho} \right)_T \right]$$

$$+ \frac{4k^2 B_\theta^2}{\mu^2 rC}\left(pf^2 + \rho s^2 B^2 \right)\left[s\rho C_v + \rho \left(\frac{\partial \mathcal{L}}{\partial T} \right)_\rho + \frac{\kappa_\parallel f^2}{B^2} \right] - \frac{2k}{\mu}\frac{d}{dr}\left(\frac{gC_t B_\theta}{C} \right), \tag{3.34}$$

with

$$C = -r^2 \left(k^2 + \frac{m^2}{r^2} \right) C_t - r^2 \rho^2 s^4 \left[s\rho C_v + \rho \left(\frac{\partial \mathcal{L}}{\partial T} \right)_\rho + \frac{\kappa_\parallel f^2}{B^2} \right], \tag{3.35}$$

and

$$C_t = s\rho C_v \left[s^2 \rho \left(\gamma p + \frac{B^2}{\mu} \right) + \frac{\gamma p f^2}{\mu} \right] - \left(s^2 \rho + \frac{f^2}{\mu} \right) \frac{\rho^2 p}{T} \left(\frac{\partial \mathcal{L}}{\partial \rho} \right)_T$$

$$+ \left[\frac{\kappa_\parallel f^2}{B^2} + \rho \left(\frac{\partial \mathcal{L}}{\partial T} \right)_\rho \right] \left[s^2 \rho \left(p + \frac{B^2}{\mu} \right) + \frac{p f^2}{\mu} \right]. \tag{3.36}$$

Equation (3.36) is a third-order polynomial in s and can be written as

$$C_t = \left[\rho^2 C_v \left(\gamma p + \frac{B^2}{\mu} \right) \right] s^3 + \left[\rho \left(p + \frac{B^2}{\mu} \right) \left(\rho \left(\frac{\partial \mathcal{L}}{\partial T} \right)_\rho + \frac{\kappa_\parallel f^2}{B^2} \right) - \frac{\rho^3 p}{T} \left(\frac{\partial \mathcal{L}}{\partial \rho} \right)_T \right] s^2$$

$$+ \left[\frac{\rho C_v \gamma p f^2}{\mu} \right] s + \left[\frac{p f^2}{\mu} \left(\rho \left(\frac{\partial \mathcal{L}}{\partial T} \right)_\rho + \frac{\kappa_\parallel f^2}{B^2} \right) - \frac{f^2 \rho^2 p}{\mu T} \left(\frac{\partial \mathcal{L}}{\partial \rho} \right)_T \right]. \tag{3.37}$$

It should be noted that Equation (3.32) is formally identical to the Hain-Lüst equation (3.25) when the non-ideal terms are neglected. This modified Hain-Lüst equation has singularities (and hence continuous spectra) given by

$$\left(s^2 \rho + \frac{f^2}{\mu} \right) C_t = 0. \tag{3.38}$$

To satisfy Equation (3.38) either

$$s^2 \rho + \frac{f^2}{\mu} = 0, \tag{3.39}$$

or

$$C_t = 0. \tag{3.40}$$

Equation (3.39) again defines the Alfvén continuum. Since Equation (3.40) is a cubic in s there are three solutions for a fixed radial co-ordinate r. Neglecting the non-ideal terms in Equation (3.36) gives

$$C_{t_{ideal}} = s\rho C_v \left[s^2 \rho \left(\gamma p + \frac{B^2}{\mu} \right) + \frac{\gamma p f^2}{\mu} \right], \tag{3.41}$$

and so either

$$s = 0, \tag{3.42}$$

or

$$s = i\sqrt{\frac{\gamma p f^2}{\rho \left(\mu \gamma p + B^2 \right)}}. \tag{3.43}$$

The real root, $s = 0$, corresponds to the ideal remnant of the thermal continuum. The two purely imaginary solutions given by Equation (3.43) correspond to the ideal slow continuum. Since the non-adiabatic terms are assumed to be small, in general their inclusion will add a small correction to the ideal slow continuum. In most cases Equation (3.40) therefore has two complex roots corresponding to the modified slow continuum and one real root corresponding to the thermal continuum.

3.5   Continuous Spectra with Dissipation

3.5.1   Continuous spectrum for non-zero perpendicular thermal conduction and zero resistivity

It has also been shown (Van der Linden and Goossens, 1991) that for non-zero perpendicular thermal conduction and zero resistivity, the continuous spectra are given by

$$\left[s^2 \rho + \frac{f^2}{\mu} \right] \left[s^2 \rho \left(p + \frac{B^2}{\mu} \right) + \frac{pf^2}{\mu} \right] \;=\; 0. \tag{3.44}$$

Therefore, either

$$s^2 \rho + \frac{f^2}{\mu} \;=\; 0, \tag{3.45}$$

or

$$s^2 \rho \left(p + \frac{B^2}{\mu} \right) + \frac{pf^2}{\mu} \;=\; 0. \tag{3.46}$$

Equation (3.45) again defines the Alfvén continuum. Equation (3.46) defines the isothermal continuum, which is the modified slow continuum (see also Hermans *et al.* (1988) who demonstrated that the above two continua exist when dissipation due to anisotropic thermal conduction is included).

3.5.2   Continuous spectra for zero perpendicular thermal conduction but non-zero resistivity

In ideal MHD it is well known that mobile regular singular points in the linear differential equations correspond to bands of singular wave solutions, or continuous spectra (see, for example, Goedbloed, 1983). Hence to derive the continuous spectrum for a one-dimensional cylindrical equilibrium, with resistivity included, singularities are looked for in the equations obtained by transforming Equations (3.15)-(3.23) into a set of six first-order ordinary differential equations. Introducing the total perturbed pressure P' given by

$$P' \;=\; p' + \frac{1}{\mu} \left(B_\theta B'_\theta + B_z B'_z \right), \tag{3.47}$$

setting perpendicular thermal conduction to zero, letting resistivity be constant in Equations (3.20)-(3.22) and after performing some fairly straightforward but lengthy algebra, the following system of differential equations is obtained

$$s \rho r p \left[s + \eta \left(\frac{m^2}{r^2} + k^2 \right) \right] C_0 \frac{dv'_r}{dr} \;=\; C_1 B'_\theta + C_2 v'_r + C_3 \psi + C_4 \zeta + C_5 B'_z + C_6 P', \tag{3.48}$$

$$\left[s + \eta \left(\frac{m^2}{r^2} + k^2 \right) \right] \frac{dP'}{dr} \;=\; C_7 v'_r + C_8 B'_\theta + C_9 \psi + C_{10} \zeta, \tag{3.49}$$

$$s \rho \eta \left[s + \eta \left(\frac{m^2}{r^2} + k^2 \right) \right] C_0 \frac{d\zeta}{dr} \;=\; C_{11} P' + C_{12} B'_\theta + C_{13} B'_z + C_{14} v'_r + C_{15} \psi + C_{16} \zeta, \tag{3.50}$$

$$s \rho \eta \left[s + \eta \left(\frac{m^2}{r^2} + k^2 \right) \right] C_0 \frac{d\psi}{dr} \;=\; C_{17} P' + C_{18} B'_\theta + C_{19} v'_r + C_{20} B'_z + C_{21} \psi + C_{22} \zeta, \tag{3.51}$$

$$\frac{dB'_\theta}{dr} \;=\; \psi, \tag{3.52}$$

$$\frac{dB'_z}{dr} = \zeta, \tag{3.53}$$

where the coefficients $C_1 - C_{22}$ are given in Appendix A and

$$C_0 = s\rho\gamma C_v + \frac{f^2\kappa_{\parallel}}{B^2} + \rho\left(\frac{\partial\mathcal{L}}{\partial T}\right)_\rho - \frac{\rho}{T}\left[\mathcal{L} + \rho\left(\frac{\partial\mathcal{L}}{\partial\rho}\right)_T\right]. \tag{3.54}$$

When resistivity is set equal to zero, it can be shown after more algebra that Equations (3.48)-(3.53) reduce to the modified Hain-Lüst equation (3.32). It can now be seen that the differential equations (3.48)-(3.53) have singularities (and hence continuous spectra) given by

$$s + \eta\left(\frac{m^2}{r^2} + k^2\right) = 0, \tag{3.55}$$

and

$$s\rho\gamma C_v + \frac{f^2\kappa_{\parallel}}{B^2} + \rho\left(\frac{\partial\mathcal{L}}{\partial T}\right)_\rho - \frac{\rho}{T}\left[\mathcal{L} + \rho\left(\frac{\partial\mathcal{L}}{\partial\rho}\right)_T\right] = 0. \tag{3.56}$$

The former is diffusion which is neglected as before, whereas the latter is the thermal continuum for non-zero, constant resistivity and zero perpendicular thermal conduction. Furthermore, it can be shown that for temperature-dependent resistivity, given by Equation (2.6), the thermal continuum becomes

$$s\rho\gamma C_v + \frac{f^2\kappa_{\parallel}}{B^2} + \rho\left(\frac{\partial\mathcal{L}}{\partial T}\right)_\rho - \frac{\rho}{T}\left[\mathcal{L} + \rho\left(\frac{\partial\mathcal{L}}{\partial\rho}\right)_T\right] + \frac{1}{\mu}\frac{d\eta}{dT}\left[\left(\frac{dB_z}{dr}\right)^2 + \frac{1}{r^2}\left(\frac{d}{dr}(rB_\theta)\right)^2\right] = 0. \tag{3.57}$$
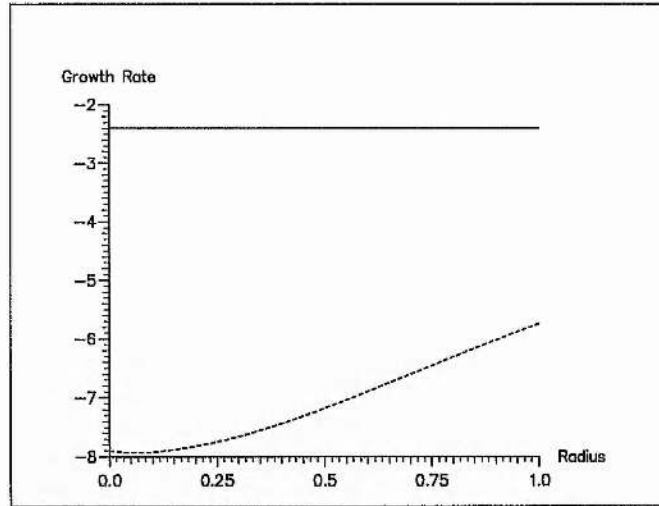
Figure 3.2(a): The thermal continua growth rates for the cold Gold-Hoyle profile with $c = 20$ in Equation (3.9) and wave numbers $k = m = 1$. Notice that the wavenumber k has been non-dimensionalised, see Appendix C. The solid line represents the thermal continuum for non-zero resistivity whilst the dashed line represents the thermal continuum for zero resistivity. The growth rate has been scaled in terms of the Alfvén time scale and the radius in terms of the outer boundary.

The singularities corresponding to Equations (3.56) and (3.57) can also be obtained using the infinite gradient method, discussed in more detail in Appendix B and Goossens, Poedts and Hermans (1985). In Equation (3.57), as in Section 3.3, the ohmic heating term and $\mathcal{L}$ are neglected.
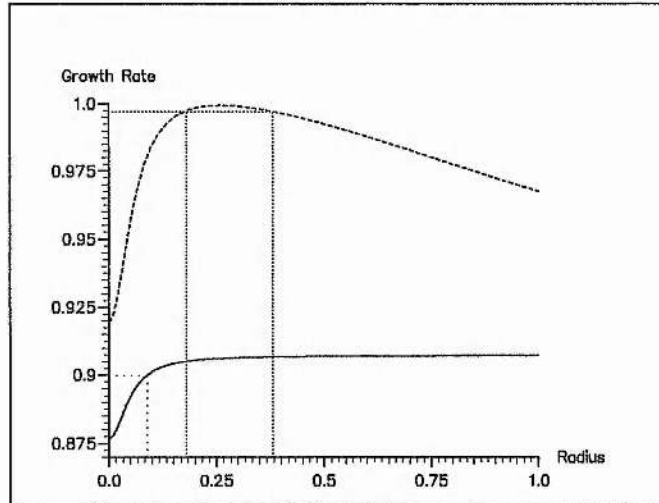
Figure 3.2(b): As in Figure 3.2(a) but for the cool Gold-Hoyle profile with $B_c = 22.5$G in the equilibrium equations and $R = 10^8$m. The corresponding temperature is 2.9×10^5K. The dense dotted lines show the positions of the two singularities which correspond to a growth rate of 0.997 as used in Figure 3.6, while the less dense dotted lines show the expected position of the singularity corresponding to a growth rate of 0.89996 as used in Figure 3.4.
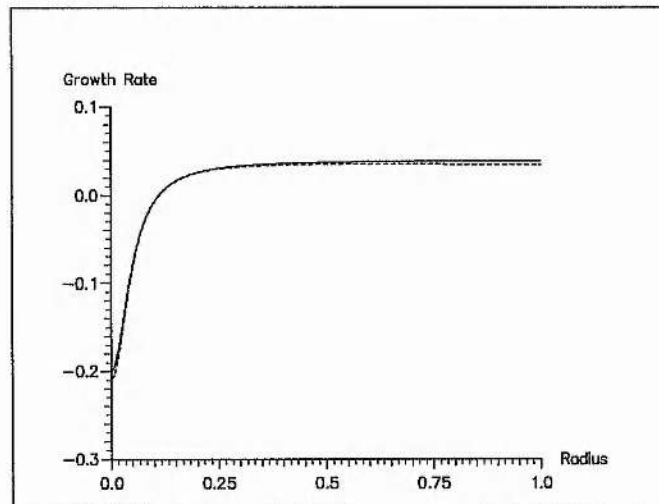
Figure 3.2(c): As in Figure 3.1(a) but for the hot Gold-Hoyle profile with $B_c = 67$G in the equilibrium equations and $R = 10^9$m. The corresponding temperature is 2.6×10^6K.

In Equation (3.56), there are no terms involving resistivity. Therefore the exact value of resistivity does not influence the thermal continuum. Comparing Equations (3.37) and (3.56), it can be seen that if terms

of order s^2 and above are neglected in Equation (3.37) it reduces to Equation (3.56). This is surprising when considering that Equation (3.56) is the singularity of the sixth-order differential equation obtained by re-writing Equations (3.48)-(3.53), whereas Equation (3.37) is the singularity of the second-order differential equation derived by Van der Linden and Goossens (1991) for zero perpendicular thermal conduction and zero resistivity. The thermal continua for both zero resistivity and non-zero constant resistivity are compared in Figure 3.1. In each of the three cases, the thermal continua are plotted for the three types of Gold-Hoyle equilibrium profiles described earlier, with $c = 20$ in Equations (3.9) and wave numbers $m = k = 1$. The dashed line is the thermal continuum for zero resistivity and the solid line the thermal continuum for non-zero constant resistivity. The curves show the local continuum eigenvalue (scaled to the Alfvén transit time given by $\tau_A = R\sqrt{\mu \rho_c}/B_c$) as a function of the cylinder radius r. In Figures 3.2(a) and 3.2(b) it can be seen that the two thermal continua plotted have considerably different growth rates. In these equilibria the thermal continuum for zero perpendicular thermal conduction and zero resistivity is removed by resistivity and is replaced by a dense set of discrete modes, called a quasi-continuum. However, in Figure 3.2(c) it can be seen that the two curves are almost identical. Closer inspection reveals the fact that the growth rates are much smaller in magnitude compared to that found in Figures 3.2(a) and 3.2(b). In this equilibrium, the thermal time scale is much smaller than the Alfvén time scale and so in the expression for the thermal continuum with zero perpendicular thermal conduction and zero resistivity given by Equation (3.40), terms of order s^2 can be neglected, giving an expression very similar to that for the thermal continuum for non-zero resistivity given by Equation (3.57). Hence, for the hot Gold-Hoyle equilibrium profile there is no quasi-continuum present. For a general equilibrium profile it would therefore be expected that resistivity would replace the thermal continuum for zero perpendicular thermal conduction and zero resistivity by a quasi-continuum, except when the thermal time scale is much smaller than the Alfvén time scale.

3.5.3   Sufficient Conditions for Thermal Instability

It is mathematically very easy to obtain continuum solutions for certain values of r since they are just solutions to either the cubic equation (3.40) for zero resistivity or the linear equation (3.57) for non-zero resistivity. Knowledge of the thermal continuum can be used to formulate sufficient conditions for the onset of thermal instability. Since continuum solutions are also solutions to the full eigenvalue problem, it can be deduced that a given equilibrium is thermally unstable if the thermal continuum is partially or completely contained in the positive real s-axis.

For zero resistivity and zero perpendicular thermal conduction, the slow and thermal continua correspond to the solutions of the cubic equation (3.40). This can be rearranged to give

$$
\left(c_s^2 + v_A^2\right)s^3 + \frac{\left(c_i^2 + v_A^2\right)}{C_v \rho}\left[\frac{\kappa_\parallel f^2}{B^2} + \rho\left(\frac{\partial \mathcal{L}}{\partial T}\right)_\rho - \frac{c_i^2 \rho^2}{T\left(c_i^2 + v_A^2\right)}\left(\frac{\partial \mathcal{L}}{\partial \rho}\right)_T\right]s^2
$$

$$
+ \; \frac{f^2}{\mu \rho}c_s^2 s + \frac{c_i^2}{C_v \rho}\frac{f^2}{\mu \rho}\left[\frac{\kappa_\parallel f^2}{B^2} + \rho\left(\frac{\partial \mathcal{L}}{\partial T}\right)_\rho - \frac{\rho^2}{T}\left(\frac{\partial \mathcal{L}}{\partial \rho}\right)_T\right] \; = \; 0, \tag{3.58}
$$

where c_s is the sound speed, c_i is the isothermal sound speed and v_A is the Alfvén speed defined by

$$
c_s^2 \; = \; \frac{\gamma p}{\rho}, \qquad c_i^2 \; = \; \frac{p}{\rho}, \qquad v_A^2 \; = \; \frac{B^2}{\mu \rho}. \tag{3.59}
$$

To investigate when an equilibrium will be thermally unstable, the roots of the Equation (3.58) are examined. For $f \equiv \mathbf{k} \cdot \mathbf{B} \neq 0$, Equation (3.58) will have at least one positive real root whenever

$$
\frac{\kappa_\parallel f^2}{B^2} + \rho\left(\frac{\partial \mathcal{L}}{\partial T}\right)_\rho - \frac{\rho^2}{T}\left(\frac{\partial \mathcal{L}}{\partial \rho}\right)_T \; < \; 0 \qquad \text{(for } \mathbf{k} \cdot \mathbf{B} \neq 0\text{)}. \tag{3.60}
$$

If $\mathbf{k} \cdot \mathbf{B} = 0$, the last two terms in Equation (3.58) vanish. Thus Equation (3.58) simplifies and has at least one positive real solution whenever

$$\rho \left(\frac{\partial \mathcal{L}}{\partial T} \right)_\rho - \frac{c_i^2 \rho^2}{T \left(c_i^2 + v_A^2 \right)} \left(\frac{\partial \mathcal{L}}{\partial \rho} \right)_T \ < \ 0 \qquad \text{(for } \mathbf{k} \cdot \mathbf{B} = 0 \text{)}. \tag{3.61}$$

Equations (3.60) and (3.61) are the isobaric instability criteria for a uniform infinite medium (see Chapter 2 and Field, 1965). It can also be shown that the slow continuum can become overstable whenever

$$(\gamma - 1) \left[\frac{\kappa_\| f^2}{B^2} + \rho \left(\frac{\partial \mathcal{L}}{\partial T} \right)_\rho \right] + \frac{\rho^2}{T} \left(\frac{\partial \mathcal{L}}{\partial \rho} \right)_T \ < \ 0. \tag{3.62}$$

This is recornised as the isentropic instability criterion for a uniform infinite plasma (see Chapter 2).

A similar, less complicated, analysis can be performed for non-zero resistivity and zero perpendicular thermal conduction. Setting $\mathcal{L}$ equal to zero and neglecting the ohmic heating term in the expression for the thermal continuum for non-zero resistivity given by Equation (3.57), it can be seen that the condition for an equilibrium to be thermally unstable at any r and any allowable wave numbers k and m is

$$\frac{\kappa_\| f^2}{B^2} + \rho \left(\frac{\partial \mathcal{L}}{\partial T} \right)_\rho - \frac{\rho^2}{T} \left(\frac{\partial \mathcal{L}}{\partial \rho} \right)_T \ < \ 0. \tag{3.63}$$

As before, this is recognised as the isobaric instability criterion for an infinite uniform medium. Examining Figure 3.2 it is found that the cold Gold-Hoyle profile is thermally stable whereas, the hot and cool profiles are both thermally unstable for the wave numbers $k = m = 1$.

The question arises as to whether these sufficient conditions for thermal instability are also necessary conditions as well. The answer is generally no because the thermal sub-spectrum may contain discrete modes in addition to the thermal continuum.

3.6 Numerical Results for Finite Resistivity

It can be readily seen from the previous Sections that the inclusion of finite resistivity removes the Alfvén continuum given by Equation (3.45) and replaces the cubic equation (3.40) (which represents the thermal continuum for zero resistivity and zero perpendicular thermal conduction, and the slow continuum), by the linear equation (3.57) (which represents the thermal continuum for non-zero resistivity). In doing so the slow continuum is also removed and the thermal continuum for zero resistivity and zero perpendicular thermal conduction is usually replaced by a dense set of discrete modes, called a quasi-continuum. This quasi-continuum is investigated numerically using the finite element code LEDA (Large-scale Eigenvalue solver for the Dissipative Alfvén spectrum). A detailed description of LEDA can be found in Appendix C. The general eigenvalue problem given by Equations (3.15)-(3.23) is then solved by two different algorithms. The first, the QR method (Kerner, 1989) gives the eigenvalues. Once these are known, they can be used in the Inverse Vector Iteration algorithm, (Kerner, 1989), to calculate and plot the eigenfunctions. In this Section, attention is restricted to the cool Gold-Hoyle equilibrium profile with wave numbers $k = m = 1$. In any study of the normal mode spectrum for a given equilibrium, it is essential to get a good idea of the global picture before restricting attention to specific areas. Hence, two QR plots are given in this Section to illustrate the ideas in the previous Sections.

Both are calculated using 50 gridpoints. In Figure 3.3(a), the situation where resistivity is zero is considered and in Figure 3.3(b) the unrealistically low value of $R_m = 1$. Notice that in both diagrams, the thermal continuum is located in approximately the same position.
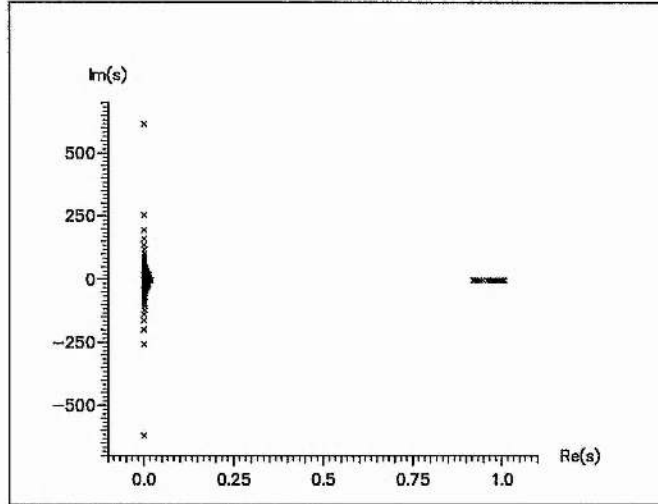
Figure 3.3(a): The QR plot with 50 gridpoints for the cool Gold-Hoyle profile with zero resistivity. Notice that the thermal continuum is clearly visible along the real s axis.
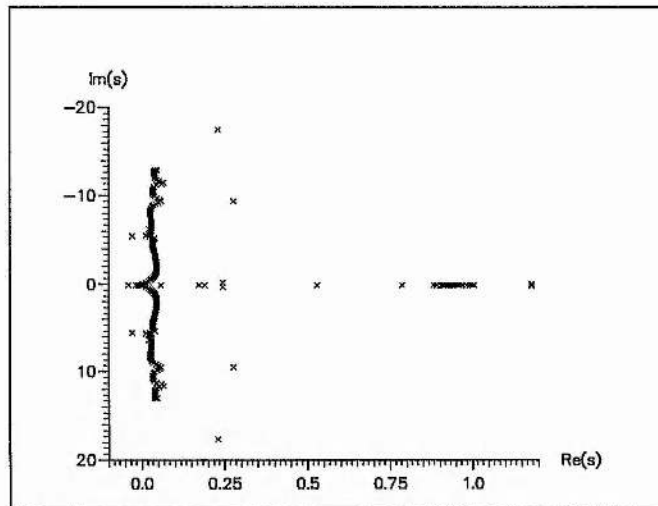
Figure 3.3(b): The QR plot with 50 gridpoints for the cool Gold-Hoyle profile with $R_m = 1$. Even for this unrealistically low value of R_m, the thermal continuum can still seen along the real s axis.

In Figure 3.3(b), it can be seen that the thermal continuum has shifted a small distance along the real s axis. Notice also the effect resistivity has on the slow and Alfvén modes. Now that the QR plots have been worked out, attention may be diverted to the thermal sub-spectrum.

Two sets of six graphs are provided here, each calculated using 1,000 gridpoints. These Figures show how the real part of the $v_\perp$ eigenfunction (scaled to the Alfvén time scale $\tau_A = R\sqrt{\mu \rho_c}/B_c$ which is typically taken to be 5 seconds in the solar corona) evolves with various values of resistivity. The $v_\perp$ eigenfunction was chosen because it best illustrates these changes. It should be noted that the same effects are seen in all the eigenfunctions. In each case the only parameter that is varied is the magnetic Reynolds number R_m. In Figure 3.4 the singular behaviour of the thermal continuum for non-zero resistivity is shown. Here $R_m = 1$ and the singular behaviour occurs at $r = 0.0886$, just as predicted by the less dense dotted line in Figure 3.2(b). In Figure 3.5 the most unstable mode (largest growth rate) of the thermal 'quasi-continuum' is followed as the value of resistivity is increased. For zero resistivity, the singularity is clearly seen at $r = 0.26$. Comparison with Figure 3.2(b) confirms this position. Increasing resistivity removes the singularity and 'spreads out' the eigenfunction.
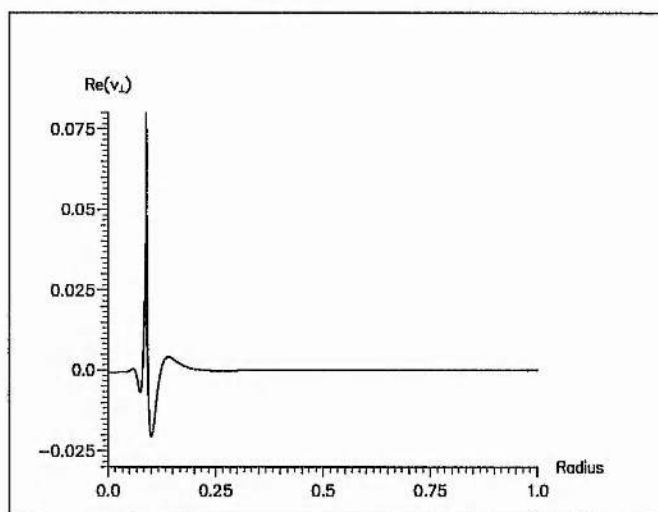
Figure 3.4: The thermal continuum singularity for $R_m = 1$ and calculated using 1,000 gridpoints. The growth rate is $s = 0.89996$. Notice that for this value of s, the position of the singularity is predicted by Figure 3.2(b).

For $R_m = 10^8$ (which is already well below the typical coronal value), the position of the original singularity is still clear and the growth rate has only been reduced by a relative amount of 10^{-5}. Thus the analysis of the thermal continuum for zero resistivity, which only involves the investigation of the cubic equation (3.40), gives important information about the results for non-zero resistivity. Increasing resistivity eventually removes the quasi-singular behaviour of the eigenfunction and smoothes out the singularity. This is clearly illustrated in Figure 3.5(f) for $R_m = 10^3$. However, while resistivity influences the shape of the eigenfunctions, it has very little effect on the eigenvalue. The growth rate smoothly asymptotes to the maximum continuum value as $R_m \to \infty$. The growth rate reduces from 0.99945 for zero resistivity to 0.99903 for $R_m = 10^3$ (which is already an unrealistically low value for the magnetic Reynolds number). For classical values of the resistivity the eigenfunctions still resemble to a high degree the singular behaviour as shown in Figure 3.5(a). Thus, many of the properties of the most unstable mode can be predicted by considering the thermal continuum described by Equation (3.40). However, the question of what happens to the higher harmonics has not yet been addressed.

Figure 3.6 shows the behaviour of the higher harmonics as resistivity is again increased. In this Figure the eigenfunction closest to the specified growth rate of 0.997 is located for various values of the magnetic Reynolds number and the eigenfunctions obtained. Figure 3.2(b) shows that, corresponding to this growth rate, the eigenfunctions for zero resistivity should be singular at $r \approx 0.18$ and $r \approx 0.38$. For large, but finite R_m, the eigenfunctions should retain a quasi-singular behaviour at these points. In addition, a simple WKB analysis suggests that the eigenfunctions will be essentially oscillatory between these singular radii and evanescent elsewhere. This is clearly seen in Figure 3.6(b).
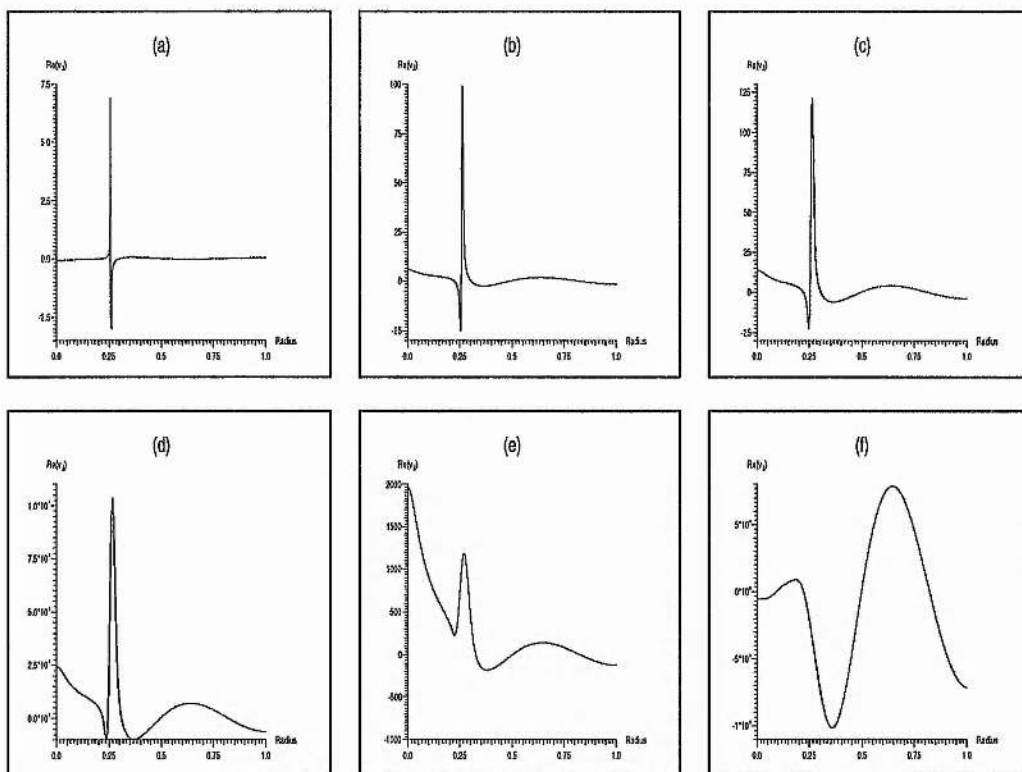
Figure 3.5: The most unstable quasi-continuum mode for various values of the magnetic Reynolds number for the cool Gold-Hoyle equilibrium profile, with wave numbers $k = m = 1$. Going from (a) to (f), the values of R_m are ∞, 10^8, 10^7, 10^6, 10^5 and 10^3. The corresponding growth rates are 0.99945, 0.99944, 0.99942, 0.99935, 0.99913 and 0.99903.

For $R_m = 10^6$, the two singular radii are located at the predicted positions and the eigenfunction is indeed highly oscillatory between these positions. As resistivity is increased the number of oscillations is reduced. This is a consequence of locating the eigenfunction nearest to a particular growth rate. One way to interpret these figures is to think of them showing how resistivity modifies the growth rates of the various normal mode harmonics. If a harmonic is identified by the number of zeros between the radii corresponding to the original singularities, then, as resistivity reduces the growth rate of each harmonic, Figure 3.6 gives the value of resistivity at which the growth rate of a particular harmonic is approximately equal to 0.997.

In summary, Figure 3.5 follows one particular normal mode as the value of resistivity is increased whereas Figure 3.6 represents different modes. To investigate how resistivity influences the spatial structure of normal modes it is important to follow the same normal mode. From Figure 3.5 it is clear that resistivity has smoothed out the singularity and the thickness of the internal boundary layer δ, as a function of resistivity, is shown in Figure 3.7. An indicator of the boundary-layer thickness used is the distance between the maximum and minimum near the original singular radius.
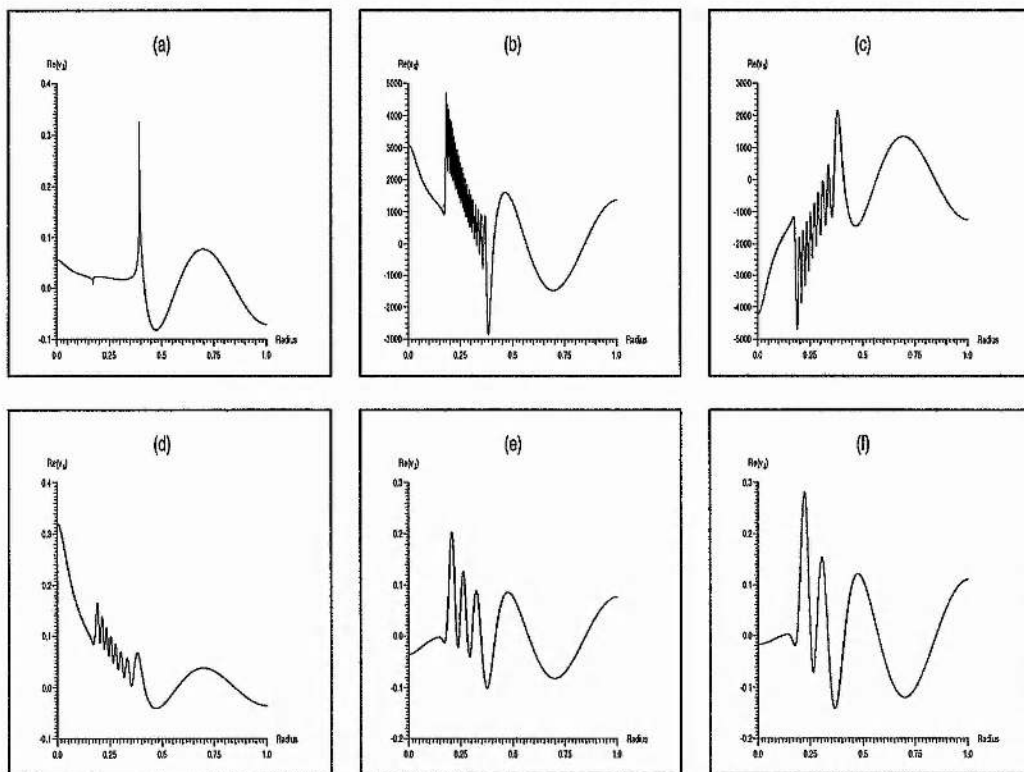
Figure 3.6: Individual quasi-continuum modes for various values of the magnetic Reynolds number. Going from (a) to (f), the values of R_m are ∞, 10^6, 2×10^5, 1.25×10^5, 2×10^4 and 10^4. The corresponding growth rates are 0.99681, 0.99705, 0.99703, 0.99687, 0.99675 and 0.99674. Notice that for a growth rate of $s = 0.997$, Figure 3.2(b) gives the location of the two singularities seen in graph (a).

It is apparent that the thickness scales with resistivity to the power $1/4$. This is not too surprising: this scaling of the thickness of the resistive layer is in agreement with the analysis presented in Sakurai, Goossens and Hollweg (1990). Their analysis also yields $\delta \sim R_m^{-1/4}$ close to an extremal value of the continuum. Based on this scaling, the thickness of the fine structure is comparable to the thickness predicted by the inclusion of perpendicular thermal conduction (Van der Linden and Goossens, 1991). These estimates are in agreement with the observed widths. If R_m lies between 10^8-10^{12}, then $R_m^{-1/4}$ will lie between 10^{-3}-10^{-2}.

Therefore the length scales for the prominence fine structure are 10^5-10^6m. This is comparable to length scales obtained with perpendicular thermal conduction obtained by Van der Linden and Goossens (1991).
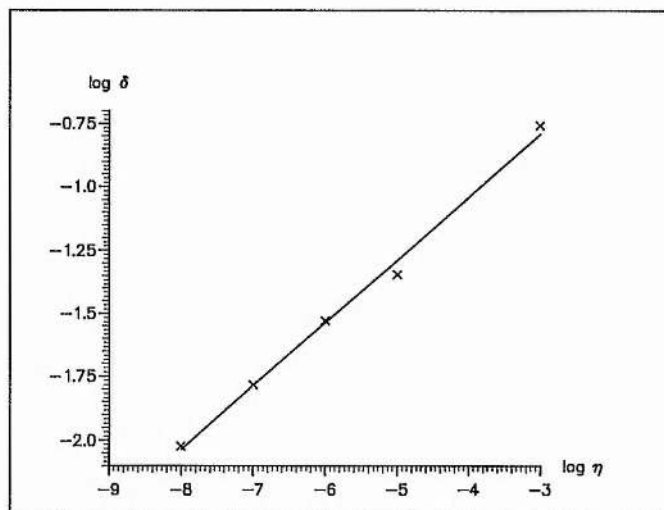
Figure 3.7: Plot of $\log \eta$ against $\log \delta$. The gradient of the line is evaluated and found to be $1/4$. Thus, the thickness of the resistive layer scales with resistivity to the power $1/4$.

3.7   Chapter Summary

This Chapter has investigated the effect of finite, scalar resistivity and perpendicular thermal conduction on the thermal instability. In the absence of these two dissipative terms there are three continuous spectra associated with the linearised MHD equations, namely the Alfvén, slow and thermal continua. These dissipative terms are now included and their effect on the continuous spectra is summarised.

Neglecting resistivity but including perpendicular thermal conduction, it is found that the thermal continuum is removed but the Alfvén and a modified slow continua remain. The removal of the thermal continuum is not surprising since temperature disturbances can be smoothed out across the magnetic flux surfaces and a global normal mode is possible. However, the eigenfunctions of this quasi-continuum vary rapidly over a length scale that is proportional to $(\kappa_\perp/\kappa_\parallel)^{1/4}$ (Van der Linden and Goossens, 1991).

Now consider the situation in which resistivity is included but perpendicular thermal conduction is neglected. In this case the Alfvén and slow mode continua are removed and the only continuous spectrum left is the thermal continuum. However, this continuum arises from the singularity associated with a sixth-order (in the perpendicular direction) differential equation rather than the singularity of the second-order equation in the absence of resistivity. The singularities are therefore quite different. Nevertheless, it appears that the two continua are similar when the Alfvén to radiative time scale ratio is small. In the other cases the thermal continuum is strongly influenced by resistivity in a discontinuous manner. This illustrates the singular nature of resistive MHD and shows that there is a difference between zero resistivity and 'small' resistivity. For the equilibrium investigated, the new thermal continuum lies below the zero resistivity continuum. In addition, the zero resistivity continuum is replaced by a quasi-continuum, which consists of a dense set of discrete and continuous (in the spatial direction) normal modes.

Finally, the inclusion of both resistivity and perpendicular thermal conduction removes all the continuous spectra. However, the thermal quasi-continuum will remain.

The main numerical work in this Chapter has concentrated on the effect of resistivity on the structure of the global normal modes. It is found that resistivity does not substantially reduce the growth rate associated with the maximum of the original thermal continuum, but does remove the singular nature of the eigenfunctions. Furthermore, since the quasi-continuum contains many normal modes with similar growth rates, the higher harmonics were also investigated. Considering the normal mode that is closest to a given growth rate, about 99% of the fundamental growth rate, the structure of the highly oscillatory eigenfunctions was investigated for different values of the magnetic Reynolds number. It was found that the length scales associated with the oscillatory nature of the eigenfunctions scaled with $\eta^{1/4}$, the same fractional power as perpendicular thermal conduction. Thus, fine scale structure can be generated by resistivity as well as perpendicular thermal conduction (see Van der Linden, 1993 for more details of the fine scale structure associated with perpendicular thermal conduction).

From the results obtained here and in Van der Linden and Goossens (1991), the importance of the thermal continuum can now be assessed. In the absence of the two dissipative effects considered, there is a thermal continuum that can be described by the solution of a simple cubic equation. The growth rate can be calculated as a function of the radial distance and this defines a range of possible growth rates. Thus, for a given radius there is an associated growth rate. At this stage, there exists a normal mode solution that has the above mentioned growth rate and possesses a singularity at the specified radius. If the thermal continuum curve has a local maximum, s_{max} at the radius, say, r_{max}, then the inclusion of resistivity removes the singularity and the most unstable quasi-continuum mode has a growth rate that is given by s_{max} and is strongly localised about r_{max}. Hence, the information about a physical, normal mode can be obtained by analysing the cubic equation that defines the thermal continuum. Now consider a growth rate that lies below the maximum of the continuum curve. There are now two different radii corresponding to this value of s. The inclusion of resistivity again removes the singularities and it is observed that the eigenfunctions are highly oscillatory between these two radii. Therefore, analysing the thermal continuum curve can also predict the radii between which fine scale structure can form.

It is clear that resistivity can produce fine scale structure as the plasma cools. This is similar to the effect of perpendicular thermal conduction and in both cases the length scales of the fine structure scale with the diffusion coefficient to the power one quarter. Hence, classical values of these two diffusion coefficients will give rise to the typical length scales observed within quiescent prominences.

Chapter 4

Magnetothermal Instabilities in Coronal Arcades

*...mechanically quiet and smooth...all the major controls are light and
precise and the gear change is perhaps the best we have ever tried.... It should
on its present merits rise right to the first rank amongst small cars of
the world.*
    -Review of the Imp in Motor Magazine.

*We put it into production and they started failing all over the place...
The prototype worked, the pre-production worked and the production didn't.*
    -Jim Pollard, Quality Manager.

4.1   Overview

In this Chapter, the normal mode spectrum for the linearised MHD equations is investigated for a plasma
in a cylindrical equilibrium. The equations describing these normal modes are solved numerically using
a finite element code. In the ideal case, the Hain-Lüst equation is expanded and a WKB solution
obtained. This is compared to the numerical solutions. In the non-ideal case, the ballooning equations
that describe localised modes are manipulated and a dispersion relation derived. It is shown that as
the axial wave number k is increased, the fundamental thermal and Alfvén modes can coalesce to form
overstable magnetothermal modes. The ratio between the magnetic and thermal terms is varied and
the existence of the magnetothermal modes examined. The corresponding growth rates are predicted
by a WKB solution to the ballooning equations. The existence of these magnetothermal modes may be
significant in the eruption of prominences into solar flares.

4.2   Introduction

As remarked in Chapter 1, there are many interesting features present both on and around the Sun.
High above the photosphere in the solar corona, prominences are often observed. These are cooler and
denser than the surrounding corona and, although not accurately known, have a mass of about one tenth
of the total corona. One of the most intriguing questions is concerned with how these prominences form.

Many suggestions have been made, one mechanism being due to a condensation driven by the plasma's optically thin radiation. Once this thermal instability is triggered, the plasma continues to cool until it becomes optically thick, typically at a temperature of about 7,000K, the temperature usually observed within the prominence (see Chapter 2 for details).

While the above scenario is happening, the equilibrium magnetic field must be stable or the prominence cannot form. This is a consequence of the radiation time scale being very much greater than the magnetic field time scale. It is interesting to note that, if the corona is treated as an isolated plasma totally unconnected to the photosphere, magnetic stability is very difficult to achieve. The question then arises as to why there are so many prominences observed when this stability condition apparently rules them out. The answer is that the corona is not an isolated plasma, but is connected by magnetic field lines that emerge from the photosphere. This connection thus stabilises the magnetic field in the corona and hence enables the prominences to form. This condition, known as line-tying, is not considered here, but will be addressed in Chapter 5.

Once formed, the prominence remains supported in the corona in a stable configuration for many days, or even months, until it erupts. The destruction of the prominence is thought to occur because the equilibrium magnetic field has become unstable to an ideal MHD instability. Often this magnetic instability will trigger off a flare which is observed as a rapid brightening in Hα. Solar flares give off an immense amount of energy, in the region of 10^{25}J. The source of this energy is the stressed coronal magnetic field that becomes unstable and releases the stored magnetic energy.

From the above discussion about possible prominence and flare formation, it is apparent that there are two distinct mechanisms at work; a thermal instability and a magnetic instability. However, there is no reason why these instabilities cannot be coupled together, instead of only occurring individually. In this Chapter, the two basic instabilities are studied and their interactions considered and examined for a simple cylindrical equilibrium. Before progressing to a more realistic situation, the basic physical properties of these magnetothermal modes must be fully understood. The first rigorous treatment of the thermal instability mechanism was by Field (1965). He considered an infinite, uniform plasma and derived various conditions for triggering a thermal instability (details are given in Chapter 2). This work has been extended by many authors (see, for example, Heyvaerts, 1974; Van der Linden and Goossens, 1991). In particular, Van der Linden and Goossens (1991) showed that the instability criteria derived by Parker (1953) and Field (1965) for a uniform, infinite plasma can be generalised into sufficient conditions for the onset of thermal instability in a non-uniform plasma (see Chapter 3).

Defining wave numbers parallel ($k_\parallel$) and perpendicular ($k_\perp$) to the equilibrium magnetic field and writing the anisotropic thermal conduction in terms of the coefficients of heat conduction parallel ($\kappa_\parallel$) and perpendicular ($\kappa_\perp$) to the magnetic field, it can be shown (Field, 1965 and Chapter 2) that the thermal instability criteria are given by

$$\left(\frac{\partial \mathcal{L}}{\partial T}\right)_\rho \; < \; 0 \qquad (\text{for } k_\parallel = k_\perp = 0), \tag{4.1}$$

$$\kappa_\parallel k_\parallel^2 + \kappa_\perp k_\perp^2 + \rho_0 \left(\frac{\partial \mathcal{L}}{\partial T}\right)_\rho - \frac{\rho_0^2}{T_0}\left(\frac{\partial \mathcal{L}}{\partial \rho}\right)_T \; < \; 0 \qquad (\text{for } k_\parallel \neq 0), \tag{4.2}$$

and

$$\kappa_\perp k_\perp^2 + \rho_0 \left(\frac{\partial \mathcal{L}}{\partial T}\right)_\rho - \frac{c_i^2 \rho_0^2}{T_0 \left(c_i^2 + v_A^2\right)}\left(\frac{\partial \mathcal{L}}{\partial \rho}\right)_T \; < \; 0 \qquad (\text{for } k_\parallel = 0,\ k_\perp \neq 0), \tag{4.3}$$

where c_i is the isothermal sound speed, defined by $c_i^2 = p_0/\rho_0$, $v_A = B_0/\sqrt{\mu\rho_0}$ is the Alfvén speed, $\mathcal{L}$ is the generalised energy loss function per unit mass with energy gains defined as negative losses

and $(\partial\mathcal{L}/\partial T)_\rho$ is the partial derivative of $\mathcal{L}$ with respect to T keeping ρ fixed. In the energy loss function an optically thin radiative loss term and an unspecified coronal heating function h are included

$$\rho\mathcal{L} \;=\; \widetilde{\chi}\rho^2 T^\alpha - \rho h, \tag{4.4}$$

where $\widetilde{\chi}$ and α are piecewise constant functions of T (Rosner, Tucker and Vaiana, 1978).

It is easy to appreciate the importance of the magnetic field on the thermal instability due to these two conditions for 'isobaric' thermal instability for $\mathbf{k}\cdot\mathbf{B}_0 = 0$ and $\mathbf{k}\cdot\mathbf{B}_0 \neq 0$, given by Equations (4.2) and (4.3) first obtained by Field (1965). From this, it can be seen that it is quite possible for the magnetic field to influence the thermal instability.

In what follows, the normal mode spectrum for the linearised MHD equations is investigated for a cylindrical equilibrium with attention restricted to the unstable subspectrum. The normal mode spectrum usually consists of both discrete and continuous subspectra. There are normally three types of continuous spectra corresponding to the anisotropic nature of the Alfvén, slow and thermal modes. However, the nature of the spectrum depends upon which dissipative effects are included and upon the equilibrium considered. For example, when resistivity is included, the Alfvén and slow mode continua are removed and only the thermal continuum remains. When perpendicular thermal conduction alone is included, the continuous spectra are found to consist of the Alfvén continuum and the modified 'isothermal' slow continuum. More details about continuous spectra can be found in Goedbloed (1983), Van der Linden and Goossens (1991), Ireland *et al.* (1992) and Chapter 3.

In previous work by Van der Linden *et al.* (1992), a first study of the coalescence of magnetic and thermal modes was presented. In particular, the effect on the Alfvén, thermal and coalesced magnetothermal modes were studied when the axial wave number k was varied while the azimuthal wave number m was set equal to zero. As the axial wave number was varied, the fundamental thermal and magnetic modes were found to coalesce (or join together) and form a complex conjugate pair of overstable wave modes. These overstable wave modes or magnetothermal instabilities were first found via the use of the ballooning method applied to the normal mode spectrum and showed that thermal instabilities and magnetic instabilities do indeed interact with one another and should be studied together and not individually. This interaction depends upon the ratio of the ideal growth time to the radiative time scale. Normally the ratio is small for the corona except when the equilibrium is near ideal marginal stability.

The aim of this Chapter is to investigate the basic properties of these magnetothermal modes for a non-zero azimuthal wave number and in the absence of photospheric boundary conditions. In Section 4.3 the basic equations are introduced and the equations for normal modes are obtained. These are solved numerically using a finite element code. Section 4.4 describes the behaviour of the fundamental Alfvén mode in the ideal case for large values of the axial wave number k with the azimuthal wave number $m = 1$. Section 4.5 examines the fundamental Alfvén, thermal and magnetothermal modes as k is varied in the non-ideal case. The ballooning equations are manipulated and a WKB solution is compared with the numerical results. The final Section then summarises the results found in this Chapter.

4.3   The Basic MHD Equations

The basic equations used in this Chapter are the standard equations of magnetohydrodynamics in which gravity, resistivity, viscosity and rotational effects are neglected,

$$\frac{\partial\rho}{\partial t} + \rho\nabla\cdot\mathbf{v} + \mathbf{v}\cdot\nabla\rho \;=\; 0, \tag{4.5}$$

$$\rho \left[\frac{\partial \mathbf{v}}{\partial t} + (\mathbf{v} \cdot \nabla) \mathbf{v} \right] \;=\; -\nabla p + \frac{1}{\mu} (\nabla \times \mathbf{B}) \times \mathbf{B}, \tag{4.6}$$

$$\frac{\partial \mathbf{B}}{\partial t} \;=\; \nabla \times (\mathbf{v} \times \mathbf{B}), \tag{4.7}$$

$$p \;=\; \frac{\mathcal{R}}{\tilde{\mu}} \rho T, \tag{4.8}$$

$$\frac{\rho^\gamma}{\gamma - 1} \left[\frac{\partial}{\partial t} \left(\frac{p}{\rho^\gamma} \right) + (\mathbf{v} \cdot \nabla) \left(\frac{p}{\rho^\gamma} \right) \right] \;=\; \nabla \cdot (\kappa \nabla T) - \rho \mathcal{L}(\rho, T), \tag{4.9}$$

where all the symbols are defined in Chapter 2. In this Chapter, perpendicular thermal conduction is neglected as it is of no relevance for the mode coalescence. Hence, the anisotropic thermal conduction term is rewritten only in terms of the coefficient of heat conduction parallel ($\kappa_\parallel$) to the magnetic field

$$\nabla \cdot (\kappa \nabla T) \;=\; \mathbf{B} \cdot \nabla \left(\kappa_\parallel \frac{\mathbf{B} \cdot \nabla T}{B^2} \right). \tag{4.10}$$

The magnetic field must also satisfy the condition

$$\nabla \cdot \mathbf{B} \;=\; 0. \tag{4.11}$$

4.3.1   The Equilibrium Equations

The equilibrium configuration is a static, one-dimensional, infinite, cylindrical plasma, having a magnetic field with axial and azimuthal components depending on the radial co-ordinate r such that Equation (4.11) is identically satisfied. Hence,

$$\mathbf{B}_0 \;=\; \big(0, B_{\theta 0}(r), B_{z0}(r)\big). \tag{4.12}$$

The aim of this work is to study coalescence of the thermal and magnetic modes. The Gold-Hoyle profile (Gold and Hoyle, 1960) is used because it is a simple equilibrium and the ideal MHD properties are well known. The specific form of the equilibrium equations used in this Chapter represent a dimensionless, isothermal, constant shear magnetic field

$$B_{\theta 0} \;=\; \frac{r}{(1 + r^2)}, \qquad B_{z0} \;=\; \frac{\lambda}{(1 + r^2)},$$

$$\beta p_0 \;=\; \frac{1 - \lambda^2}{2(1 + r^2)^2}, \tag{4.13}$$

where the plasma beta β has been defined as $\beta = \mu p_c / B_c^2$ with p_c and B_c representing the values of the plasma's pressure and magnetic field strength at the centre of the cylinder axis respectively, while r is a dimensionless co-ordinate ranging from 0 to 1, scaled to the radius of the outer plasma boundary. In these equilibrium equations λ is a variable parameter. When $\lambda = 0$, the equilibrium magnetic field is shearless and when $\lambda = 1$ a pressureless, force free field is obtained. In this equilibrium, the values of density and magnetic field strength at the centre of the cylinder axis are taken to be $\rho_c = 3.6886 \times 10^{-11}$kg m^{-3} and $B_c = 10$G, respectively. The thermal equilibrium is given by $\mathcal{L} = 0$. In this equilibrium, the coronal heating is considered to be constant per unit mass.

4.3.2 Linear Perturbations

The normal mode solutions that are to be solved numerically are obtained by linearising Equations (4.5)-(4.9), introducing a magnetic vector potential so that Equation (4.11) is automatically satisfied and letting all the perturbed quantities behave like

$$\rho_1 = \rho'(r) \exp\left[i\left(m\theta + kz\right)\right] e^{st}. \tag{4.14}$$

Introducing velocity components v'_r perpendicular to the flux surface and $v'_\perp$ and $v'_\parallel$ in the flux surface but perpendicular and parallel to the equilibrium magnetic field respectively and dropping the '0' subscripts for ease of writing it is found that the linearised equations become

$$s\rho' = -\frac{1}{r}\frac{d}{dr}\left(r\rho v'_r\right) - \frac{i\rho f}{B}v'_\parallel - \frac{i\rho g}{B}v'_\perp, \tag{4.15}$$

$$s\rho v'_r = -\frac{d}{dr}\left[\frac{p}{T}T' + \frac{p}{\rho}\rho' - \frac{ig}{\mu}A'_r - \frac{B_\theta}{\mu}\frac{dA'_z}{dr} + \frac{B_z}{\mu r}\frac{d}{dr}\left(rA'_\theta\right)\right]$$
$$- \frac{2ikB_\theta}{\mu r}A'_r + \frac{kf}{\mu}A'_\theta + \frac{2B_\theta}{\mu r}\frac{dA'_z}{dr} - \frac{mf}{\mu r}A'_z, \tag{4.16}$$

$$s\rho r B i v'_\perp = \frac{pgr}{T}T' + \frac{pgr}{\rho}\rho' + \frac{mB^2}{\mu r}\frac{d}{dr}\left(rA'_\theta\right) + \frac{kB^2 r}{\mu}\frac{dA'_z}{dr} - \frac{B^2 r}{\mu}\left(\frac{m^2}{r^2} + k^2\right)iA'_r$$
$$+ \frac{1}{\mu}\left(\frac{B_\theta B_z}{r} + B_z\frac{dB_\theta}{dr} - B_\theta\frac{dB_z}{dr}\right)\left(krA'_\theta - mA'_z\right), \tag{4.17}$$

$$s\rho B i r v'_\parallel = \frac{frp}{T}T' + \frac{frp}{\rho}\rho' - kr\frac{dp}{dr}A'_\theta + m\frac{dp}{dr}A'_z, \tag{4.18}$$

$$sA'_r = Bv'_\perp, \tag{4.19}$$

$$sA'_\theta = -B_z v'_r, \tag{4.20}$$

$$sA'_z = B_\theta v'_r, \tag{4.21}$$

$$s\rho C_v T' = -\rho C_v\frac{dT}{dr}v'_r - \frac{p}{r}\frac{d}{dr}\left(rv'_r\right) - \frac{ipf}{B}v'_\parallel - \frac{ipg}{B}v'_\perp - \frac{f^2\kappa_\parallel}{B^2}T'$$
$$- \left(\mathcal{L} + \rho\left(\frac{\partial\mathcal{L}}{\partial\rho}\right)_T\right)\rho' - \rho\left(\frac{\partial\mathcal{L}}{\partial T}\right)_\rho T' + \frac{f\kappa_\parallel}{rB^2}\frac{dT}{dr}\left(rkA'_\theta - mA'_z\right), \tag{4.22}$$

$$p' = \frac{p}{T}T' + \frac{p}{\rho}\rho', \tag{4.23}$$

where $\mathbf{A}' = (A'_r, A'_\theta, A'_z)$ is the perturbed magnetic vector potential and

$$f = \frac{mB_\theta}{r} + kB_z, \qquad g = \frac{mB_z}{r} - kB_\theta, \qquad C_v = \frac{\mathcal{R}}{\tilde{\mu}\left(\gamma - 1\right)}. \tag{4.24}$$

4.4   Results for the Ideal Case

In any study of the normal mode spectrum for a given equilibrium, it is essential to get a good idea of what is happening globally, before restricting attention to specific regions, see Van der Linden and Goossens (1991). It is therefore very important to discover the nature of the spectrum and the associated bands of continuous spectra before proceeding with any local analysis. After neglecting the non-ideal terms in Equations (4.15)-(4.23) and performing some algebra, the Hain-Lüst equation is obtained (see Goedbloed (1983) and Chapter 3):

$$\frac{d}{dr}\left[\frac{rN}{r^2 D}\frac{d\chi}{dr}\right] \;+\; \left[-\frac{1}{r}\left(s^2\rho + f^2\right) - \frac{d}{dr}\left(\frac{B_\theta^2}{r^2}\right)\right.$$
$$\left.+\; \frac{4k^2 B_\theta^2}{r^3 D}\left(B^2 s^2\rho + \gamma p f^2\right) - \frac{d}{dr}\left(\frac{2k B_\theta g}{r^2 D}\left(s^2\rho\left(\gamma p + B^2\right) + \gamma p f^2\right)\right)\right]\chi \;=\; 0, \quad (4.25)$$

where

$$N \;=\; \left(s^2\rho + f^2\right)\left(s^2\rho\left(\gamma p + B^2\right) + \gamma p f^2\right), \tag{4.26}$$

and

$$D \;=\; s^4\rho^2 + \left(k^2 + \frac{m^2}{r^2}\right)\left(s^2\rho\left(\gamma p + B^2\right) + \gamma p f^2\right), \tag{4.27}$$

where $\chi \equiv rv'_r$. As in Chapter 3, it can be seen that the continuous spectra present are given by the singularities in Equation (4.25). These singularities correspond to the positions where $N = 0$ and consist of the Alfvén continuum and the slow mode continuum. It is important to note that the zeros of D are only apparent singularities and do not correspond to continuous spectra. Notice that there is no continuous spectrum along the real s axis in ideal MHD. Considering the equilibrium given by Equations (4.13) with $\lambda = 0$ and $\beta = 1$, it can be seen that the Alfvén continuum collapses to a single point. Numerically, the fundamental Alfvén mode is found on the real positive axis (unstable) for an azimuthal wave number $m = 1$ and a fixed value of the axial wave number k. For $m = 1$, the value of k is varied and as k tends to infinity, the instability growth rate asymptotes to a fixed value. The eigenfunctions become increasingly more localised near $r = 0$ in the sense that the fundamental Alfvén mode becomes peaked about a particular radius as k increases.

The eigenfunctions were calculated using the finite element code LEDA (see Appendix C). The equations for normal modes given by Equations (4.15)-(4.23), with the non-ideal terms neglected, form an eigenvalue problem which is solved using up to 4,000 gridpoints (yielding very high spatial resolution). The eigenvalues obtained are expressed in the asymptotic form for large k as

$$s \;=\; s_0 + \frac{s_1}{k} + \frac{s_2}{k^2} + \dots. \tag{4.28}$$

Hence, for any three different values of k (and corresponding growth rates), three equations in s_0, s_1 and s_2 can be found and thus solved. For the values of k given by 1,000, 2,000 and 3,000, $s_0 = 1.414213565$ and $s_1 = -1.673325$.

Analytically, the Hain-Lüst equation (4.25) may be expanded for a small radius r and large axial wave number k, since the numerical solutions indicate localisation near $r = 0$. By matching up the two solutions for small r but large kr, it is found that $s_0 = \sqrt{2} = 1.414213562$ and $s_1 = -\sqrt{14/5} = -1.673320053$ (see Appendix D for details). Comparing the analytical results with the numerical results, very good agreement is found for large k. This gives confidence that both the numerical and analytical methods are accurate.

4.5 Ballooning Modes in the Non-Ideal Case

In this Section, a similar study to that previously carried out in Section 4.4 is performed with non-ideal effects included. The ballooning equations are manipulated to obtain a dispersion relation which is solved numerically. The ballooning approximation that describes localised modes is then compared to the exact solutions to Equations (4.15)-(4.23) generated by LEDA. The ballooning approximation was first introduced by Connor, Hastie and Taylor (1979) to investigate ideal instabilities in a toroidal plasma. Later Dewar and Glasser (1983) gave a detailed mathematical treatment for an ideal plasma in a general toroidal system. Hood (1986a,b) studied ballooning modes in the ideal case, for a coronal plasma. These applications were limited to linear, ideal MHD. The method has also been used with non-ideal effects included. For example, Velli and Hood (1986, 1987) studied resistive instabilities in a solar coronal loop while Van der Linden, Goossens and Hood (1988) studied the combined effects of resistivity and viscosity. To derive the ballooning equations, the perturbed quantities are assumed to have the form

$$f(\mathbf{r}) = \tilde{f}(r,\theta) \exp\left[iS(\mathbf{r})/\delta + st\right], \tag{4.29}$$

where $\mathbf{B} \cdot \nabla S = 0$ and $\delta \ll 1$. This form of the perturbation represents a rapid variation across the magnetic field lines (given by the exponential part) and a slow variation along the field lines given by the amplitude factor, present in front of the exponential. The constraint $\mathbf{B} \cdot \nabla S = 0$ for a coronal arcade is satisfied by setting

$$S = F(r) + z - q(r)\theta, \tag{4.30}$$

with

$$q(r) = \frac{rB_z}{B_\theta}, \tag{4.31}$$

where in principle $F(r)$ will be determined from the solutions to the eigenvalue problem and where $q(r)$ is known as the safety factor in magnetic fusion research. When the ballooning approximation given by Equation (4.29) is substituted into the linearised MHD equations, to lowest order in δ the following (ballooning) equations are obtained

$$\mathbf{B} \cdot \nabla \phi = -\frac{sB^2}{|\nabla S|^2} A_\|, \tag{4.32}$$

$$\mathbf{B} \cdot \nabla A_\| = -\frac{\mu \rho s |\nabla S|^2}{B^2} \phi + \frac{2\mu B_\theta}{rB^2} p_1, \tag{4.33}$$

$$\mathbf{B} \cdot \nabla u = -\frac{(\mu p + B^2)}{\mu p B^2}\left(s\mu p_1 + \frac{\mu}{B_\theta}\frac{dp}{dr}\phi\right) + \frac{s}{T}T_1 - \frac{2B_\theta}{rB^2}\phi, \tag{4.34}$$

$$\mathbf{B} \cdot \nabla p_1 \;=\; -s\rho B^2 u + \frac{B^2}{|\nabla S|^2 \, B_\theta} \frac{dp}{dr} A_{\|}, \tag{4.35}$$

$$\left[\kappa_{\|}\frac{(\mathbf{B} \cdot \nabla)^2}{B^2} - \left(\frac{\partial \widehat{\mathcal{L}}}{\partial T}\right)_p - \frac{\gamma}{(\gamma-1)}\frac{sp}{T}\right]T_1 \;=\; -\left[s - \left(\frac{\partial \widehat{\mathcal{L}}}{\partial p}\right)_T\right]p_1 - \frac{1}{B_\theta}\frac{dp}{dr}\phi, \tag{4.36}$$

where ϕ is the electrostatic potential, $A_{\|}$ is the parallel component of the vector potential, u is the parallel component of the perturbed velocity and $\widehat{\mathcal{L}}$ has been defined to be $\widehat{\mathcal{L}} = \rho\mathcal{L}$. The electrostatic potential ϕ is related, to leading order, to the perpendicular component of the perturbed velocity $\mathbf{v}'_{\perp}$ in the $\mathbf{B}_0 \times \nabla S$ direction by

$$\mathbf{v}'_{\perp} \approx \frac{i}{\delta}\left(\mathbf{B}_0 \times \nabla S\right)\phi. \tag{4.37}$$

These ballooning equations, derived first by Hood, Van der Linden and Goossens (1989), represent the Alfvén, slow and thermal modes. The fast modes have been eliminated by setting

$$\mu p_1 + \mathbf{B} \cdot \mathbf{B}_1 \;=\; 0, \tag{4.38}$$

and have therefore been excluded in the derivation of the ballooning equations, see Hood, Van der Linden and Goossens (1989). These ballooning equations can easily be obtained from Hood *et al.* (1989), by replacing their variables by $\phi/\epsilon \to \phi$, $-ip_1 \to p_1$, $-iv_{\|} \to uB$, $a_{\|}/\epsilon \to A_{\|}B/\,|\nabla S|^2$ and $-iT_1 \to T_1$. Introducing the time scales in Table 4.1 and setting $\mathbf{B} \to B_0\mathbf{B}$, $\mathbf{B}_1 \to B_0\mathbf{B}_1$, $p \to p_0p$, $p_1 \to p_0p_1$, $T \to T_0T$, $T_1 \to T_0T_1$, $\rho \to \rho_0\rho$, $\nabla \to \nabla/l$, $r \to lr$, $s \to s/\tau_A$, $A_{\|} \to A_{\|}$, $\phi \to B_0 l\phi/\tau_A$ and $u \to lu/\tau_A B_0$, it is found that the dimensionless equations, for the isothermal equilibrium $T=1$, are

$$\mathbf{B} \cdot \nabla\phi \;=\; -\frac{sB^2}{|\nabla S|^2}A_{\|}, \tag{4.39}$$

$$\mathbf{B} \cdot \nabla A_{\|} \;=\; -\frac{\rho s\,|\nabla S|^2}{B^2}\phi + \frac{2B_\theta\beta}{rB^2}p_1, \tag{4.40}$$

$$\mathbf{B} \cdot \nabla u \;=\; -\frac{(\beta p + B^2)}{\beta pB^2}\left(s\beta p_1 + \frac{\beta}{B_\theta}\frac{dp}{dr}\phi\right) + sT_1 - \frac{2B_\theta}{rB^2}\phi, \tag{4.41}$$

$$\mathbf{B} \cdot \nabla p_1 \;=\; -\frac{s\rho B^2}{\beta}u + \frac{B^2}{|\nabla S|^2 \, B_\theta}\frac{dp}{dr}A_{\|}, \tag{4.42}$$

$$\left[\widehat{R}\frac{(\mathbf{B} \cdot \nabla)^2}{B^2} - \left(\frac{\partial \widehat{\mathcal{L}}}{\partial T}\right)_p - \frac{\gamma}{(\gamma-1)}\epsilon sp\right]T_1 \;=\; -\left[\epsilon s - \left(\frac{\partial \widehat{\mathcal{L}}}{\partial p}\right)_T\right]p_1 - \frac{\epsilon}{B_\theta}\frac{dp}{dr}\phi, \tag{4.43}$$

where

$$\epsilon = \tau_{rad}/\tau_A, \quad \widehat{R} = \tau_{rad}/\tau_{cond} \quad \text{and} \quad \beta = \tau_A^2/\tau_s^2. \tag{4.44}$$

Equation (4.44) defines some parameters in terms of time scales. Typical values of these time scales for the solar corona and prominences are given in Table 4.1.

Time scales	Symbol	Definition	Coronal Value	Prom. Value
Alfvén	τ_A	$l(\mu\rho)^{1/2}/B$	5	100
Sound (isothermal)	τ_s	$l/(T\mathcal{R}/\widetilde{\mu})^{1/2}$	200	300
Radiation	τ_{rad}	$1/p\chi T^{\alpha-2}$	3,000	1
Conduction	τ_{cond}	$pl^2/\kappa_{\|}T$	600	10^7
Free-fall	τ_g	v/g	40	40

Table 4.1: Typical time scales, in seconds, for the physical processes that occur in the solar corona and prominences. The values taken in this Chapter, to model a coronal arcade, are $B = 10$G, $\rho = 3.7 \times 10^{-11}$kg m^{-3} and $T = 2.6 \times 10^6$K.

Since the amplitude function $\widetilde{f}$ does not depend on z, $\mathbf{B} \cdot \nabla \rightarrow imB_\theta/r$ and the ballooning equations become

$$\frac{imB_\theta}{r}\phi = -\frac{sB^2}{|\nabla S|^2}A_{\|}, \tag{4.45}$$

$$\frac{imB_\theta}{r}A_{\|} = -\frac{\rho s|\nabla S|^2}{B^2}\phi + \frac{2B_\theta\beta}{rB^2}p_1, \tag{4.46}$$

$$\frac{imB_\theta}{r}u = -\frac{(\beta p + B^2)}{\beta pB^2}\left(s\beta p_1 + \frac{\beta}{B_\theta}\frac{dp}{dr}\phi\right) + sT_1 - \frac{2B_\theta}{rB^2}\phi, \tag{4.47}$$

$$\frac{imB_\theta}{r}p_1 = -\frac{s\rho B^2}{\beta}u + \frac{B^2}{|\nabla S|^2}\frac{dp}{B_\theta}\frac{dp}{dr}A_{\|}, \tag{4.48}$$

$$\left[-\frac{\widehat{R}m^2B_\theta^2}{r^2B^2} - \left(\frac{\partial\widehat{\mathcal{L}}}{\partial T}\right)_p - \frac{\gamma}{(\gamma-1)}\epsilon sp\right]T_1 = -\left[\epsilon s - \left(\frac{\partial\widehat{\mathcal{L}}}{\partial p}\right)_T\right]p_1 - \frac{\epsilon}{B_\theta}\frac{dp}{dr}\phi. \tag{4.49}$$

It is important to appreciate how to obtain global normal modes from the ballooning (or localised) modes. Dewar and Glasser (1983) showed that the most unstable mode in ideal MHD could be found by setting $dF/dr = 0$ and solving the ballooning equations on each flux surface. The growth rate of the most unstable, physical mode then corresponds to the maximum of the ballooning growth rate as a function of r, the radial flux surface co-ordinate. Unfortunately, there is no proof that this method holds for non-ideal MHD. Thus, following Van der Linden *et al.* (1992), the ballooning equations are solved simultaneously on each flux surface and the maximum ballooning growth rate compared with the actual normal mode solutions obtained by LEDA.

4.5.1   Dispersion Relation

The variables in Equations (4.45)-(4.49) are ϕ, $A_\parallel$, p_1, u and T_1. For non-trivial solution, the determinant of the coefficients of these variables must vanish giving

$$\frac{s^2 \rho B^2}{\beta} \left[\frac{\epsilon}{B_\theta} \frac{dp}{dr} + \frac{r}{2\beta B_\theta} \left(\epsilon s - \left(\frac{\partial \widehat{\mathcal{L}}}{\partial p} \right)_T \right) \left(\frac{m^2 B_\theta^2}{sr^2} + s\rho \right) |\nabla S|^2 \right]$$

$$+ \left[\frac{\widehat{R} m^2 B_\theta^2}{r^2 B^2} + \left(\frac{\partial \widehat{\mathcal{L}}}{\partial T} \right)_p + \frac{\gamma \epsilon s p}{(\gamma - 1)} \right] \left[\frac{-m^2 B_\theta}{r} \left\{ \frac{1}{2\beta} \left(\frac{m^2 B_\theta^2}{sr^2} + s\rho \right) |\nabla S|^2 + \frac{1}{rs} \frac{dp}{dr} \right\} \right.$$

$$\left. - \frac{\rho s}{\beta} \left\{ \frac{(\beta p + B^2)}{p} \left(\frac{1}{B_\theta} \frac{dp}{dr} + \frac{rs}{2B_\theta \beta} \left(\frac{m^2 B_\theta^2}{sr^2} + s\rho \right) |\nabla S|^2 \right) + \frac{2B_\theta}{r} \right\} \right] = 0. \qquad (4.50)$$

Rearranging Equation (4.50) gives

$$- \frac{\epsilon \rho^2 (\gamma \beta p + B^2) |\nabla S|^2}{B_\theta^2 (\gamma - 1)} s^5 + \rho^2 |\nabla S|^2 \left[-\frac{B^2}{B_\theta^2} \left(\frac{\partial \widehat{\mathcal{L}}}{\partial p} \right)_T + \frac{(\beta p + B^2) \gamma}{(\gamma - 1) B_\theta^2} \sigma_R \right] s^4$$

$$- \frac{\epsilon \rho}{r^2 (\gamma - 1)} \left[\gamma \beta p \left(m^2 |\nabla S|^2 + 4 \right) + \frac{(\gamma \beta p + B^2)}{B_\theta^2} \left(m^2 B_\theta^2 |\nabla S|^2 + 2r\beta \frac{dp}{dr} \right) \right] s^3$$

$$+ \frac{\rho}{r^2} \left[\frac{\gamma \beta p}{(\gamma - 1)} \sigma_R \left(m^2 |\nabla S|^2 + 4 + \frac{(\beta p + B^2)}{\beta p B_\theta^2} \left(m^2 B_\theta^2 |\nabla S|^2 + 2r\beta \frac{dp}{dr} \right) \right) - m^2 B^2 \left(\frac{\partial \widehat{\mathcal{L}}}{\partial p} \right)_T |\nabla S|^2 \right] s^2$$

$$- \frac{m^2 \gamma \beta p}{(\gamma - 1) r^4} \left(m^2 B_\theta^2 |\nabla S|^2 + 2r\beta \frac{dp}{dr} \right) (\epsilon s - \sigma_R) = 0, \qquad (4.51)$$

where σ_R is the isobaric growth rate given by

$$\sigma_R = -\frac{(\gamma - 1)}{\gamma p} \left[\left(\frac{\partial \widehat{\mathcal{L}}}{\partial T} \right)_p + \frac{m^2 \widehat{R} B_\theta^2}{r^2 B^2} \right]. \qquad (4.52)$$

4.5.2   Ballooning modes for $\lambda = 0$

In this Section, parallel thermal conduction is set equal to zero for simplicity and because its inclusion will only reduce the growth rates slightly. Consider first the case in which there is no z component of the equilibrium magnetic field. For this shearless equilibrium magnetic field, $\lambda = 0$ in Equations (4.13). Setting $\lambda = 0$ and $dF/dr = 0$ gives $|\nabla S|^2 = 1$. Equation (4.51) then becomes

$$- \frac{\epsilon \rho^2 (\gamma \beta p + B^2)}{B^2 (\gamma - 1)} s^5 + \rho^2 \left[-\left(\frac{\partial \widehat{\mathcal{L}}}{\partial p} \right)_T + \frac{(\beta p + B^2) \gamma}{(\gamma - 1) B^2} \sigma_R \right] s^4$$

$$- \frac{\epsilon \rho}{r^2 (\gamma - 1)} \left[\gamma \beta p \left(m^2 + 4 \right) + \frac{(\gamma \beta p + B^2)}{B^2} \left(m^2 B^2 + 2r\beta \frac{dp}{dr} \right) \right] s^3$$

$$+ \frac{\rho}{r^2} \left[\frac{\gamma \beta p}{(\gamma - 1)} \sigma_R \left(m^2 + 4 + \frac{(\beta p + B^2)}{\beta p B^2} \left(m^2 B^2 + 2r\beta \frac{dp}{dr} \right) \right) - m^2 B^2 \left(\frac{\partial \widehat{\mathcal{L}}}{\partial p} \right)_T \right] s^2$$

$$- \frac{m^2 \gamma \beta p}{(\gamma - 1) r^4} \left(m^2 B^2 + 2r\beta \frac{dp}{dr} \right) (\epsilon s - \sigma_R) = 0, \qquad (4.53)$$

where the isobaric growth rate σ_R is now given by

$$\sigma_R = -\frac{(\gamma - 1)}{\gamma p} \left(\frac{\partial \widehat{\mathcal{L}}}{\partial T} \right)_p. \qquad (4.54)$$

Equation (4.53) is the dispersion relation which is a fifth order polynomial in s. As in the ideal case, the first stage must be to appreciate the layout of the complete ballooning mode spectrum for the equilibrium considered. For zero perpendicular thermal conduction and zero resistivity it has been shown by Van der Linden and Goossens (1991) that the continuous spectrum consists of an Alfvén continuum, a slow mode continuum and a thermal continuum (see also Chapter 3). The thermal continuum lies on the real s axis, so the next stage is to find out where it is located. After doing so, the dispersion relationship given by Equation (4.53) is solved numerically using a NAG routine (NAG Ltd., 1988). The five solutions are then plotted together with the thermal continuum (given by Equation (E.3) in Appendix E) with $m = 1$ for various values of ϵ in Figure 4.1.
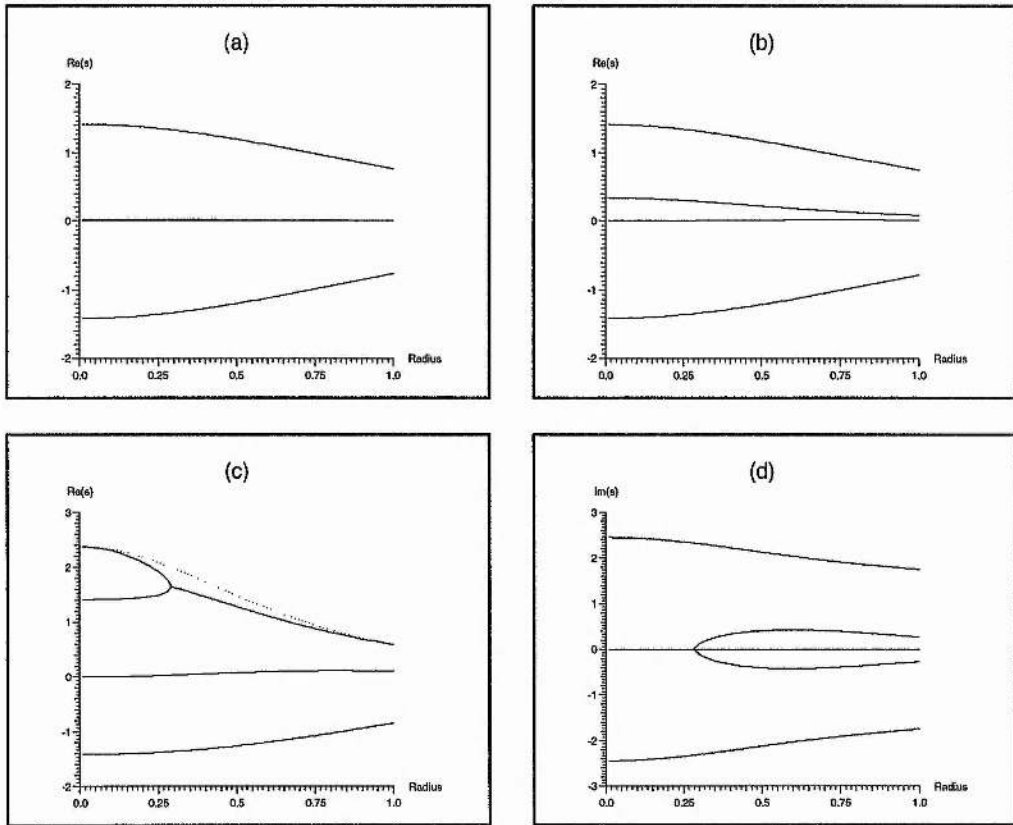
Figure 4.1: The solutions to the dispersion relation for various values of ϵ. Going from (a) to (c), the real part of the solutions are shown for $\epsilon = 16.9$, 1.2 and 0.17. In (d) the imaginary part of the solution corresponding to the real solution (c) is shown. The dashed line represents the thermal continuum.

Large values of ϵ can be thought of as modelling equilibria far from marginal stability whereas small values of ϵ correspond to equilibria close to marginal stability. In each of the four graphs, the radius ranges from 0 to 1, scaled to the radius of the cylinder and the growth rate s is scaled in terms of the Alfvén time scale. Because the fast modes have been eliminated in deriving the ballooning equations, it follows that the five solutions to the dispersion relation will represent the two Alfvén modes, the two slow modes and the thermal mode. It should be noted that these curves at this stage do not represent actual normal modes. These curves are investigated for various values of ϵ in Figure 4.1. For the large value of ϵ, taken in Figure 4.1(a), the Alfvén mode curves can easily be seen and are distinct, but the thermal

and slow mode curves together with the thermal continuum curve are very close to each other and have a small growth rate. When $\epsilon = 1.2$, Figure 4.1(b) shows that each curve can easily be seen. Going from top to bottom of the graph, the curves represent the Alfvén, thermal, slow and Alfvén modes. Here, as in the previous case, the thermal continuum lies almost on top of the thermal mode curve.
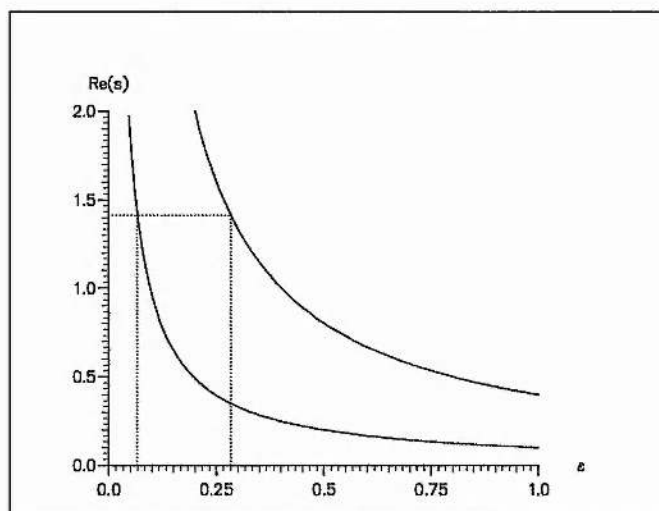
Figure 4.2: The location of the thermal continuum for various values of ϵ. The top curve is the maximum of the continuum and the lower curve is the minimum. The horizontal dotted line represents a growth rate of $\sqrt{2}$ and the vertical dotted lines represent the upper and lower values of ϵ for which $s = \sqrt{2}$ is the end points of the thermal continuum.
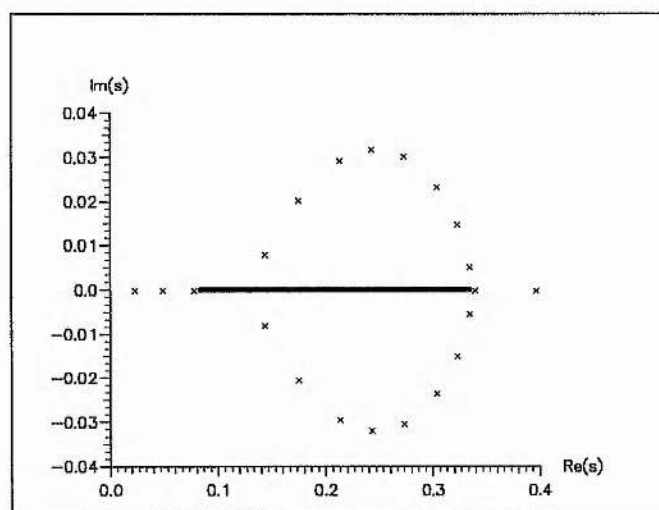
Figure 4.3: The fundamental Alfvén and magnetothermal modes with $\epsilon = 1.2$ for $m = 1$ and various values of the axial wave number k ranging from $k = 1.423$ to $k = 1.62$. The thermal continuum is represented by the solid fat line.

For a small value of ϵ ($\epsilon = 0.17$), it can be seen in Figure 4.1(c) that the lowest Alfvén and slow modes are distinct. However, the Alfvén and thermal modes coalesce at about $r \approx 0.28$ and form a pair of

overstable wave solutions. To confirm this, the imaginary part of the growth rate is plotted in Figure 4.1(d) and as before it can be seen that at $r \approx 0.28$ the modes coalesce. The thermal continuum is shown in Figure 4.1(c) as the dashed line lying above the two curves that coalesce.

Next the equations for normal modes (4.15)-(4.23) are solved using LEDA and the results presented. Before individual solutions are obtained, the location of the thermal continuum must be found for a fixed value of ϵ. The maximum and minimum values of the thermal continuum are shown in Figure 4.2. Notice that as ϵ gets larger, the maximum and minimum curves for the thermal continuum get closer together. As $\epsilon \to \infty$, the previous ideal case should be retrieved with the thermal continuum collapsing to a single point at the origin. By enlarging the ϵ axis to include larger values, the two curves converge to zero as expected.
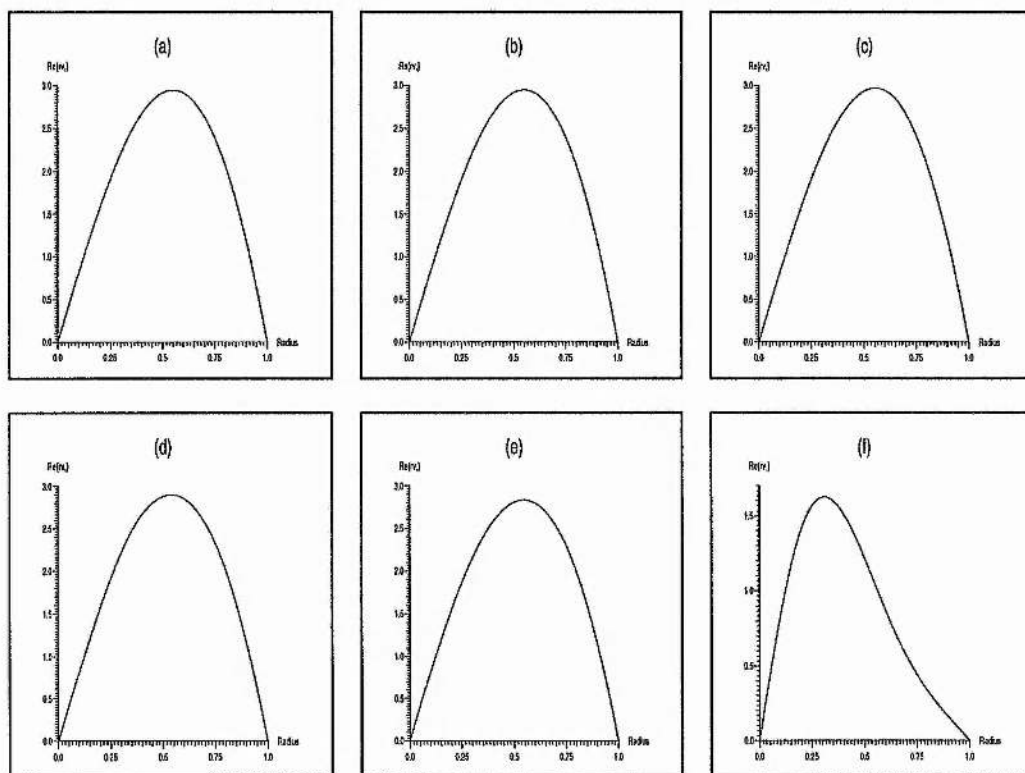
Figure 4.4: The eigenfunctions for various fundamental modes with $\epsilon = 1.1944$, $m = 1$ and various values of the axial wave number k. The fundamental Alfvén mode is shown in (a), (b), (e) and (f) and the fundamental magnetothermal mode is shown in (c) and (d). Going from (a) to (f), the values of k are 1.423, 1.4282, 1.4430, 1.5, 1.5795 and 10. The corresponding growth rates are 0.0248, 0.0777, $0.1565 + 0.0137i$, $0.2554 + 0.0318i$, 0.3398 and 1.2604. In each case 500 gridpoints were used to calculate these eigenfunctions.

Now that the location of the thermal continuum and shape of the localised ballooning curves are known for any value of ϵ, the thermal subspectrum can be investigated for various, fixed values of ϵ by solving the full Equations (4.15)-(4.23) using the finite element code LEDA. The fundamental unstable Alfvén mode is located on the real, positive s axis for small k and $m = 1$, below the thermal continuum. The wave number k is varied slowly since the interaction of this mode and the thermal continuum is important. Fixing $\epsilon = 1.2$ and for a value of $k = 1.4282$, with a corresponding growth rate of $s = 0.0777$, the fundamental Alfvén mode is very close to the lower end of the continuum which starts at $s = 0.0838$

at $r = 1$ and finishes at $s = 0.3349$ at $r = 0$. When k is varied, the growth rate of the fundamental Alfvén mode increases until it just touches the lower end of the thermal continuum, where upon it splits up into two magnetothermal modes that enter the complex s plane. As k is increased, these two modes travel around the continuum before rejoining the real axis above the maximum of the thermal continuum. On rejoining the real s axis, one mode, the thermal mode, travels down towards the maximum of the continuum, while the other mode, the Alfvén mode, travels up the real axis as k increases before it asymptotes towards a fixed value, see Figure 4.3. The $\mathrm{Re}(rv'_r)$ eigenfunctions of the fundamental Alfvén mode as it coalesces with the fundamental thermal mode to form a pair of overstable magnetothermal wave modes as the growth rate moves around the thermal continuum are shown in Figure 4.4. In the first two graphs (a) and (b), the fundamental Alfvén mode is below the thermal continuum. In the graphs (c) and (d), the fundamental magnetothermal mode lies above the thermal continuum in the complex plane. Finally in the last two graphs (e) and (f), the fundamental Alfvén mode is located above the thermal continuum on the real s axis.
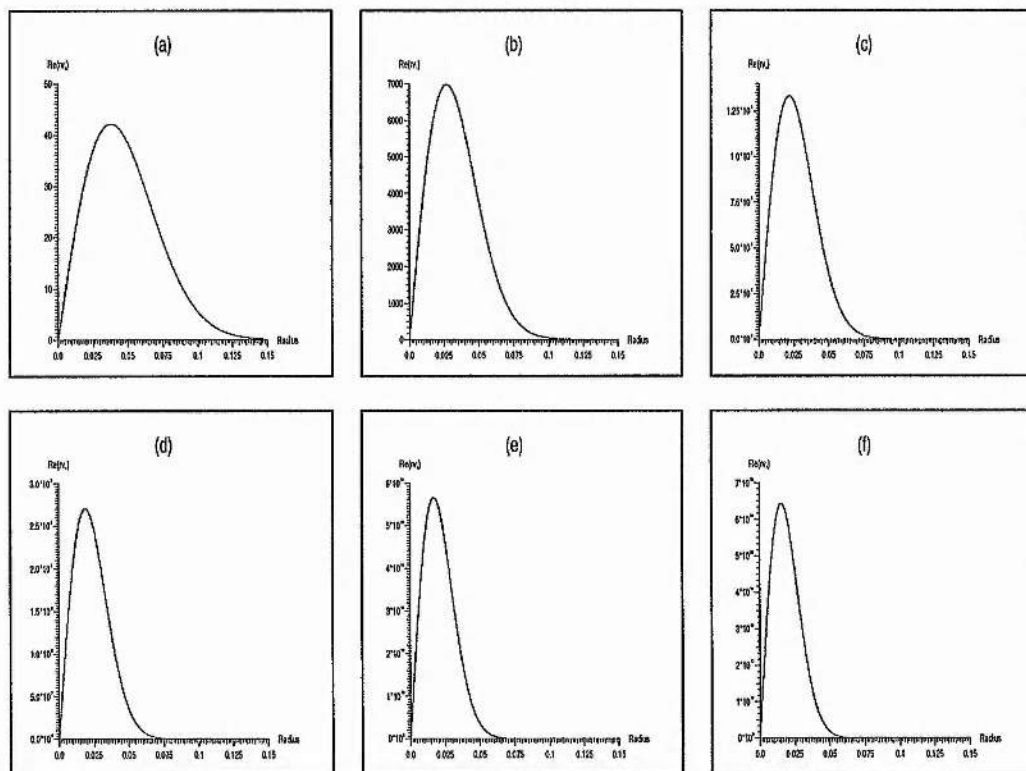
Figure 4.5: The fundamental Alfvén mode with $\epsilon = 1/\sqrt{2}$ for $m = 1$ and various values of the axial wave number k. Going from (a) to (f), the values of k are 500, 1,000, 1,500, 2,000, 2,500 and 3,000. The corresponding growth rates are 1.4102, 1.4122, 1.4129, 1.4132, 1.4134 and 1.4135. In each case 4,000 gridpoints were used to calculate these eigenfunctions. Note the expanded scale for r.

It is easy to see that the eigenfunctions change very little as the magnetothermal modes move around the continuum, but as k increases, the eigenfunctions get more and more localised. As in the ideal case, it is found that as k gets large the growth rate tends to a fixed, positive, real number. This is calculated by LEDA using 2,000 radial gridpoints. For three different values of k the growth rate is expanded as in Equation (4.28), and solved to give the values of s_0, s_1 and s_2. For values of k equal to 1,000, 1,500 and

2,000, it is found that $s_0 = 1.41421344$ and $s_1 = -1.83238$. To understand the qualitative differences in coupling of magnetic and thermal instabilities for equilibria far from or close to marginal stability, ϵ is varied in the following. Setting $\epsilon = 1/\sqrt{2}$, a similar study is carried out, with particular attention focused on the large k behaviour. When $k = 1,000, 2,000$ and $3,000$ and using $4,000$ gridpoints in LEDA, it is found that $s_0 = \sqrt{2}$ and $s_1 = -1.99996$. The eigenfunctions for this value of ϵ and for various, large values of k are shown in Figure 4.5. Notice that the eigenfunctions get more localised about $r = 0$ as k increases.
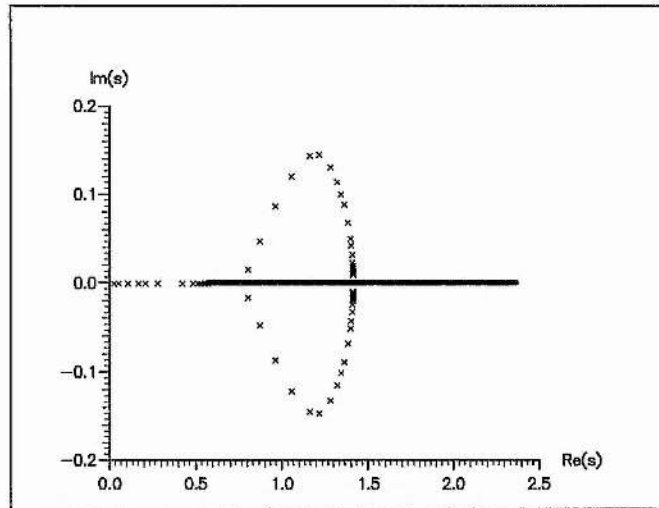
Figure 4.6: The fundamental Alfvén and magnetothermal modes with $\epsilon = 0.17$ for $m = 1$ and various values of the axial wave number k. The thermal continuum is represented by the solid fat line.
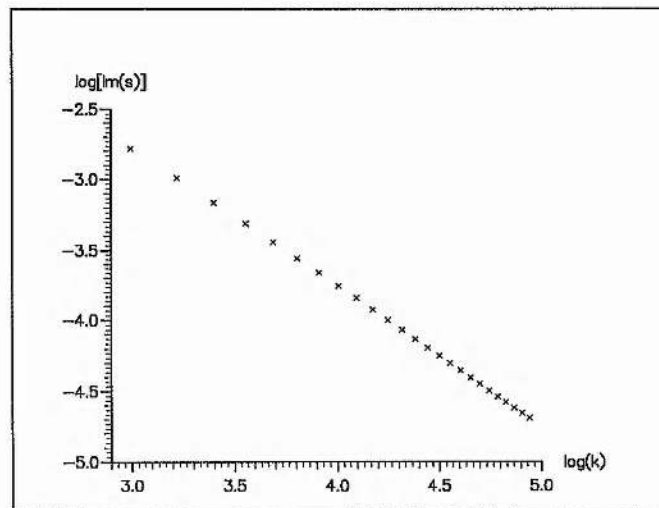
Figure 4.7: Plot of $\log \mathrm{Im}(s)$ against $\log k$ for the magnetothermal modes shown in Figure 4.6. The points lie on a straight line with a gradient of -1.

Now consider the case for a large value of ϵ. For $\epsilon = 16.9$, the thermal continuum lies between $s = 0.0237$

at $r = 0$ to $s = 0.0059$ at $r = 1$. For $k = 1.424$, the fundamental Alfvén mode is found above the maximum of the continuum, with a corresponding growth rate of $s = 0.0379$. Using large values of k equal to 1,000, 1,500 and 2,000, with corresponding growth rates of 1.4125, 1.4131 and 1.4134, with 2,000 gridpoints Equation (4.28) yields $s_0 = 1.41421349$ and $s_1 = -1.68232$. Comparing these values with the ones obtained in the ideal case it can be seen that the modification to s_1 is due to the effect of the non-ideal terms which are small because of the large value of ϵ. Consider next a small value of ϵ, $\epsilon = 0.17$. The thermal continuum lies between $s = 2.3680$ at $r = 0$ to $s = 0.5719$ at $r = 1$. The fundamental Alfvén mode for $k = 1.423$ is found below the minimum of the continuum, with a corresponding growth rate of $s = 0.0247$. The value of k is gradually increased until $k = 1.76$ which has a growth rate of $s = 0.5695$. This is just below the minimum value of the thermal continuum. When k in increased further, the fundamental Alfvén mode enters the complex plane and becomes the fundamental magnetothermal mode. As k increases further, the fundamental magnetothermal mode follows the curve shown in Figure 4.6. For this value of ϵ, the fundamental magnetothermal mode tends towards a fixed value inside the thermal continuum rather than splitting up into the fundamental thermal and Alfvén modes as in the previous cases when rejoining the real s axis.
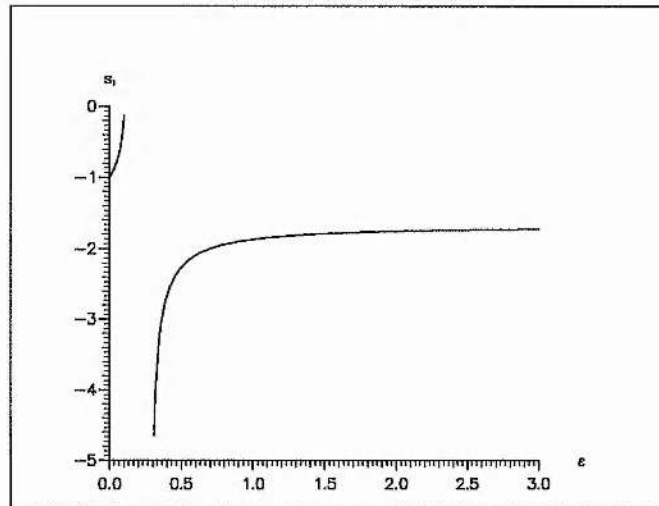
Figure 4.8: Plot of the correction term s_1 in Equation (4.55) against ϵ.

For any finite k the mode remains complex (overstable); only in the limit for $k \to \infty$ is a purely real (unstable) mode recovered. To confirm this, the values of $\log \text{Im}(s)$ are plotted against $\log k$ in Figure 4.7. As can be seen, the values plotted lie on a straight line, with gradient -1. Hence $\text{Im}(s) \sim k^{-1}$, so that as k tends to infinity, $\text{Im}(s)$ tends to zero and the fundamental magnetothermal mode enters the thermal continuum at $s \approx 1.4142$ as predicted by the eigenvalues corresponding to k equal to 50, 100 and 140 substituted into Equation (4.28).

Finally, an even smaller value of ϵ, $\epsilon = 0.01$ is considered. In this case, the thermal continuum lies between $s = 9.1$ at $r = 1$ to $s = 40.0$ at $r = 0$. The fundamental Alfvén mode is located below the thermal continuum. As k is increased, it is found that the value of the growth rate this mode asymptotes to is below the thermal continuum. For the values of k equal to 500, 600 and 700 with 750 gridpoints, it is found that $s_0 = 1.41421348$ and $s_1 = -0.96644$. Notice that in all the cases for ϵ dealt with so far, the value of s_0 has always been equal to $\sqrt{2}$. The large k behaviour for these values of ϵ can be predicted analytically. The ballooning equations are manipulated and a WKB analysis carried out. A detailed description of this is included in Appendix E. It is found that for $\lambda = 0$, the expansion for the

growth rate is given by

$$s = \sqrt{2} - \frac{2\left(n + \frac{1}{2}\right)}{k}\sqrt{\left(\frac{14\epsilon - \sqrt{2}}{5\epsilon - \sqrt{2}}\right)} + \cdots, \qquad (4.55)$$

where n is the mode number. Equation (4.55) yields a fair amount of information about large k behaviour. For any value of ϵ, Equation (4.55) gives $s_0 = \sqrt{2}$, so that as $k \to \infty$, $s \to \sqrt{2}$ for all ϵ. This is in agreement with the numerical results obtained. Care, however, must be used in applying the $1/k$ correction term in Equation (4.55). This was derived taking no account of the singularity corresponding to the thermal continuum. Therefore, whenever $s = \sqrt{2}$ lies within the thermal continuum, the correction term in Equation (4.55) will not give the correct value for s_1. Referring to Figure 4.2, it can be shown that $s = \sqrt{2}$ is at the maximum of the thermal continuum for $\epsilon = \sqrt{2}/5$ and $s = \sqrt{2}$ is at the minimum of the thermal continuum for $\epsilon = 0.0663$. Hence, the correction term in Equation (4.55) is valid for all ϵ except whenever $0.0663 \leq \epsilon \leq \sqrt{2}/5$. Equation (4.55) predicts the large k behaviour of all the Alfvén modes (or harmonics). In this work, attention is restricted to the fundamental Alfvén mode and so $n = 0$ in Equation (4.55). For large ϵ, the non-ideal terms are small and the results should behave as in the ideal case considered earlier. This is indeed so as can be seen in Equation (4.55), since as $\epsilon \to \infty$, $s \to \sqrt{2} - \frac{1}{k}\sqrt{\frac{14}{5}}$, the value previously predicted by Appendix D for the ideal case. To get an idea of how s_1 varies with the allowed values of ϵ, s_1 is plotted against ϵ in Figure 4.8. Substituting in the values of ϵ taken in the numerical work into Equation (4.55), the predictions for s_0 and s_1 can be made. These are summarised in Table 4.2. These results are in excellent agreement with the growth rates obtained by LEDA and again give confidence that the numerical results are accurate. The error in s_0 is $O\left(1/k^2\right)$ and s_1, $O\left(1/k\right)$. For the results in which k=1,000, the error in s_0 is therefore 10^{-6} and in s_1 is 10^{-3}.

Value of ϵ	Values of k	Value of s_0	Value of s_1	Prediction of s_1
16.9	1,000, 1,500, 2,000	1.41421349	-1.68232	-1.68245
1.2	1,000, 1,500, 2,000	1.41421344	-1.83238	-1.83262
$1/\sqrt{2}$	1,000, 2,000, 3,000	1.41421355	-1.99996	-2
0.17	50, 100, 140	1.414207	$\pm 1.2946i$	$\pm 1.2931i$
0.01	500, 600, 700	1.41421348	-0.96644	-0.96645

Table 4.2: Summary of the values of s_0 and s_1 found numerically, for a fixed value of ϵ and large k. The predictions for the correction term s_1 given by Equation (4.55) can be compared to the numerical values. Agreement is found correct to 3 decimal places for large values of k.

As in the previous ideal case, these results could be made more accurate by increasing the values of k and hence the number of gridpoints used to calculate the eigenvalues. Also, with a higher order WKB approximation, it should be possible to predict the value of s_2.

4.5.3 Ballooning modes for non-zero λ

In this Section, a non-zero component along the z direction is included in the equilibrium magnetic field. To model this a slightly different dispersion relation is obtained by setting $|\nabla S|^2 = B^2/B_\theta^2$ in Equation (4.51) to give

$$-\frac{\epsilon\rho^2\left(\gamma\beta p + B^2\right)B^2}{B_\theta^2\left(\gamma - 1\right)B_\theta^2}s^5 + \frac{\rho^2 B^4}{B_\theta^4}\left[-\left(\frac{\partial\widehat{\mathcal{L}}}{\partial p}\right)_T + \frac{\left(\beta p + B^2\right)\gamma}{\left(\gamma - 1\right)B^2}\sigma_R\right]s^4$$

$$- \quad \frac{\epsilon\rho}{r^2(\gamma-1)}\left[\gamma\beta p\left(\frac{B^2 m^2}{B_\theta^2}+4\right)+\frac{(\gamma\beta p+B^2)}{B_\theta^2}\left(m^2 B^2+2r\beta\frac{dp}{dr}\right)\right]s^3$$

$$+ \quad \frac{\rho}{r^2}\left[\frac{\gamma\beta p}{(\gamma-1)}\sigma_R\left(\frac{m^2 B^2}{B_\theta^2}+4+\frac{(\beta p+B^2)}{\beta p B_\theta^2}\left(m^2 B^2+2r\beta\frac{dp}{dr}\right)\right)-\frac{B^2}{B_\theta^2}m^2 B^2\left(\frac{\partial\hat{\mathcal{L}}}{\partial p}\right)_T\right]s^2$$

$$- \quad \frac{m^2\gamma\beta p}{(\gamma-1)r^4}\left(m^2 B^2+2r\beta\frac{dp}{dr}\right)(\epsilon s-\sigma_R) \quad = \quad 0. \tag{4.56}$$

To be able to compare the WKB analysis with numerical results, a parameter n is introduced throughout the work in this Section. The wave numbers k and m both depend on this integer parameter n, where $m = n + M$ and $k = -n/\lambda$. As before, the value of $M = 1$.
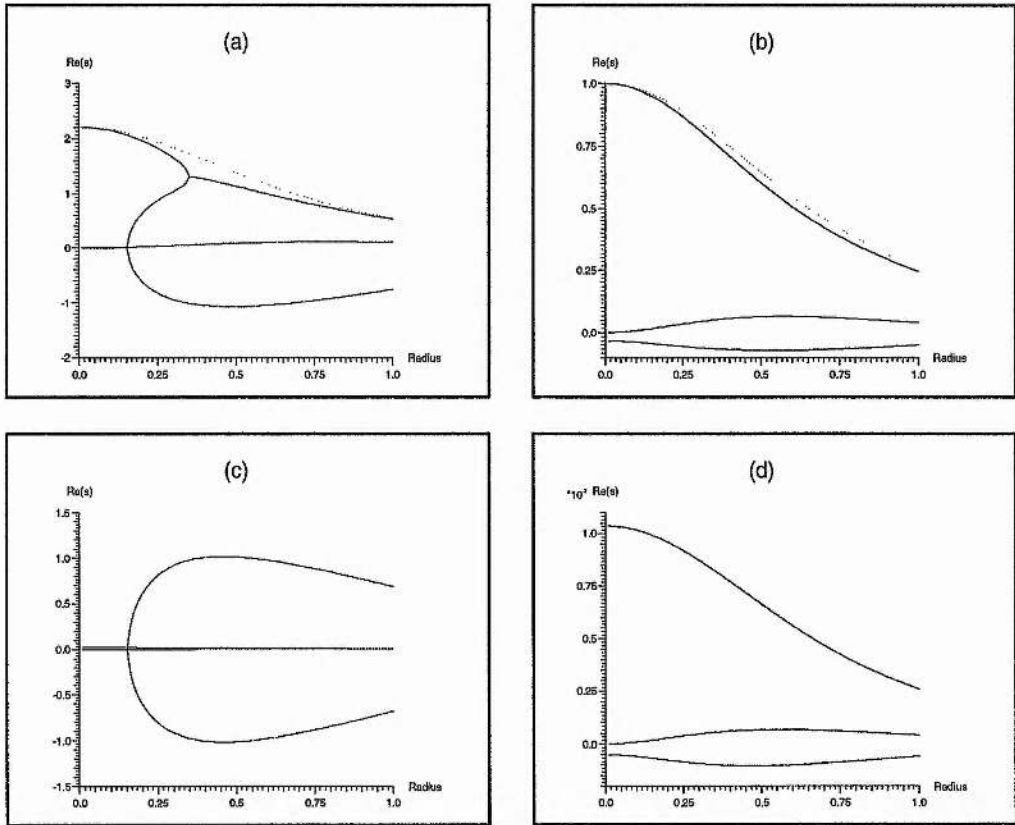
Figure 4.9: The solutions to the dispersion relation for various values of λ. In (a) and (b), the real part of the solutions are shown for ϵ=0.17 with $\lambda = 0.25$ and 0.75. In (c) and (d), ϵ =16.9 and $\lambda = 0.25$ and 0.75.

This guarantees that the mode has the same variation along the magnetic field as in the previous section. The dispersion relation given by Equation (4.56) is solved as in the previous case for $\lambda = 0$ and $m = 1$. The five solutions for two values of ϵ and various values of λ are shown in Figure 4.9 together with the thermal continuum represented by the dotted line which was calculated with n=1,000 and $M = 1$. Notice that in Figures 4.9(a) and (b), the thermal continuum and the thermal mode curves coincide at $r = 0$. In Figures 4.9(c) and (d), the thermal continuum cannot be distinguished from the corresponding thermal mode ballooning curves.

Taking $\epsilon = 16.97$ and $\lambda = 0.25$, the thermal continuum lies between $s = 0.0222$ at $r = 0$ to $s = 0.0055$ at $r = 1$. For a value of $n = 1$, the fundamental Alfvén mode was located above the maximum of the thermal continuum with a growth rate of $s = 0.6862$. For large values of n, information can be gained from the dispersion relation given by Equation (4.56). In Figure 4.9(c) it can be seen that the Alfvén modes have a maximum growth rate associated with them. This growth rate was calculated analytically and found to be $s = 1.01556585 = s_{max}$ which occurred at a radius of $r = 0.4567 = r_{max}$. Therefore, for large values of n, the fundamental Alfvén mode should asymptote to a growth rate of s_{max} and should be extremely localised at a radius of r_{max}. Notice that this is one point that differs from the work for $\lambda = 0$.
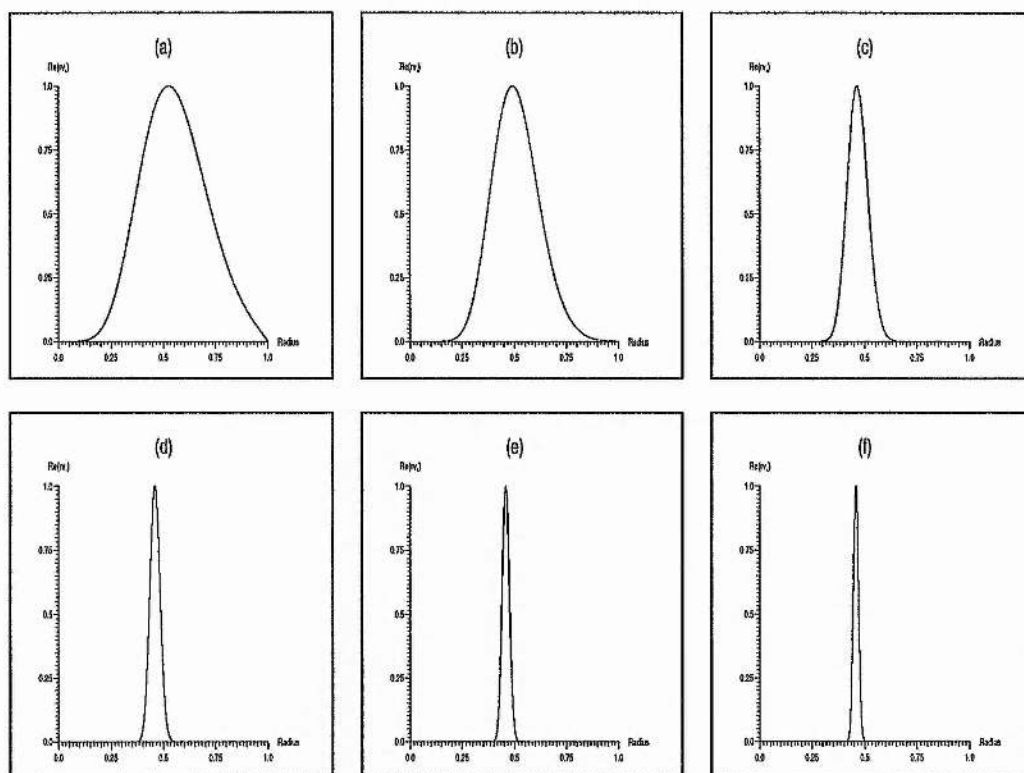
Figure 4.10: The fundamental Alfvén mode with $\epsilon = 16.9$ and $\lambda = 0.25$ for various values of the parameter n. Going from (a) to (f), the values of n are 5, 10, 50, 200, 400 and 800. The corresponding growth rates are 0.9611, 0.9875, 1.0098, 1.0141, 1.0148 and 1.0152. In each case 4,000 gridpoints were used to calculate these eigenfunctions.

In that Section, for this value of ϵ, the fundamental Alfvén mode was localised around the origin, but here, the fundamental Alfvén mode is localised at a point $r = r_{max}$. This means that the previous analysis carried out for $\lambda = 0$ for which r was assumed to be small cannot be easily adapted to model this case. Again, LEDA was used to calculate the fundamental Alfvén mode as n was varied. Figure 4.10 shows how the fundamental Alfvén mode behaves as n increases. As n gets larger, it can easily be seen that the fundamental Alfvén mode becomes increasingly more localised. The values of the radius corresponding to the maximum of the mode are given in Table 4.3. From Table 4.3, it can be seen that as n gets large, the values for the radius of the maximum approach the value of r predicted by the ballooning equations. As in the previous cases, the corresponding eigenvalues for the curves shown in Figure 4.10 are expressed in the asymptotic form for large n as

$$s = s_0 + \frac{s_1}{n} + \frac{s_2}{n^2} + \dots \tag{4.57}$$

For all values of n chosen, the value of s_0 predicted by the ballooning equations is correct to 4 decimal places, however for the values of $n = 200, 400$ and 800, agreement is particularly good, with $s_0 = 1.015565843$ and $s_1 = -0.290752$. For this value of ϵ, the effect of varying λ is examined.

Values of n	Values of r	Values of s
5	0.5256	0.9611
10	0.4911	0.9875
50	0.4636	1.0098
200	0.4584	1.0141
400	0.4576	1.0148
800	0.4571	1.0152

Table 4.3: The values of radius that correspond to the maximum value of the eigenfunction for the solutions shown in Figure 4.10 and corresponding values of n shown. Here $\epsilon = 16.9$.

The maximum of the ballooning curves (corresponding to the value s_0) are evaluated for various values of λ and are plotted in Figure 4.11. Notice that as λ increases, the value of s_0 decreases quite rapidly, until $\lambda \approx 0.6$, where the growth rate becomes very small.
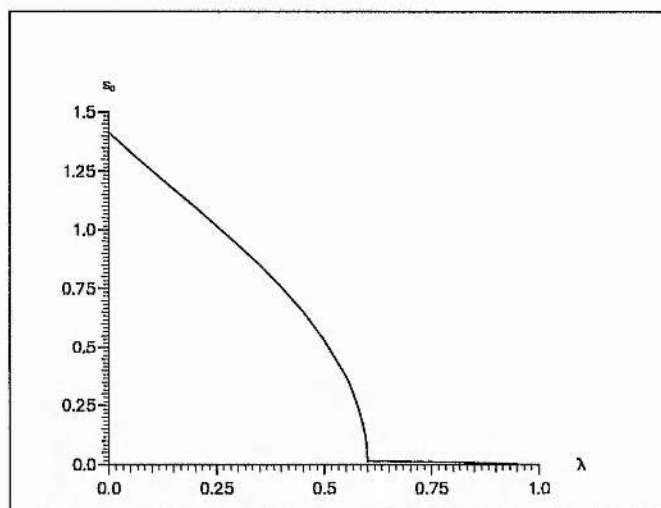
Figure 4.11: The values of the growth rate s_0, predicted by finding the maximum of the ballooning curve, plotted against λ for $\epsilon = 16.9$.

This is a consequence of the ideal modes becoming stable and the thermal mode being picked up. Thus for this particular value of ϵ, increasing the magnetic field in the z direction decreases the growth rate that the fundamental Alfvén mode asymptotes to as $n \to \infty$. The case for small ϵ is investigated next.

For $\lambda = 0.25$ and $\epsilon = 0.17$, the thermal continuum is located between $s = 0.5366$ at $r = 1$ to $s = 2.2006$ at $r = 0$. For $n = 1$, the fundamental magnetothermal modes are located in the complex plane with growth rates of $s = 0.8120 \pm 0.1645i$.
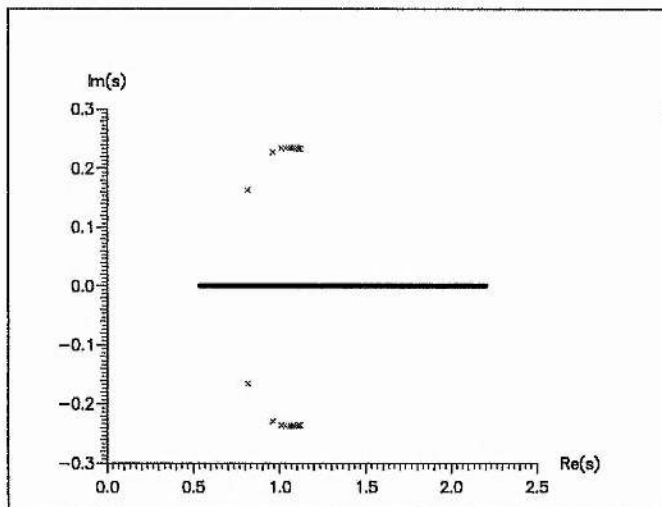
Figure 4.12: The fundamental magnetothermal modes with $\epsilon = 0.17$ for $M = 1$, $\lambda = 0.25$ and various values of the parameter n. The thermal continuum is represented by the solid line.

As n is increased up to $n = 53$ the fundamental magnetothermal mode remains in the complex plane as can be seen in Figure 4.12. Unfortunately, magnetothermal modes corresponding to values of $n > 53$ could not be calculated numerically due to poor convergence in LEDA. However, it can easily be seen that magnetothermal modes do exist for these values of n, ϵ and λ. It may be expected that as $n \to \infty$ the magnetothermal modes join the thermal continuum at $s = \sqrt{2}$.

4.6 Chapter Summary

This Chapter has investigated joint magnetic and thermal instabilities (magnetothermal instabilities) in a simple cylindrical equilibrium. In the ideal case, for a shearless equilibrium magnetic field, the fundamental Alfvén mode was located on the real s axis for a small value of the axial wave number k, and a fixed value of the azimuthal wave number m. As the value of k was increased, it was found that the fundamental Alfvén mode became more localised around $r = 0$, whilst the growth rate headed towards a fixed, larger value. This growth rate was predicted by expanding the Hain-Lüst equation for small r and large kr. A WKB analysis was performed and agreement with the numerical results was obtained.

A similar study was also performed in the non-ideal case for a shearless equilibrium magnetic field configuration when perpendicular and parallel thermal conduction were neglected. The dispersion relation was derived via the use of the ballooning approximation and the five roots plotted. The thermal continuum was located on the real s axis and plotted also. The normal mode solutions were then obtained for various values of ϵ, the ratio of the coronal radiation time scale to the Alfvén time scale.

The fundamental unstable Alfvén mode was found on the real s axis below the thermal continuum for a small value of k. For $\epsilon = 1.2$, as k was increased, the fundamental Alfvén mode just touched the lower end of the thermal continuum. It then entered the complex plane as the fundamental magnetothermal

modes before moving around to the top end of the continuum. It was found that when the fundamental magnetothermal modes rejoined the real s axis, they split up into two modes, the fundamental thermal mode which moved down towards the top end of the thermal continuum and the fundamental Alfvén mode which headed towards a fixed, larger growth rate which occurred as the wave number k was increased. The values of ϵ were then varied, to investigate the qualitative differences in the coupling of magnetic and thermal instabilities for equilibria far from or close to marginal stability.

For a large value of ϵ, the fundamental Alfvén mode was located on the real s axis above the thermal continuum and was found to asymptote towards a fixed growth rate as the wave number k increased.

For a small value of ϵ, $\epsilon = 0.17$ corresponding to the case when the plasma is close to ideal marginal stability when the growth time is larger than the radiation time, the fundamental Alfvén mode was located below the thermal continuum. As k was increased, the fundamental Alfvén mode just touched the lower end of the thermal continuum, before entering the complex plane. As the value of k was further increased, the fundamental magnetothermal modes headed back down towards the real s axis, close to the middle of the thermal continuum. Only in the limit $k \to \infty$ is a purely real, unstable continuum mode retrieved, with a corresponding growth rate $s = \sqrt{2}$.

For an even smaller value of ϵ, $\epsilon = 0.01$, the fundamental Alfvén mode was found on the real s axis below the thermal continuum, for a small value of k. As the value of k was increased, this mode asymptotes to a growth rate of $s = \sqrt{2}$, well below the minimum of the thermal continuum.

In all the above cases, it was found that as $k \to \infty$, $s \to \sqrt{2}$. Analytically, the growth rate was expanded in terms of $1/k$ and the values of s_0 and the first order correction term s_1 were predicted by manipulating the ballooning equations into a second order differential equation containing a large parameter k in it. This was solved by another WKB analysis. The resulting equation predicted $s_0 = \sqrt{2}$ for all values of ϵ. For $\epsilon < 0.0663$, $s_0 = \sqrt{2}$ was below the minimum of the thermal continuum and so magnetothermal modes were shown not exist. For $0.0663 \le \epsilon \le \sqrt{2}/5$, the fundamental magnetothermal modes approached $\sqrt{2}$ inside the thermal continuum as $k \to \infty$. For $\epsilon > \sqrt{2}/5$, $s_0 = \sqrt{2}$ is above the thermal continuum and hence mode coalescence will occur. For the values of ϵ studied where $s = \sqrt{2}$ was outside the thermal continuum, excellent agreement was obtained between the numerical and analytical results.

For a non-zero component of the equilibrium magnetic field in the z direction, the ballooning equations were manipulated to give a slightly different dispersion relation which was again solved numerically.

For a small value of ϵ, the fundamental magnetothermal mode was located in the complex plane with $n = 1$. As n was increased this mode was found to stay in the complex plane. The maximum value for n taken was $n = 53$. Above this value, the eigenfunction was found to be very difficult to calculate.

For a large value of ϵ and value of $n = 1$, the fundamental Alfvén mode was located on the real s axis and above the maximum of the thermal continuum. This mode travelled along the real s axis as n increased, before approaching a fixed, real, positive growth rate, $s_{\max}$. This mode was also found to be extremely localised about the point $r = r_{\max}$ for large values of n. These values were again calculated analytically and excellent agreement was found using the ballooning approximation.

This Chapter has therefore demonstrated that thermal and magnetic instabilities can interact to form magnetothermal instabilities. It is well known that the thermal instability may be important in prominence formation and that it is the magnetic instability which results in a prominence erupting into a flare. It is possible that a neighbouring thermal instability may trigger the magnetic instability, thus initiating the pre-flare phase. The oscillations observed just before a flare occurs may be explained in terms of overstable wave modes or magnetothermal modes. Magnetothermal modes could therefore play an important part in the eruption of prominences at the onset of solar flares.

Chapter 5

Line-tying in Coronal Arcades

*...if you don't happen to have any new nuts, changing the left
and right hand nuts over side to side will often bring an unused
part of their collars in line with the slot.*

      -Tim Millington, renewing an output-shaft oil seal.

*Instead of getting bigger and better bangs in the combustion
chambers, one could achieve unwelcome and expensive noises
lower down.*

      -Tim Millington, on how to tune an imp engine.

5.1 Overview

In this Chapter the effect of line-tying is considered in a coronal arcade. The ballooning equations which were introduced in Chapter 4 are manipulated to give a dispersion relation that is a quadratic in the square of the azimuthal wave number m if parallel thermal conduction is neglected, or a cubic in m^2 if parallel conduction is included. Rigid wall boundary conditions are applied to this dispersion relation. The dispersion relation is then solved numerically and the solutions plotted. Unfortunately, the expression for the thermal continuum in line-tied arcades is required since, the thermal continuum must play an important role in the proceedings. This calculation is long and by no means trivial and is left for future work.

5.2 Introduction

In Chapter 4, the combination of magnetic and thermal instabilities in a coronal arcade were examined in the absence of the effects of line-tying. It was demonstrated that for certain values of the ratio of the radiative time scale to the Alfvén time scale, the fundamental, unstable Alfvén mode could coalesce with the fundamental thermal mode to produce overstable magnetothermal modes. This is not a realistic situation since, in the solar corona the magnetic field lines are essentially of finite length and anchored to the photosphere. In the study of prominences, two types of magnetic field line structure have been examined. These correspond to normal and inverse polarity prominences (see Chapter 1 for more details). In both these types of prominence, the magnetic field lines emerge from the photosphere and forms an overlying arcade structure. Therefore, a more realistic prominence model will be one in which the magnetic field lines are anchored to the photosphere. This effect, known as line-tying, is included in this Chapter.

Line-tying is important in the formation of prominences in the solar corona since, without line-tying, the prominence could not form. In the solar corona, the Alfvén time scale is much shorter than the radiative (or thermal instability) time scale. Hence, any equilibrium would be destroyed by a magnetic instability long before the thermal instability could generate the cool condensation. It is therefore necessary for prominence formation to have a magnetically stable equilibrium before the thermal instability can generate the prominence. It is not difficult to conceive that anchoring the magnetic field lines in the photosphere (and thus restricting field line movement) will significantly influence the stability of the global magnetic field.

As the density of the photosphere is much larger than the density of the solar corona, perturbations occuring in the corona will not substantially move the endpoints of the photosphere-anchored magnetic field lines. Consequently, line-tying will be strongly stablising, as realised by Raadu (1972). Since line-tying has a substantial effect on the magnetic instability, it is important to study the effect of line-tying on the mode coalescence described in Chapter 4. In particular, it has to be established whether mode coalescence occurs. If so, the effect on the magnetothermal modes has to be investigated.

Hence, the model presented in Chapter 4 is extended to include line-tying and the method of solution examined. For comparison, exactly the same equilibrium profile is used, together with the ballooning equations. The layout of this Chapter is as follows: Section 5.3 recaps the ballooning and equilibrium equations considered and Section 5.4 discusses the boundary conditions which may be used. The method of solution is given in Section 5.5 and Section 5.6 summarises the results and discusses options for completing this work.

5.3   The basic equations

The equilibrium equations used are the Gold-Hoyle equilibrium equations which were described earlier in Chapter 4 and are produced here for convenience:

$$B_{\theta 0} \;=\; \frac{r}{(1 + r^2)}, \qquad B_{z0} \;=\; \frac{\lambda}{(1 + r^2)},$$

$$\beta p_0 \;=\; \frac{1 - \lambda^2}{2(1 + r^2)^2}. \tag{5.1}$$

A full description of this equilibrium magnetic field profile and its various properties is described in Chapter 4. The ballooning equations introduced in Chapter 4 for an isothermal equilibrium are

$$\mathbf{B} \cdot \nabla \phi \;=\; -\frac{sB^2}{|\nabla S|^2} A_\| , \tag{5.2}$$

$$\mathbf{B} \cdot \nabla A_\| \;=\; -\frac{\rho s\,|\nabla S|^2}{B^2}\phi + \frac{2B_\theta \beta}{rB^2}p_1, \tag{5.3}$$

$$\mathbf{B} \cdot \nabla u \;=\; -\frac{(\beta p + B^2)}{\beta p B^2}\left(s\beta p_1 + \frac{\beta}{B_\theta}\frac{dp}{dr}\phi\right) + sT_1 - \frac{2B_\theta}{rB^2}\phi, \tag{5.4}$$

$$\mathbf{B} \cdot \nabla p_1 \;=\; -\frac{s\rho B^2}{\beta}u + \frac{B^2}{|\nabla S|^2 B_\theta}\frac{dp}{dr}A_\| , \tag{5.5}$$

$$\left[\widehat{R}\frac{(\mathbf{B}\cdot\nabla)^2}{B^2} - \left(\frac{\partial\widehat{\mathcal{L}}}{\partial T}\right)_p - \frac{\gamma}{(\gamma - 1)}\epsilon sp\right]T_1 \;=\; -\left[\epsilon s - \left(\frac{\partial\widehat{\mathcal{L}}}{\partial p}\right)_T\right]p_1 - \frac{\epsilon}{B_\theta}\frac{dp}{dr}\phi, \tag{5.6}$$

with

$$\epsilon = \tau_{rad}/\tau_A, \quad \widehat{R} = \tau_{rad}/\tau_{cond} \quad \text{and} \quad \beta = \tau_A^2/\tau_s^2, \tag{5.7}$$

where ϕ is the electrostatic potential, which is, to leading order, related to the perpendicular component of the perturbed velocity, $A_\parallel$ is the parallel component of the vector potential, u is the parallel component of the perturbed velocity, T_1 is the perturbed temperature and p_1 is the perturbed plasma pressure. The time scales given by τ_A, τ_{rad}, τ_{cond} and τ_s are defined in Table 4.1 and S is given by

$$S = F(r) - \frac{rB_z}{B_\theta}\theta + z. \tag{5.8}$$

As in Chapter 4, for non-trivial solution, the determinant of the coefficients of these variables vanishes giving

$$m^4 \left(\frac{\gamma\beta p B_\theta^2 |\nabla S|^2}{(\gamma-1)r^4} \right)(\sigma_\mathrm{R} - \epsilon s)$$

$$+ \quad m^2 \left[\frac{s^2 \rho |\nabla S|^2 B^2}{r^2} \left(\epsilon s - \left(\frac{\partial\widehat{\mathcal{L}}}{\partial p}\right)_T \right) + \frac{\gamma}{(\gamma-1)r^2} \left(\frac{2\beta^2 p}{r}\frac{dp}{dr} + s^2 \rho |\nabla S|^2 (2\beta p + B^2) \right)(\sigma_\mathrm{R} - \epsilon s) \right]$$

$$+ \quad \frac{s^2\rho}{(\gamma-1)r^2}(\sigma_\mathrm{R} - \epsilon s)\left[4\gamma\beta p + \frac{2r\beta}{B_\theta^2}(\gamma\beta p + B^2)\frac{dp}{dr} \right] + \frac{2s^2\rho\beta B^2 \sigma_\mathrm{R}}{rB_\theta^2}\frac{dp}{dr}$$

$$- \quad \frac{\epsilon\rho^2(\gamma\beta p + B^2)|\nabla S|^2}{B_\theta^2(\gamma-1)}s^5 + \rho^2 |\nabla S|^2 \left[-\frac{B^2}{B_\theta^2}\left(\frac{\partial\widehat{\mathcal{L}}}{\partial p}\right)_T + \frac{(\beta p + B^2)\gamma}{(\gamma-1)B_\theta^2}\sigma_R \right]s^4 = 0, \tag{5.9}$$

where

$$\sigma_R = -\frac{(\gamma-1)}{\gamma p}\left[\left(\frac{\partial\widehat{\mathcal{L}}}{\partial T}\right)_p + \frac{m^2\widehat{R}B_\theta^2}{r^2 B^2} \right] \tag{5.10}$$

is the isobaric growth rate. Notice that Equation (5.9) can also be obtained by rearranging Equation (4.51) in Chapter 4. One major difference between this work and the previous work presented in Chapter 4 is that previously, the azimuthal wave number m was an integer whereas here m is restricted by the boundary conditions and need not be an integer. Notice that Equation (5.9) is a quadratic in m^2 when parallel thermal conduction is set equal to zero and a cubic equation in m^2 when parallel thermal conduction is included, provided $\gamma \neq 1$. Substituting the isothermal Gold-Hoyle equilibrium equations (5.1) with $\partial\widehat{\mathcal{L}}/\partial p = p_0$, $\partial\widehat{\mathcal{L}}/\partial T = (\alpha-1)p_0^2$, $\beta = 1$, $\widehat{R} = 0$ and $\alpha = -1$ into Equation (5.9), the following equation is obtained

$$\frac{(1-\lambda^2)}{4r^2(1+r^2)^6}\left\{ |\nabla S|^2 \left[2(\gamma-1)(1-\lambda^2) - 2\gamma\epsilon s(1+r^2)^2 \right] m^4 \right.$$

$$+ \quad \frac{1}{(1+r^2)}\left[\left(-4(1-\lambda^2) + s^2(1+r^2)^2 |\nabla S|^2 \right)\left(2(\gamma-1)(1-\lambda^2) - 2\gamma\epsilon s(1+r^2)^2 \right) \right.$$

$$+ \quad s^2(\gamma-1)(r^2+\lambda^2)(1+r^2)|\nabla S|^2 \left(2\epsilon s(1+r^2)^2 - (1-\lambda^2) \right) \bigg] m^2$$

$$+ \quad \frac{(1-\lambda^2)}{4(1+r^2)}\left[8s^2(r^2+\lambda^2)\left(2\epsilon s(2-\gamma)(1+r^2)^2 - 2(1-\lambda^2)(\gamma-1) \right) \right.$$

$$+ \quad |\nabla S|^2 s^4(1+r^2)^2 \left(2(1-\lambda^2)(\gamma-1) - \epsilon s(1+r^2)(2\gamma + 4r^2 + 2\lambda^2(2-\gamma)) \right) \bigg] \bigg\} = 0, \tag{5.11}$$

where

$$|\nabla S|^2 = \left(\frac{dF}{dr}\right)^2 + \frac{\lambda^2}{r^2} + 1. \tag{5.12}$$

5.4 Boundary Conditions

Throughout the work in this Chapter, the effect of line-tying is implemented by letting the magnetic field lines be anchored to the photosphere at $\theta = \pm\pi/2$. Since Equation (5.9) is a fourth-order polynomial in m, when parallel thermal conduction is neglected, four boundary conditions (or line-tying conditions) are required. In the corona, the Alfvén time scale is around 5 seconds while in the photosphere it is about 100 seconds. Thus, the photosphere cannot respond to Alfvénic disturbances in the corona and coronal perturbations do not effect the photosphere. It is also difficult to conceive how a small perturbation of a plasma, with the density of the corona, can effect the much denser photospheric plasma. Hence, two of the boundary conditions used for a coronal arcade require that the component of the perturbed velocity perpendicular to the equilibrium magnetic field vanish at the photospheric interface

$$v'_\perp = 0 \quad \text{at} \quad \theta = \pm\frac{\pi}{2}. \tag{5.13}$$

Another two boundary conditions are needed. These concern the parallel component of the perturbed velocity. They have been a great source of controversy over the past decade. Two possible sets have been considered recently. One set of conditions was proposed by Einaudi and Van Hoven (1981, 1983), who argued that the best boundary conditions to use were where the plasma's energy was conserved, but, the parallel component of the perturbed velocity was non-zero

$$v'_\parallel \big|_{\theta=-\pi/2} = v'_\parallel \big|_{\theta=\pi/2}, \tag{5.14}$$

and

$$\frac{\partial v'_\parallel}{\partial n}\bigg|_{\theta=-\pi/2} = -\frac{\partial v'_\parallel}{\partial n}\bigg|_{\theta=\pi/2}, \tag{5.15}$$

where n is a field aligned co-ordinate. The conditions given by Equations (5.14) and (5.15) are known as flow through conditions. The second set of boundary conditions have been used by many authors, for example, Hood (1986a), Cargill and Hood (1989) and Hardie, Hood and Allen (1991). They argue that the best conditions to use are where the parallel perturbed velocity vanishes at the photosphere

$$v'_\parallel = 0 \quad \text{at} \quad \theta = \pm\frac{\pi}{2}. \tag{5.16}$$

The conditions given by Equations (5.16) are known as rigid wall conditions. Hood (1986a) compared these two sets of boundary conditions and concluded that rigid wall conditions were best for ideal MHD modes with relatively high frequencies and that flow through conditions were best for slower thermal or resistive instabilities. Since the aim of this Chapter is to investigate mode coalescence in a line-tied arcade, the boundary conditions used will be the rigid wall conditions.

Notice that if parallel thermal conduction is included in the analysis, the dispersion relation given by Equation (5.9) is a cubic in m^2 and hence, a further set of boundary conditions is required. These are usually applied to the perturbed temperature and are another controversial matter. There are two favoured sets of thermal boundary conditions which could be used. The first set of boundary conditions

treat the photosphere as a perfectly, thermally conducting plasma of fixed temperature so that

$$T' \;=\; 0 \quad \text{at} \quad \theta \;=\; \pm \frac{\pi}{2}. \tag{5.17}$$

The second possibility is to treat the photosphere as a perfect insulator (no heat flux into the photosphere) with the result that

$$\frac{\partial T'}{\partial n} \;=\; 0 \quad \text{at} \quad \theta \;=\; \pm \frac{\pi}{2}. \tag{5.18}$$

The thermal boundary conditions given by Equation (5.17) are probably the most realistic to use in practice, since it is difficult to conceive how the diffuse corona could significantly increase the temperature of the photosphere. However, if time and resources permit, the best idea would be to consider both these conditions in turn and compare the results.

5.5   Method of Solution

For simplicity, the solutions are split up into even and odd terms. The boundary conditions given by Equations (5.13) and (5.16) are applied to the dispersion relation using the following procedure. The electrostatic potential ϕ in the ballooning equations is related to the perpendicular component of the perturbed velocity $v'_\perp$ by the simplified version of Ohm's law (see Equation (4.37) in Chapter 4) and u is the parallel component of the perturbed velocity. Hence, the boundary conditions will be satisfied if

$$\phi \;=\; 0 \quad \text{at} \quad \theta \;=\; \pm \frac{\pi}{2}, \tag{5.19}$$

and

$$u \;=\; 0 \quad \text{at} \quad \theta \;=\; \pm \frac{\pi}{2}. \tag{5.20}$$

The even solutions are given by

$$\phi \;=\; a \cos m_1 \theta + b \cos m_2 \theta, \tag{5.21}$$

and

$$u \;=\; A \sin m_1 \theta + B \sin m_2 \theta, \tag{5.22}$$

where a, b, A and B are functions of radius and growth rate and m_1^2 and m_2^2 are the solutions to the dispersion relation given by Equation (5.11). Substituting Equation (5.21) into the ballooning equations (5.2)-(5.4) gives

$$A \;=\; \frac{2\left(1+r^2\right)^2}{s\left(r^2+\lambda^2\right)} \left[\frac{|\nabla S|^2 \, m_1^2}{2s\left(1-\lambda^2\right)} + \frac{s\,|\nabla S|^2}{4} - \frac{2}{s\left(1+r^2\right)} \right] am_1, \tag{5.23}$$

and

$$B \;=\; \frac{2\left(1+r^2\right)^2}{s\left(r^2+\lambda^2\right)} \left[\frac{|\nabla S|^2 \, m_2^2}{2s\left(1-\lambda^2\right)} + \frac{s\,|\nabla S|^2}{4} - \frac{2}{s\left(1+r^2\right)} \right] bm_2. \tag{5.24}$$

Applying the boundary conditions given by Equations (5.19) and (5.20) to Equations (5.21) and (5.22) gives

$$a \cos\left(\frac{m_1 \pi}{2}\right) + b \cos\left(\frac{m_2 \pi}{2}\right) \;=\; 0, \tag{5.25}$$

and

$$A \sin \left(\frac{m_1 \pi}{2} \right) + B \sin \left(\frac{m_2 \pi}{2} \right) \; = \; 0. \tag{5.26}$$

Using Equations (5.23) and (5.24), Equations (5.25) and (5.26), can be combined to give

$$\left[\alpha m_1^2 + \beta \right] m_1 \tan \left(\frac{m_1 \pi}{2} \right) \; = \; \left[\alpha m_2^2 + \beta \right] m_2 \tan \left(\frac{m_2 \pi}{2} \right), \tag{5.27}$$

where

$$\alpha \; = \; 2 \left(1 + r^2 \right) |\nabla S|^2, \tag{5.28}$$

and

$$\beta \; = \; \left(1 - \lambda^2 \right) \left(1 + r^2 \right) s^2 \, |\nabla S|^2 - 8 \left(1 - \lambda^2 \right). \tag{5.29}$$

Similarly for the odd modes given by

$$\phi \; = \; a \sin m_1 \theta + b \sin m_2 \theta, \tag{5.30}$$

and

$$u \; = \; A \cos m_1 \theta + B \cos m_2 \theta, \tag{5.31}$$

the boundary conditions become

$$\left[\alpha m_1^2 + \beta \right] m_1 \cot \left(\frac{m_1 \pi}{2} \right) \; = \; \left[\alpha m_2^2 + \beta \right] m_2 \cot \left(\frac{m_2 \pi}{2} \right). \tag{5.32}$$

Following Chapter 4, dF/dr is set equal to zero in Equation (5.12). The ballooning equations, subject to the line-tied boundary conditions, are solved on each magnetic flux surface. The maximum of the ballooning growth rate, as a function of the flux co-ordinate r may then be obtained. This maximum growth rate should correspond to the most unstable physical mode. It should be noted that proof of this statement has yet to be obtained for non-ideal MHD. Unfortunately, at present, it is not possible to verify this result. However, a numerical code which is capable of solving the equations describing normal modes in line-tied arcades could possibly be obtained by adapting POLLUX, the finite element code used by Van der Linden (1991) to obtain normal modes solutions subject to line-tying boundary conditions in a coronal loop.

To check Equations (5.11) and (5.27) set $\gamma = 1$, $\lambda = 0$ and $|\nabla S|^2 = 1$. This yields

$$m^4 + \left[\frac{-4}{(1 + r^2)} + \left(1 + r^2 \right) s^2 \right] m^2 + \left[\frac{-2s^2 r^2}{(1 + r^2)} + \frac{s^4}{4} \left(1 + 2r^2 \right) \right] \; = \; 0, \tag{5.33}$$

and

$$\left(\frac{E_i - m_1^2 G}{m_1} \right) \tan \left(\frac{m_1 \pi}{2} \right) \; = \; \left(\frac{E_i - m_2^2 G}{m_2} \right) \tan \left(\frac{m_2 \pi}{2} \right), \tag{5.34}$$

where

$$E_i \; = \; -\frac{1}{2} \left(\frac{-4r^2}{(1 + r^2)} + \frac{s^2}{2} \left(1 + 2r^2 \right) \right), \tag{5.35}$$

and

$$G = \frac{1}{2}\left(1 + 2r^2\right). \tag{5.36}$$

These are the same Equations obtained by Hardie, Hood and Allen (1991) by allowing $\gamma = 1$, $k^2 = 1$, $\rho_0 = 1/2$ and $\eta = 0$. The boundary conditions obtained give a relationship between m_1 and m_2.

The next step is therefore to solve the dispersion relation given by Equation (5.11) subject to the boundary conditions given by Equation (5.27) numerically and plot the obtained growth rate s against the cylinder radius r. As a check for the equations and numerical code, the case studied by Hardie, Hood and Allen (1991) is considered first. In Figure 5.1, the solutions to the dispersion relation subject to the boundary conditions for $\epsilon=1,000$ and $\gamma = 1$ are plotted. The dotted curve corresponds to $\rho_0 = 1/2$, the value taken by Hardie, Hood and Allen (1991) and the solid curve corresponds to $\rho_0 = p_0$ for the equilibrium plasma pressure p_0 defined in Equation (5.1).
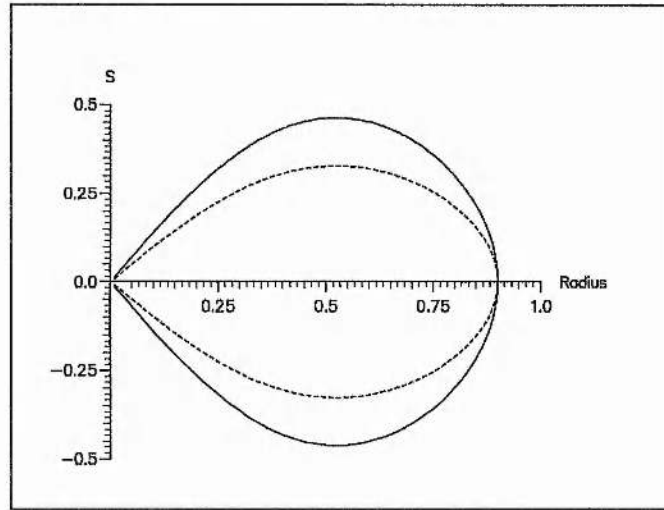

Figure 5.1: The solutions to the dispersion relation given by Equation (5.9) subject to the boundary condition given by Equation (5.27) when $\epsilon=1,000$ and $\gamma = 1$. The dotted curve corresponds to $\rho_0 = 1/2$, the value taken by Hardie et $al.$ (1991) and the solid curve corresponds to $\rho_0 = p_0$ for the equilibrium plasma pressure p_0 defined in Equation (5.1).

The dotted line can also be obtained from the solid curve by dividing the growth rates by $\sqrt{2}$. The curves cut the radius axis at $r = 0.90$. The maximum growth rate occurs at $r = 0.53$ and has a value of $s = 0.33$ for $\rho_0 = 1/2$ and $s = 0.46$ for $\rho_0 = p_0$. These curves correspond to the Alfvén modes. Thus, it may be expected that for large values of the axial wave number k, the most unstable, physical, magnetic instability would have a growth rate of $s = 0.33$ for the equilibrium profile where $p_0 = \rho_0$ or $s = 0.46$ for the equilibrium considered by Hardie et $al.$ (1991).

In Figure 5.2, the effect of having $\gamma = 5/3$ is examined. The top curve is the isobaric growth rate, given by Equation (5.10) for $\lambda = 0$ and $\widehat{R} = 0$. Going from top to bottom, the other curves correspond to $\lambda = 0.3$, 0.2, 0.1, 0.05 and 0. Notice that there is a distinct difference in behaviour between λ zero and non-zero close to $r = 0$. This is because of the λ^2/r^2 term in the $|\nabla S|^2$ terms of the dispersion relation. In all the cases investigated for $\lambda \neq 0$, the corresponding isobaric growth rate curves have met the solution curves at $r = 0$ and have a similar shape to the curve shown for $\lambda = 0$. The solution curves

in this case correspond to the thermal modes, since the Alfvén modes have been shown by Cargill, Hood and Migliuolos (1986) to be stable for $\gamma \geq 4/3$. Since the magnetic modes are stable, it would appear that for this value of ϵ, mode coalescence (yielding overstable magnetothermal modes) does not occur. To obtain magnetothermal modes, it is necessary to have both a magnetic instability and a thermal instability. This requires a value of $\gamma < 4/3$, so that a magnetic instability can form and a value of $\gamma \neq 1$, so that the thermal instability can be present. Thus, a value of γ should be taken such that both these instabilities may occur if magnetothermal modes are to be studied.
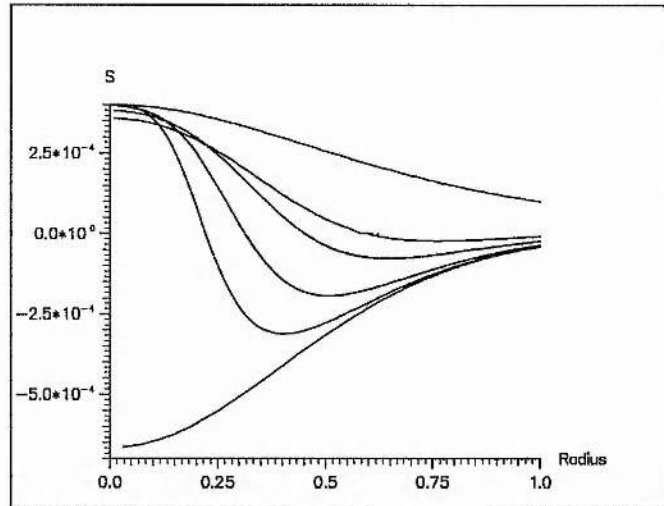

Figure 5.2: The solutions to the dispersion relation when ϵ=1,000, $\gamma = 5/3$ and various values of λ. The top curve is the isobaric growth rate given by Equation (5.10) when $\lambda = 0$ and $\widehat{R} = 0$. Going from top to bottom, the other curves correspond to $\lambda = 0.3$, 0.2, 0.1, 0.05 and 0.

So far, the thermal continuum has been neglected in this analysis. As seen in the previous Chapters, this had an important bearing on the stability of this equilibrium and hence the results obtained. Therefore, the results obtained are incomplete as an in-depth study of the thermal continuum in line-tied geometries is required. Unfortunately, the expression for the thermal continuum in line-tied arcades requires a long and difficult calculation. This is left for future work. Only when the location of the thermal continuum is known, can progress be made.

Once this expression is obtained, the influence of the thermal continuum on the thermal instability and mode coalescence can be assessed. Then, when the basic mechanism has been fully understood for a fixed value of ϵ, the next stage would be to vary ϵ to investigate mode coupling in equilibra close to or far from marginal stability.

5.6   Chapter Summary

This Chapter has introduced the effects of line-tying in a coronal arcade. The ballooning equations were manipulated to yield a dispersion relation. The various forms of the line-tying boundary conditions were discussed and rigid wall conditions chosen. These boundary conditions stated that the perturbed velocity of the plasma must vanish at the photospheric interface. The dispersion relation was then solved numerically subject to these rigid wall conditions and the solutions plotted.

The previous equations and the numerical results of Hardie *et al.* (1991) were obtained for $\gamma = 1$

and $\rho_0 = 1/2$ for a perfectly conducting (ideal) plasma. It was shown by Cargill *et al.* (1986) that for $\gamma = 5/3$, the ideal (magnetic) modes were stabilised. This was demonstrated for $\epsilon = 1,000$ and various values of λ in Figure 5.2. Figure 5.2 also showed that the thermal modes are unstable for certain values of λ.

However, these results were obtained without the knowledge of the thermal continuum in line-tied arcades. The expression for the thermal continuum in line-tied geometries is however necessary if further progress is to be made. This is left as a suggestion for future work.

Chapter 6

Summary and Future Work

*...But, even on cross-plies I can't get the back to hang out
and the car does understeer first but not as much as that nasty
little man from Top Gear seems to think.*

-Matthew Holingsworth, Imp club magazine, April 94.

*...I now use the words 'Tony Mason' as the worst possible form
of expletive.*

-Richard Llewellyn, Imp club magazine, June 94.

6.1 Thesis Summary

This thesis has examined several problems related to thermal instabilities in the solar corona. The work is important in facilitating the understanding of the formation and eruption of solar prominences.

Chapter 1 has described various solar phenomena both on and close to the solar surface. In particular, a detailed description of quiescent prominences and the associated fine scale structure is given. Several possible mechanisms for prominence formation are discussed. The thermal instability is the most likely candidate because it accounts not only for the prominence's formation but, also for the coronal cavity observed above the prominence.

Chapter 2 has described the thermal instability both physically and mathematically. For an infinite, uniform medium, first studied by Field (1965), the instability criteria are derived. From the description given in Chapter 2 it can be seen how a thermal instability may cause a prominence to form and why the prominence is cooler and denser than the surrounding corona.

The effect of finite, scalar resistivity and perpendicular thermal conduction on the thermal instability was examined in Chapter 3. In the absence of these two dissipative terms there are three continuous spectra associated with the linearised MHD equations, namely the Alfvén, slow and thermal continua. Neglecting resistivity but, including perpendicular thermal conduction, it was shown by Van der Linden and Goossens (1991) that the thermal continuum was removed but, the Alfvén and a modified slow continua remain. When the thermal continuum was removed, it was replaced by a quasi-continuum, the eigenfunctions of which varied rapidly over a length scale which was proportional to $(\kappa_\perp/\kappa_\parallel)^{1/4}$. When resistivity was included but perpendicular thermal conduction neglected, it was shown that the Alfvén and slow mode continua were removed and the only continuous spectrum remaining was the thermal continuum. The singularities corresponding to the thermal continuum for the cases with zero and non-zero resistivity were quite different. Nevertheless, it appeared that the two continua were similar when the Alfvén to radiative time scale ratio was small.

In the other cases the thermal continuum is strongly influenced by resistivity in a discontinuous manner, illustrating the singular nature of resistive MHD. For the equilibrium investigated, the new thermal continuum lies below the zero resistivity continuum. In addition, the zero resistivity continuum is replaced by a quasi-continuum, which consists of a dense set of discrete and continuous (in the spatial direction) normal modes. Finally, the inclusion of both resistivity and perpendicular thermal conduction removes all the continuous spectra, however, the thermal quasi-continuum remains.

The main numerical work in Chapter 3 concentrated on the effect of resistivity on the structure of the global normal modes. It is found that resistivity does not substantially reduce the growth rate associated with the maximum of the original thermal continuum, but, does remove the singular nature of the eigenfunctions.

The most unstable quasi-continuum mode was investigated for different values of the magnetic Reynolds number. It was found that the length scales associated with the oscillatory nature of the eigenfunctions scaled with $\eta^{1/4}$, the same fractional power as perpendicular thermal conduction. Thus, it is clear that resistivity can produce fine scale structure as the plasma cools. This is similar to the effect of perpendicular thermal conduction and in both cases the length scales of the fine structure scale with the diffusion coefficient to the power one quarter. Hence, classical values of these two diffusion coefficients will give rise to the typical length scales observed within quiescent prominences.

Chapter 4 has investigated joint magnetic and thermal instabilities (magnetothermal instabilities) using a simple cylindrical equilibrium. For a shearless equilibrium magnetic field configuration with perpendicular and parallel thermal conduction neglected, a dispersion relation was derived. This was achieved via the use of the ballooning approximation and the five roots plotted. The thermal continuum was located on the real s axis and was also plotted. The normal mode solutions were then obtained numerically for various values of ϵ, the ratio of the coronal radiation time scale to the Alfvén time scale.

The fundamental unstable Alfvén mode for a small value of k was found on the real s axis below the thermal continuum. For $\epsilon = 1.2$, as k was increased, the fundamental Alfvén mode just touched the lower end of the thermal continuum. It then entered the complex plane as a pair of fundamental magnetothermal modes before moving around to the top end of the continuum. It was found that when the fundamental magnetothermal modes rejoined the real s axis, they split up into two modes, the fundamental thermal mode which moved down towards the top end of the thermal continuum and the fundamental Alfvén mode which headed towards a fixed, larger growth rate which occurred as the wave number k was increased. This value was predicted analytically using a WKB analysis. The values of ϵ were then varied in order to investigate the qualitative differences in the coupling of magnetic and thermal instabilities for equilibria far from or close to marginal stability.

For a non-zero component of the equilibrium magnetic field in the z direction, the ballooning equations were manipulated to give a slightly different dispersion relation which was again solved numerically. For a large value of ϵ and value of $n = 1$, the fundamental Alfvén mode was located on the real s axis and above the maximum of the thermal continuum. This mode travelled along the real s axis as n increased, before approaching a fixed, real, positive growth rate, $s_{\max}$. This mode was also found to be extremely localised about the point $r = r_{\max}$ for large values of n. These values were again calculated using the ballooning approximation and excellent agreement was obtained.

Chapter 4 has demonstrated that thermal and magnetic instabilities can interact to form magnetothermal instabilities. It is well known that the thermal instability may be important in prominence formation and that it is the magnetic instability which results in a prominence erupting into a flare. It is possible that a thermal instability close to the prominence may trigger the magnetic instability, thus initiating the pre-flare phase. The oscillations observed prior to flares may be explained in terms of overstable wave modes or magnetothermal modes. Magnetothermal modes could therefore play an important part in the eruption of prominences at the onset of solar flares.

Finally, Chapter 5 examined the effects of line-tying in a coronal arcade. The ballooning equations

were manipulated to yield a dispersion relation which was solved numerically subject to rigid wall boundary conditions. The previous equations and numerical results of Hardie, Hood and Allen (1991) were obtained for $\gamma = 1$, $\rho_0 = 1/2$ in the ideal case. It was shown that for $\gamma = 5/3$, the ideal modes were stabilised and that only the thermal modes were unstable. However, this result was obtained without knowledge of the thermal continuum in line-tied arcades. Rigorous treatment requires the expression for the thermal continuum in line-tied geometries for progress to be made.

From these results, the following mechanism for a prominence's lifetime may be proposed. A thermal instability in the corona together with a dip in an arcade type magnetic field structure allows the prominence to form. A siphon mechanism may also aid this formation. As a consequence of resistivity and perpendicular thermal conduction, the observed fine scale structure can form. Finally, a neighbouring thermal instability may trigger off a magnetic instability causing the prominence to erupt into a solar flare.

6.2   Future Work

There are numerous possibilities for extending this work and these are discussed next.

Chapter 3 was concerned about how the inclusion of finite, scalar, temperature-dependent resistivity effected the normal mode spectrum of the linearised MHD equations. These equations were manipulated into a set of first-order ordinary differential equations. The singularities of these differential equations corresponded to continuous spectra. An alternative method of locating these singularities is to use the infinite gradient method described in more detail in Appendix B. The advantage of this method is that it is very quick to use, however the draw back is that it is not rigorous since it relies on all the variables being continuous across the singularity.

Although Chapter 3 has examined the effect of temperature-dependent resistivity on the continuous spectra, the normal mode solutions obtained have delt only with constant resistivity. Therefore, one extension to Chapter 3 would be to include the classic form of the temperature-dependent resistivity given by Equation (2.6) in Chapter 2.

Another extension to Chapter 3 would be to include dissipation due to viscosity. This may be achieved by adding the extra viscous terms to the momentum and energy equations. Unfortunately this is a very messy and complicated procedure because full treatment requires the inclusion of all the coefficients of viscosity (see Braginskii, 1965). Once these terms have been added, a similar method to that presented in Chapter 3 can be followed to ascertain the singularities (if any) of the corresponding system of first-order ordinary differential equations. Additional matrix elements may be calculated (using the method described in Appendix C) and programmed into LEDA together with possible additional surface terms and an appropriate set of boundary conditions. Then, as in Chapter 3, various parts of the normal mode spectrum can be studied. Thus, the effect of viscosity on the thermal instability can be discovered. If the thermal continuum is removed and replaced by a quasi-continuum (as is the case with resistivity or perpendicular thermal conduction) it may be possible to derive a scaling law for prominence fine scale structure. When including viscosity (for example) it may be easier to first work in a Cartesian geometry. Then, when the results are known, progress to a more realistic cylindrical geometry may be made.

In Chapter 3, the simplified version of Ohm's law (given by Equation (2.14) in Chapter 2) was used. The more lengthy and complicated generalised Ohm's law could be considered and corresponding results compared.

Different equilibria could be considered. For example, to model a laboratory plasma, a Tokamak-like current profile might be used.

This is more complicated than the Gold-Hoyle equilibrium profile and is well known in nuclear fusion research. It has been applied to solar physics by several authors, for example, An (1986)

$$B_\theta = B_c \frac{h_0}{2r\,(\nu+1)} \left[1 - \left(1-r^2\right)^{\nu+1}\right], \tag{6.1}$$

$$B_z = B_c, \tag{6.2}$$

$$p = p_c \left[\frac{1}{2}B^2 - \int_0^r \frac{B_\theta^2}{r'}dr' + c_0\right], \tag{6.3}$$

where ν, c_0 and h_0 are constants with B_c and p_c, the values of the magnetic field and the plasma pressure along the $r = 0$ axis of the cylinder respectively. There is still a free choice for either the density or temperature profiles. The following temperature profile might, for example, be chosen

$$T = h_0^2 \left(e_0 - r^2\right)^{d_0}, \tag{6.4}$$

where d_0 and e_0 are constants, with $e_0 > 1$ such that the temperature is non-zero throughtout the equilibrium and at the boundary $r = 1$. More realistic prominence equilibria could be created and used. It should be noted however, that the existence of the thermal continuum is a robust feature of the normal mode spectrum. The existence of the thermal continuum will therefore be independent of the choice of equilibria. The location of the thermal continuum and the eigenvalues and eigenfunctions obtained will, of course, vary from equilibrium to equilibrium.

So far Chapter 3 has only been concerned with continuous spectra in a one-dimensional cylinder. A more realistic situation would be to consider two-dimensional cylindrical equilibria, $\rho = \rho\,(r, z)$, etc. The method to obtain the continua should be very similar to that presented in Chapter 3. The linearised equations may be rearranged to give the two-dimensional Hain-Lüst equation. The singularities of this equation would then correspond to continuous spectra. The work corresponding to two-dimensional continua (gap continua) is currently being studied by Van der Linden and co-workers. Finally, the non-linear equations could be examined to investigate how non-linearity links up with the normal mode spectrum. In particular the effects on the thermal sub-spectrum could be ascertained.

In Chapter 4 another study of the normal mode spectrum was undertaken. The existence of magnetothermal modes was investigated. The fundamental thermal and Alfvén modes were found to coalesce for certain ratios of the radiative to Alfvén time scales to form overstable wave (or magnetothermal) modes. The work could be extended by investigating the coalescence of the higher harmonics. For the shearless Gold-Hoyle equilibrium profile with zero thermal conduction and no dissipation, the large k behaviour with $m = 1$ should be given by Equation (4.55), where k and m are the axial and azimuthal wave numbers respectively.

The WKB method used to predict the growth rate and first-order correction terms for large values of k could be extended to include the second-order correction term. The results presented in Chapter 4 could be obtained to any degree of accuracy required by increasing the values of k. This would require a larger number of gridpoints.

More dissipation could be included such as resistivity, perpendicular thermal conduction and viscosity. The first stage would involve knowledge of the continuous spectra. In the case of viscosity, the continuous spectra are unknown so they would first need to be calculated using the method described in the above paragraphs. The ballooning equations have already been derived with all these terms included by Hood, Van der Linden and Goossens (1989). These can be manipulated to form a dispersion relation which could be solved numerically following the method presented in Chapter 4. The large k behaviour may be studied and possibly predicted using a WKB analysis. This analysis may need to be extended

to accommodate complex growth rates. Thus, the use of Stokes and anti-Stokes lines may be required. More details may be obtained in Heading (1962).

In Chapter 4, the constraint $\mathbf{B} \cdot \nabla S = 0$ has been satisfied for a coronal arcade by setting

$$S = F(r) + z - q_1(r)\theta, \tag{6.5}$$

with

$$q_1(r) = \frac{rB_z}{B_\theta}. \tag{6.6}$$

Another study could be performed for a coronal loop by letting this constraint be satisfied by

$$S = F(r) + \theta - q_2(r)z, \tag{6.7}$$

with

$$q_2(r) = \frac{B_\theta}{rB_z}. \tag{6.8}$$

The effect of these two constraints on the thermal instability may then be compared. The Gold-Hoyle profile used in Chapter 4, although being simple and well known, is not a very realistic equilibrium profile in practise and could be replaced. The coalescence of the thermal and Alfvén modes could be studied in two and three dimensions. Finally, non-linear effects could play an important role in not only the ballooning modes but also on the thermal continuum and the coalescence of thermal and magnetic instabilities. Non-linear solutions could also coalesce with magnetic and thermal instabilities and may provide an insight into the mechanism associated with the eruption of prominences into solar flares.

In Chapter 5, the effect of line-tying is investigated for a coronal arcade. A discussion on the different types of boundary conditions which may be used is presented and the method of solution outlined. Unfortunately, it is necessary to calculate the continuous spectra (in particular the thermal continuum) and understand fully its' importance in line-tied geometries. Once the location of the thermal continuum is known, the solutions to the ballooning equations (with the boundary conditions satisfied) can be fully understood and applied to actual normal mode solutions. This will give a guide as to how line-tying effects the thermal instability. To calculate the thermal continuum in line-tied geometries, the methods previously discussed may be used. However, the effects of line-tying make the analysis of a one-dimensional equilibrium strictly two-dimensional.

Once the effect of line-tying on the thermal instability is known, dissipation effects such as parallel and perpendicular thermal conduction and resistivity could be included. Notice that if perpendicular thermal conduction is included, the thermal continuum is removed and replaced by a quasi-continuum. This may simplify the analysis.

As before, further extensions could consist of more realistic equilibrium profiles and the inclusion of non-linear terms.

The analytical fit to the optically thin radiation used throughout this thesis is that calculated by Rosner et al. (1978). Different analytical fits could be used, for example, Cook et al. (1989) and the results compared.

A currently unresolved matter in solar physics is the coronal heating function. Throughout this thesis, it is taken to be constant per unit mass, despite the fact that this is clearly unrealistic. Further advances in this work could be made once the specific form of the coronal heating function is known.

The resolution of the obsevations of prominences and the associated fine scale structure needs to be increased and this may then reveal other interesting (and maybe suprising) phenomena.

As technology and computing power increases, it makes these future options more accessible, hopefully enabling all the properties of the thermal instablity and solar prominences to be eventually fully understood.

Appendix A

A.1 The coefficients of Equations (3.48)-(3.53)

The coefficients of Equations (3.48)-(3.53) in Chapter 3 are

$$
C_1 = \frac{mp\eta}{r}C_{23} + \frac{1}{\mu}\left[s + \eta\left(\frac{m^2}{r^2} + k^2\right)\right] \times
$$

$$
\times \left[mpfC_0 + s^2\rho\left(rB_\theta\left(s\rho C_v + \frac{f^2\kappa_\parallel}{B^2} + \rho\left(\frac{\partial\mathcal{L}}{\partial T}\right)_\rho\right) + \frac{2p\eta}{rT}\frac{d}{dr}(rB_\theta)\right)\right], \tag{A.1}
$$

$$
C_2 = sp\left[s + \eta\left(\frac{m^2}{r^2} + k^2\right)\right]\left[\frac{sr}{T}\left(p\frac{d\rho}{dr} - \rho^2 C_v\frac{dT}{dr}\right) - \frac{d}{dr}(r\rho)C_0\right] - fprC_{23}, \tag{A.2}
$$

$$
C_3 = \frac{2s^2\rho p\eta}{\mu T}\left[s + \eta\left(\frac{m^2}{r^2} + k^2\right)\right]\frac{d}{dr}(rB_\theta) + mp\eta C_{23}, \tag{A.3}
$$

$$
C_4 = \frac{2s^2\rho rp\eta}{\mu T}\left[s + \eta\left(\frac{m^2}{r^2} + k^2\right)\right]\frac{dB_z}{dr} + krp\eta C_{23}, \tag{A.4}
$$

$$
C_5 = \frac{r}{\mu}\left[s + \eta\left(\frac{m^2}{r^2} + k^2\right)\right]\left[s^2\rho B_z\left(s\rho C_v + \frac{f^2\kappa_\parallel}{B^2} + \rho\left(\frac{\partial\mathcal{L}}{\partial T}\right)_\rho\right) + kpfC_0\right], \tag{A.5}
$$

$$
C_6 = -r\left[s + \eta\left(\frac{m^2}{r^2} + k^2\right)\right]\left[s^2\rho\left(s\rho C_v + \frac{f^2\kappa_\parallel}{B^2} + \rho\left(\frac{\partial\mathcal{L}}{\partial T}\right)_\rho\right) + \left(\frac{m^2}{r^2} + k^2\right)pC_0\right], \tag{A.6}
$$

$$
C_7 = -\left[s^2\rho + \frac{f^2}{\mu} + s\rho\eta\left(\frac{m^2}{r^2} + k^2\right)\right], \tag{A.7}
$$

$$
C_8 = \frac{1}{\mu r}\left[\frac{mf\eta}{r} - 2B_\theta\left(s + \eta\left(\frac{m^2}{r^2} + k^2\right)\right)\right], \tag{A.8}
$$

$$
C_9 = \frac{mf\eta}{\mu r}, \tag{A.9}
$$

$$
C_{10} = \frac{kf\eta}{\mu}, \tag{A.10}
$$

$$
C_{11} = \frac{B_z}{rp}C_6 + \frac{mg}{r}\left[s + \eta\left(\frac{m^2}{r^2} + k^2\right)\right]C_0, \tag{A.11}
$$

$$
C_{12} = \frac{B_z}{rp}C_1 + \frac{m}{r\mu}\left[\frac{m\eta}{r^2}\left(\frac{B_z}{r}\frac{d}{dr}(rB_\theta) - B_\theta\frac{dB_z}{dr}\right) - fB_z\left(s + \eta\left(\frac{m^2}{r^2} + k^2\right)\right)\right]C_0, \tag{A.12}
$$

$$C_{13} = \frac{B_z}{rp}C_5 + \left[s + \eta\left(\frac{m^2}{r^2} + k^2\right)\right]\left[s\rho\left(s + \eta\left(\frac{m^2}{r^2} + k^2\right)\right) + \frac{mfB_\theta}{r\mu}\right]C_0, \tag{A.13}$$

$$C_{14} = \frac{B_z}{rp}C_2 + \frac{1}{r}\left[s\rho\left(s + \eta\left(\frac{m^2}{r^2} + k^2\right)\right)\frac{d}{dr}(rB_z) - \frac{mf}{\mu}\left(\frac{B_z}{r}\frac{d}{dr}(rB_\theta) - B_\theta\frac{dB_z}{dr}\right)\right]C_0, \tag{A.14}$$

$$C_{15} = \frac{B_z}{rp}C_3 + \frac{m^2\eta}{\mu r^2}\left(\frac{B_z}{r}\frac{d}{dr}(rB_\theta) - B_\theta\frac{dB_z}{dr}\right)C_0, \tag{A.15}$$

$$C_{16} = \frac{B_z}{rp}C_4 - \frac{\eta}{r}\left[s\rho\left(s + \eta\left(\frac{m^2}{r^2} + k^2\right)\right) - \frac{mk}{\mu}\left(\frac{B_z}{r}\frac{d}{dr}(rB_\theta) - B_\theta\frac{dB_z}{dr}\right)\right]C_0, \tag{A.16}$$

$$C_{17} = \frac{B_\theta}{rp}C_6 - kg\left(s + \eta\left(\frac{m^2}{r^2} + k^2\right)\right)C_0, \tag{A.17}$$

$$C_{18} = \frac{B_\theta}{rp}C_1 + \left[s + \eta\left(\frac{m^2}{r^2} + k^2\right)\right]\left[s\rho\left(s + \eta\left(\frac{m^2}{r^2} + k^2\right)\right) + \frac{kfB_z}{\mu}\right]C_0$$
$$+ \frac{\eta}{r^2}\left[s\rho\left(s - \eta\left(\frac{m^2}{r^2} - k^2\right)\right) - \frac{mk}{\mu}\left(\frac{B_z}{r}\frac{d}{dr}(rB_\theta) - B_\theta\frac{dB_z}{dr}\right)\right]C_0, \tag{A.18}$$

$$C_{19} = \frac{B_\theta}{rp}C_2 + \left[s\rho\left(s + \eta\left(\frac{m^2}{r^2} + k^2\right)\right)\frac{dB_\theta}{dr} + \frac{2mf\rho\eta}{r^2}\left(s + k^2\eta\right)\right]C_0$$
$$+ \frac{kf}{\mu}\left[\frac{B_z}{r}\frac{d}{dr}(rB_\theta) - B_\theta\frac{dB_z}{dr}\right]C_0, \tag{A.19}$$

$$C_{20} = \frac{B_\theta}{rp}C_5 - \frac{kfB_\theta}{\mu}\left(s + \eta\left(\frac{m^2}{r^2} + k^2\right)\right)C_0, \tag{A.20}$$

$$C_{21} = \frac{B_\theta}{rp}C_3 - \frac{\eta\rho}{r}\left[\frac{m^2\eta}{r^2}\left(k^2\eta\left(1 + s\rho k\eta\right) + 2s\right) + s\left(s + \eta\left(\frac{m^2}{r^2} + k^2\right)\right)\right]C_0$$
$$- \frac{mk\eta}{r\mu}\left(\frac{B_z}{r}\frac{d}{dr}(rB_\theta) - B_\theta\frac{dB_z}{dr}\right)C_0, \tag{A.21}$$

$$C_{22} = \frac{B_\theta}{rp}C_4 - k\eta\left[\frac{2s\rho m\eta}{r^2} + \frac{k}{\mu}\left(\frac{B_z}{r}\frac{d}{dr}(rB_\theta) - B_\theta\frac{dB_z}{dr}\right)\right]C_0, \tag{A.22}$$

where

$$C_{23} = \frac{s^2\rho f\kappa_\parallel}{TB^2}\frac{dT}{dr} - \frac{1}{\mu}\left(\frac{m}{r^2}\frac{d}{dr}(rB_\theta) + k\frac{dB_z}{dr}\right)\left(C_0 + \frac{2s^2\rho\eta}{T}\right). \tag{A.23}$$

Appendix B

B.1 Infinite gradient method for obtaining singularities

In this Appendix, the infinite gradient method for locating singularities is presented. In ideal MHD it is well known that mobile regular singular points in the linear differential equations correspond to bands of singular wave solutions, or continuous spectra (see, for example, Goedbloed, 1983). Hence to derive the continuous spectrum for a cylindrical equilibrium with resistivity included, singularities are looked for in the equations obtained by transforming Equations (3.15)-(3.23) into a set of six first-order ordinary differential equations. At these singularities, the radial derivatives become infinite. Hence, in the equations for normal modes (3.15)-(3.23), consider the limit as $d/dr \to \infty$. In this limit, it can be assumed that Q can be neglected in comparision to dQ/dr for any perturbed quantity Q that is differentiated with respect to r. Hence, for non-zero resistivity and zero perpendicular thermal conduction the variables dA'_θ/dr, dA'_z/dr, A'_θ, A'_z, A'_r, v'_r and p' may be neglected in Equations (3.15)-(3.23) to give

$$s\rho' = -\rho\frac{dv'_r}{dr}, \tag{B.1}$$

$$\frac{dp'}{dr} - \frac{ig}{\mu}\frac{dA'_r}{dr} - \frac{B_\theta}{\mu}\frac{d^2A'_z}{dr^2} + \frac{B_z}{\mu}\frac{d^2A'_\theta}{dr^2} = 0, \tag{B.2}$$

$$\frac{d\eta}{dT}\frac{dB_z}{dr}T' - \frac{im\eta}{r}\frac{dA'_r}{dr} + \eta\frac{d^2A'_\theta}{dr^2} = 0, \tag{B.3}$$

$$\eta\frac{d^2A'_z}{dr^2} - ik\eta\frac{dA'_r}{dr} - \frac{1}{r}\frac{d\eta}{dT}\frac{d}{dr}(rB_\theta)T' = 0, \tag{B.4}$$

$$\frac{T'}{T} + \frac{\rho'}{\rho} = 0, \tag{B.5}$$

$$s\rho C_v T' = -p\frac{dv'_r}{dr} - \frac{f^2\kappa_\parallel}{B^2}T' - \left[\mathcal{L} + \rho\left(\frac{\partial\mathcal{L}}{\partial\rho}\right)_T\right]\rho' - \rho\left(\frac{\partial\mathcal{L}}{\partial T}\right)_\rho T' + \frac{2\eta}{\mu}\frac{dB_z}{dr}\left[\frac{d^2A'_\theta}{dr^2} - \frac{im}{r}\frac{dA'_r}{dr}\right]$$

$$+ \frac{2\eta}{r\mu}\frac{d}{dr}(rB_\theta)\left[ik\frac{dA'_r}{dr} - \frac{d^2A'_z}{dr^2}\right] + \frac{1}{\mu}\frac{d\eta}{dT}\left[\left(\frac{dB_z}{dr}\right)^2 + \frac{1}{r^2}\left(\frac{d}{dr}(rB_\theta)\right)^2\right]T'. \tag{B.6}$$

Eliminating all the variables except T' and dp'/dr in Equations (B.1)-(B.6), yields two equations in two unknowns

$$\left\{s\rho\gamma C_v + \frac{f^2\kappa_\parallel}{B^2} + \rho\left(\frac{\partial\mathcal{L}}{\partial T}\right)_\rho - \frac{\rho}{T}\left[\mathcal{L} + \rho\left(\frac{\partial\mathcal{L}}{\partial\rho}\right)_T\right] + \frac{1}{\mu}\frac{d\eta}{dT}\left[\left(\frac{dB_z}{dr}\right)^2 + \frac{1}{r^2}\left(\frac{d}{dr}(rB_\theta)\right)^2\right]\right\}T' = 0, \tag{B.7}$$

$$\frac{dp'}{dr} + \frac{1}{\mu}\frac{d\eta}{dT}\left[\left(\frac{dB_z}{dr}\right)^2 + \frac{1}{r^2}\left(\frac{d}{dr}(rB_\theta)\right)^2\right]T' = 0. \tag{B.8}$$

84

Hence for a non-trivial solution

$$s\rho\gamma C_v + \frac{f^2 \kappa_\parallel}{B^2} + \rho\left(\frac{\partial \mathcal{L}}{\partial T}\right)_\rho - \frac{\rho}{T}\left[\mathcal{L} + \rho\left(\frac{\partial \mathcal{L}}{\partial \rho}\right)_T\right] + \frac{1}{\mu}\frac{d\eta}{dT}\left[\left(\frac{dB_z}{dr}\right)^2 + \frac{1}{r^2}\left(\frac{d}{dr}\left(rB_\theta\right)\right)^2\right] = 0. \quad \text{(B.9)}$$

This is the thermal continuum for non-zero resistivity and zero perpendicular thermal conduction. It should be noted that this method is presented here only as a check that the singularities obtained in Chapter 3 are correct. It is not mathematically rigorous because of the assumption that all of the variables are continuous across the singularity. This is not always the case with, for example, the perturbed total pressure. However, the advantage of this method is that the singularities are obtained relatively quickly and easily compared to the rigorous method described in Chapter 3.

Appendix C

C.1 Description of LEDA

In this Appendix a brief description of LEDA is given. LEDA is the finite element code used in the numerical work in Chapters 3 and 4. One advantage finite elements have over other numerical codes is that they are easy to use once implemented. Any degree of accuracy may be obtained by increasing the number of gridpoints used (combined with accumulation of gridpoints if required).

C.1.1 The Non-dimensional Equations

The eight variables are re-defined as follows

$$v_1 \;=\; rv_r', \qquad v_2 \;=\; -\frac{B}{B_z}v_\perp', \qquad v_3 \;=\; \frac{r}{B}\left(iv_\parallel' + \frac{B_\theta}{B_z}v_\perp'\right), \tag{C.1}$$

$$\hat{\rho} \;=\; r\rho', \qquad \hat{T} \;=\; rT', \qquad a_1 \;=\; iA_r', \qquad a_2 \;=\; rA_\theta', \qquad a_3 \;=\; A_z'. \tag{C.2}$$

In addition to re-defining the variables, the following dimensionless quantities are introduced $\hat{\rho} = R\rho_c\hat{\rho}^*$, $r = Rr^*$, $\hat{T} = RT_c\hat{T}^*$, $k = R^{-1}k^*$, $v_1 = Rv_{Ac}v_1^*$, $v_2 = v_{Ac}v_2^*$, $v_3 = \frac{R}{B_c}v_{Ac}v_3^*$, $T = T_cT^*$, $a_1 = RB_ca_1^*$, $a_2 = R^2B_ca_2^*$, $a_3 = RB_ca_3^*$, $\rho = \rho_c\rho^*$, $B_z = B_cB_z^*$, $B_\theta = B_cB_\theta^*$, $s = v_{Ac}R^{-1}s^*$, $m = m^*$, $g = \frac{B_c}{R}g^*$, $f = \frac{B_c}{R}f^*$, $p = p_cp^*$,

$$\kappa_\parallel^* \;=\; \frac{\tilde{\mu}(\gamma-1)}{\mathcal{R}\rho_cRv_{Ac}}\kappa_\parallel, \quad \kappa_\perp^* \;=\; \frac{\tilde{\mu}(\gamma-1)}{\mathcal{R}\rho_cRv_{Ac}}\kappa_\perp, \quad \eta^* \;=\; \frac{1}{Rv_{Ac}}\eta, \quad \mathcal{L}^* \;=\; \frac{R\tilde{\mu}(\gamma-1)}{\rho_c\mathcal{R}v_{Ac}T_c}\mathcal{L}, \tag{C.3}$$

where

$$p_c \;=\; \frac{B_c^2}{\mu}, \qquad\qquad T_c \;=\; \frac{B_c^2\tilde{\mu}}{\mu\mathcal{R}\rho_c}, \tag{C.4}$$

are reference values (together with ρ_c and B_c) usually associated with values on the cylinder axis. The Equations (3.15)-(3.22) for normal modes in cylindrical geometry then become (asterisks omitted for ease of writing)

$$\frac{s\hat{\rho}}{r} \;=\; -\frac{1}{r}\frac{d}{dr}(\rho v_1) - \frac{\rho m}{r}v_2 - \frac{\rho f}{r}v_3, \tag{C.5}$$

$$\frac{s\rho}{r}v_1 \;=\; -\frac{d}{dr}\left[\frac{p}{rT}\hat{T} + \frac{p}{r\rho}\hat{\rho} - ga_1 - B_\theta\frac{da_3}{dr} + \frac{B_z}{r}\frac{da_2}{dr}\right]$$

$$\qquad -\; \frac{2kB_\theta}{r}a_1 + \frac{kf}{r}a_2 + \frac{2B_\theta}{r}\frac{da_3}{dr} - \frac{mf}{r}a_3, \tag{C.6}$$

$$s\rho rB_\theta v_2 \;=\; \frac{pg}{T}\hat{T} + \frac{pg}{\rho}\hat{\rho} + \frac{mB^2}{r}\frac{da_2}{dr} + kB^2r\frac{da_3}{dr} - B^2r\left(\frac{m^2}{r^2} + k^2\right)a_1$$

$$\qquad +\; \left(\frac{B_\theta B_z}{r} + B_z\frac{dB_\theta}{dr} - B_\theta\frac{dB_z}{dr}\right)(ka_2 - ma_3), \tag{C.7}$$

$$s\rho B_z v_3 = \frac{kp}{T}\hat{T} + \frac{kp}{\rho}\hat{\rho} + \frac{dB_z}{dr}(ka_2 - ma_3) + B_\theta r\left(\frac{m^2}{r^2} + k^2\right)a_1 - \frac{mB_\theta}{r}\frac{da_2}{dr} - krB_\theta\frac{da_3}{dr}, \quad (C.8)$$

$$sa_1 = B_z v_2 + \frac{m\eta}{r^2}\frac{da_2}{dr} - \eta\left(\frac{m^2}{r^2} + k^2\right)a_1 + k\eta\frac{da_3}{dr}, \quad (C.9)$$

$$sa_2 = -B_z v_1 + \eta r\frac{d}{dr}\left[\frac{1}{r}\frac{da_2}{dr}\right] - mr\eta\frac{d}{dr}\left(\frac{a_1}{r}\right) + km\eta a_3 - k^2\eta a_2 + \frac{d\eta}{dT}\frac{dB_z}{dr}\hat{T}, \quad (C.10)$$

$$sa_3 = \frac{B_\theta}{r}v_1 - \frac{k\eta}{r}\frac{d}{dr}(ra_1) + \frac{\eta}{r}\frac{d}{dr}\left(r\frac{da_3}{dr}\right) - \frac{m^2\eta}{r^2}a_3 + \frac{mk\eta}{r^2}a_2 - \frac{1}{r^2}\frac{d\eta}{dT}\frac{d}{dr}(rB_\theta)\hat{T}, \quad (C.11)$$

$$\frac{s\rho}{r}\hat{T} = -\frac{\rho}{r}\frac{dT}{dr}v_1 - (\gamma-1)\frac{p}{r}\frac{dv_1}{dr} - (\gamma-1)\frac{pm}{r}v_2 - (\gamma-1)\frac{pf}{r}v_3$$

$$+ \frac{1}{r}\frac{d}{dr}\left[r\kappa_\perp\frac{d}{dr}\left(\frac{\hat{T}}{r}\right)\right] - \frac{1}{r}\left[\left(\frac{m^2}{r^2} + k^2\right)\kappa_\perp + \frac{f^2}{B^2}(\kappa_\parallel - \kappa_\perp)\right]\hat{T}$$

$$- \frac{1}{r}\left(\mathcal{L} + \rho\left(\frac{\partial\mathcal{L}}{\partial\rho}\right)_T\right)\hat{\rho} - \frac{\rho}{r}\left(\frac{\partial\mathcal{L}}{\partial T}\right)_\rho\hat{T} + \frac{f}{rB^2}(\kappa_\parallel - \kappa_\perp)\frac{dT}{dr}(ka_2 - ma_3)$$

$$+ \frac{1}{r}\frac{d}{dr}\left[\left(\frac{\partial\kappa_\perp}{\partial\rho}\hat{\rho} + \frac{\partial\kappa_\perp}{\partial T}\hat{T} - 2rB_\theta\frac{\partial\kappa_\perp}{\partial B^2}\frac{da_3}{dr} + 2B_z\frac{\partial\kappa_\perp}{\partial B^2}\frac{da_2}{dr} - 2rg\frac{\partial\kappa_\perp}{\partial B^2}a_1\right)\frac{dT}{dr}\right]$$

$$+ 2(\gamma-1)\eta\frac{dB_z}{dr}\left[\frac{km}{r}a_3 - \frac{k^2}{r}a_2 + \frac{d}{dr}\left(\frac{1}{r}\frac{da_2}{dr}\right) - m\frac{d}{dr}\left(\frac{a_1}{r}\right)\right]$$

$$+ 2(\gamma-1)\frac{\eta}{r^2}\frac{d}{dr}(rB_\theta)\left[k\frac{d}{dr}(ra_1) - \frac{d}{dr}\left(r\frac{da_3}{dr}\right) + \frac{m^2}{r}a_3 - \frac{mk}{r}a_2\right]$$

$$+ (\gamma-1)\frac{1}{r}\frac{d\eta}{dT}\left[\left(\frac{dB_z}{dr}\right)^2 + \frac{1}{r^2}\left(\frac{d}{dr}(rB_\theta)\right)^2\right]\hat{T}, \quad (C.12)$$

where all coefficients are now real.

C.1.2 The Matrix Elements

The state vector given by

$$\mathbf{u}^T = \left(\hat{\rho}, v_1, v_2, v_3, \hat{T}, a_1, a_2, a_3\right), \quad (C.13)$$

is introduced and every variable is expanded as a finite linear combination of known expansion functions $h_j(r)\,(1 \leq j < \infty)$, for example

$$u_1 \equiv \hat{\rho} = \sum_{j=1}^{n}\chi_{1j}h_j^1(r), \quad (C.14)$$

where the unknown coefficients $(\chi_{lj})_{l=1,\dots,8}^{j=1,\dots,n}$ are to be found from the differential equations. These expansions are substituted into Equations (C.5)-(C.12) which are then projected onto the basis functions using

$$\langle h_1(r), h_2(r)\rangle \equiv \int_0^R h_1^*(r)h_2(r)\,dr. \quad (C.15)$$

This projection yields a set of $8n$ linear equations for the $8n$ coefficients $(\chi_{lj})_{l=1,\ldots,8}^{j=1,\ldots,n}$ and forms a general matrix eigenvalue problem of the form

$$s\mathbf{B} \cdot \mathbf{X} = \mathbf{A} \cdot \mathbf{X}, \tag{C.16}$$

where $\mathbf{X}$ is the vector containing the coefficients $(\chi_{lj})_{l=1,\ldots,8}^{j=1,\ldots,n}$ and $\mathbf{A}$ and $\mathbf{B}$ are $8n \times 8n$ matrices with n being the number of expansion functions used. Finite elements are used as the expansion functions. These have the property that, for any function $f(r)$,

$$\int f(r)\, h_i(r)\, h_j(r)\, dr = 0 \qquad \forall \; |i - j| > 2. \tag{C.17}$$

Therefore only the sub-blocks which form the main diagonal and it's nearest neighbours contain non-zero elements. Hence the matrices $\mathbf{A}$ and $\mathbf{B}$ possess a tri-diagonal block structure with the matrix $\mathbf{B}$ being symmetrical. The sub-blocks of $\mathbf{A}$ and $\mathbf{B}$ are determined by

$$B_{jl}(1,1) = \int \left[\frac{1}{r}\right] h_j^1 h_l^1 dr, \tag{C.18}$$

$$B_{jl}(2,2) = \int \left[\frac{\rho}{r}\right] h_j^2 h_l^2 dr, \tag{C.19}$$

$$B_{jl}(3,3) = \int [\rho B_z] h_j^3 h_l^3 dr, \tag{C.20}$$

$$B_{jl}(4,4) = \int \left[\frac{\rho B_z}{r}\right] h_j^4 h_l^4 dr, \tag{C.21}$$

$$B_{jl}(5,5) = \int \left[\frac{\rho}{r}\right] h_j^5 h_l^5 dr, \tag{C.22}$$

$$B_{jl}(6,6) = \int [r] h_j^6 h_l^6 dr, \tag{C.23}$$

$$B_{jl}(7,7) = \int \left[\frac{1}{r}\right] h_j^7 h_l^7 dr, \tag{C.24}$$

$$B_{jl}(8,8) = \int [r] h_j^8 h_l^8 dr, \tag{C.25}$$

$$A_{jl}(1,2) = \int \left[-\frac{1}{r}\frac{d\rho}{dr}\right] h_j^1 h_l^2 dr + \int \left[-\frac{\rho}{r}\right] h_j^1 \frac{dh_l^2}{dr} dr, \tag{C.26}$$

$$A_{jl}(1,3) = \int \left[-\frac{m\rho}{r}\right] h_j^1 h_l^3 dr, \tag{C.27}$$

$$A_{jl}(1,4) = \int \left[-\frac{\rho f}{r}\right] h_j^1 h_l^4 dr, \tag{C.28}$$

$$A_{jl}(2,1) = \int \left[\frac{p}{\rho r}\right] \frac{dh_j^2}{dr} h_l^1 dr, \tag{C.29}$$

$$A_{jl}(2,5) = \int \left[\frac{p}{rT}\right] \frac{dh_j^2}{dr} h_l^5 dr, \tag{C.30}$$

$$A_{jl}(2,6) = \int [-g] \frac{dh_j^2}{dr} h_l^6 dr + \int \left[-\frac{2kB_\theta}{r} \right] h_j^2 h_l^6 dr, \tag{C.31}$$

$$A_{jl}(2,7) = \int \left[\frac{kf}{r} \right] h_j^2 h_l^7 dr + \int \left[\frac{B_z}{r} \right] \frac{dh_j^2}{dr} \frac{dh_l^7}{dr} dr, \tag{C.32}$$

$$A_{jl}(2,8) = \int \left[-\frac{fm}{r} \right] h_j^2 h_l^8 dr + \int \left[\frac{2B_\theta}{r} \right] h_j^2 \frac{dh_l^8}{dr} dr + \int [-B_\theta] \frac{dh_j^2}{dr} \frac{dh_l^8}{dr} dr, \tag{C.33}$$

$$A_{jl}(3,1) = \int \left[\frac{pg}{\rho r} \right] h_j^3 h_l^1 dr, \tag{C.34}$$

$$A_{jl}(3,5) = \int \left[\frac{pg}{Tr} \right] h_j^3 h_l^5 dr, \tag{C.35}$$

$$A_{jl}(3,6) = \int \left[-B^2 \left(\frac{m^2}{r^2} + k^2 \right) \right] h_j^3 h_l^6 dr, \tag{C.36}$$

$$A_{jl}(3,7) = \int \left[\frac{k}{r} \left(\frac{B_\theta B_z}{r} + B_z \frac{dB_\theta}{dr} - B_\theta \frac{dB_z}{dr} \right) \right] h_j^3 h_l^7 dr + \int \left[\frac{mB^2}{r^2} \right] h_j^3 \frac{dh_l^7}{dr} dr, \tag{C.37}$$

$$A_{jl}(3,8) = \int \left[-\frac{m}{r} \left(\frac{B_\theta B_z}{r} + B_z \frac{dB_\theta}{dr} - B_\theta \frac{dB_z}{dr} \right) \right] h_j^3 h_l^8 dr + \int \left[kB^2 \right] h_j^3 \frac{dh_l^8}{dr} dr, \tag{C.38}$$

$$A_{jl}(4,1) = \int \left[\frac{kp}{r\rho} \right] h_j^4 h_l^1 dr, \tag{C.39}$$

$$A_{jl}(4,5) = \int \left[\frac{kp}{rT} \right] h_j^4 h_l^5 dr, \tag{C.40}$$

$$A_{jl}(4,6) = \int \left[B_\theta \left(\frac{m^2}{r^2} + k^2 \right) \right] h_j^4 h_l^6 dr, \tag{C.41}$$

$$A_{jl}(4,7) = \int \left[\frac{k}{r} \frac{dB_z}{dr} \right] h_j^4 h_l^7 dr + \int \left[-\frac{mB_\theta}{r^2} \right] h_j^4 \frac{dh_l^7}{dr} dr, \tag{C.42}$$

$$Ajl(4,8) = \int \left[-\frac{m}{r} \frac{dB_z}{dr} \right] h_j^4 h_l^8 dr + \int [-kB_\theta] h_j^4 \frac{dh_l^8}{dr} dr, \tag{C.43}$$

$$A_{jl}(5,1) = \int \left[\frac{1}{r^2} \frac{\partial \kappa_\perp}{\partial \rho} \frac{dT}{dr} - \frac{1}{r} \left(\mathcal{L} + \rho \left(\frac{\partial \mathcal{L}}{\partial \rho} \right)_T \right) \right] h_j^5 h_l^1 dr + \int \left[-\frac{1}{r} \frac{\partial \kappa_\perp}{\partial \rho} \frac{dT}{dr} \right] \frac{dh_j^5}{dr} h_l^1 dr, \tag{C.44}$$

$$A_{jl}(5,2) = \int \left[-\frac{\rho}{r} \frac{dT}{dr} \right] h_j^5 h_l^2 dr + \int \left[-(\gamma-1) \frac{p}{r} \right] h_j^5 \frac{dh_l^2}{dr} dr, \tag{C.45}$$

$$A_{jl}(5,3) = \int \left[(-\gamma-1) \frac{pm}{r} \right] h_j^5 h_l^3 dr, \tag{C.46}$$

$$A_{jl}(5,4) = \int \left[-(\gamma-1) \frac{pf}{r} \right] h_j^5 h_l^4 dr, \tag{C.47}$$

$$A_{jl}(5,5) = \int \left[\frac{1}{r^2} \frac{\partial \kappa_\perp}{\partial T} \frac{dT}{dr} - \frac{\kappa_\perp}{r^3} - \frac{\kappa_\perp g^2}{rB^2} - \frac{\kappa_\parallel f^2}{rB^2} - \frac{\rho}{r} \left(\frac{\partial \mathcal{L}}{\partial T} \right)_\rho \right] h_j^5 h_l^5 dr$$

$$+ \int \left[\frac{1}{r} (\gamma - 1) \frac{d\eta}{dT} \left\{ \left(\frac{dB_z}{dr} \right)^2 + \frac{1}{r^2} \left(\frac{d}{dr} (rB_\theta) \right)^2 \right\} \right] h_j^5 h_l^5 dr$$

$$+ \int \left[\frac{\kappa_\perp}{r^2} \right] h_j^5 \frac{dh_l^5}{dr} dr + \int \left[\frac{\kappa_\perp}{r^2} - \frac{1}{r} \frac{\partial \kappa_\perp}{\partial T} \frac{dT}{dr} \right] \frac{dh_j^5}{dr} h_l^5 dr + \int \left[-\frac{\kappa_\perp}{r} \right] \frac{dh_j^5}{dr} \frac{dh_l^5}{dr} dr, \qquad (C.48)$$

$$A_{jl}(5,6) = \int \left[-\frac{2g}{r} \frac{dT}{dr} \frac{\partial \kappa_\perp}{\partial B^2} + \frac{2m}{r} (\gamma - 1) \left(\eta \frac{d^2 B_z}{dr^2} + \frac{d\eta}{dr} \frac{dB_z}{dr} \right) \right] h_j^5 h_l^6 dr$$

$$+ \int \left[-\frac{2k}{r} (\gamma - 1) \left(\eta \frac{d^2}{dr^2} (rB_\theta) + \frac{d\eta}{dr} \frac{d}{dr} (rB_\theta) - \frac{2\eta}{r} \frac{d}{dr} (rB_\theta) \right) \right] h_j^5 h_l^6 dr$$

$$+ \int \left[2g \frac{dT}{dr} \frac{\partial \kappa_\perp}{\partial B^2} + \frac{2m}{r} (\gamma - 1) \eta \frac{dB_z}{dr} - \frac{2k}{r} (\gamma - 1) \eta \frac{d}{dr} (rB_\theta) \right] \frac{dh_j^5}{dr} h_l^6 dr, \qquad (C.49)$$

$$A_{jl}(5,7) = \int \left[\frac{kf}{rB^2} (\kappa_\parallel - \kappa_\perp) \frac{dT}{dr} - \frac{2k^2}{r} (\gamma - 1) \eta \frac{dB_z}{dr} \right] h_j^5 h_l^7 dr$$

$$+ \int \left[-\frac{2mk\eta}{r^3} (\gamma - 1) \frac{d}{dr} (rB_\theta) \right] h_j^5 h_l^7 dr$$

$$+ \int \left[\frac{2B_z}{r^2} \frac{\partial \kappa_\perp}{\partial B^2} \frac{dT}{dr} - \frac{2}{r} (\gamma - 1) \left(\frac{d\eta}{dr} \frac{dB_z}{dr} + \eta \frac{d^2 B_z}{dr^2} \right) \right] h_j^5 \frac{dh_l^7}{dr} dr$$

$$+ \int \left[-\frac{2B_z}{r} \frac{\partial \kappa_\perp}{\partial B^2} \frac{dT}{dr} - \frac{2}{r} (\gamma - 1) \eta \frac{dB_z}{dr} \right] \frac{dh_j^5}{dr} \frac{dh_l^7}{dr} dr, \qquad (C.50)$$

$$A_{jl}(5,8) = \int \left[-\frac{mf}{rB^2} (\kappa_\parallel - \kappa_\perp) \frac{dT}{dr} + \frac{2m\eta}{r} (\gamma - 1) \left(k \frac{dB_z}{dr} + \frac{m}{r^2} \frac{d}{dr} (rB_\theta) \right) \right] h_j^5 h_l^8 dr$$

$$+ \int \left[\frac{2}{r} (\gamma - 1) \left(\eta \frac{d^2}{dr^2} (rB_\theta) + \frac{d\eta}{dr} \frac{d}{dr} (rB_\theta) - \frac{2\eta}{r} \frac{d}{dr} (rB_\theta) \right) - \frac{2B_\theta}{r} \frac{\partial \kappa_\perp}{\partial B^2} \frac{dT}{dr} \right] h_j^5 \frac{dh_l^8}{dr} dr$$

$$+ \int \left[2B_\theta \frac{\partial \kappa_\perp}{\partial B^2} \frac{dT}{dr} + \frac{2\eta}{r} (\gamma - 1) \frac{d}{dr} (rB_\theta) \right] \frac{dh_j^5}{dr} \frac{dh_l^8}{dr} dr, \qquad (C.51)$$

$$A_{jl}(6,3) = \int [rB_z] h_j^6 h_l^3 dr, \qquad (C.52)$$

$$A_{jl}(6,6) = \int \left[-r\eta \left(\frac{m^2}{r^2} + k^2 \right) \right] h_j^6 h_l^6 dr, \qquad (C.53)$$

$$A_{jl}(6,7) = \int \left[\frac{m\eta}{r} \right] h_j^6 \frac{dh_l^7}{dr} dr, \qquad (C.54)$$

$$A_{jl}(6,8) = \int [rk\eta] h_j^6 \frac{dh_l^8}{dr} dr, \qquad (C.55)$$

$$A_{jl}(7,2) = \int \left[-\frac{B_z}{r} \right] h_j^7 h_l^2 dr, \qquad (C.56)$$

$$A_{jl}(7,5) = \int \left[\frac{1}{r} \frac{d\eta}{dT} \frac{dB_z}{dr} \right] h_j^7 h_l^5 dr, \tag{C.57}$$

$$A_{jl}(7,6) = \int \left[\frac{m}{r} \frac{d\eta}{dr} \right] h_j^7 h_l^6 dr + \int \left[\frac{m\eta}{r} \right] \frac{dh_j^7}{dr} h_l^6 dr, \tag{C.58}$$

$$A_{jl}(7,7) = \int \left[-\frac{k^2\eta}{r} \right] h_j^7 h_l^7 dr + \int \left[-\frac{1}{r} \frac{d\eta}{dr} \right] h_j^7 \frac{dh_l^7}{dr} dr + \int \left[-\frac{\eta}{r} \right] \frac{dh_j^7}{dr} \frac{dh_l^7}{dr} dr, \tag{C.59}$$

$$A_{jl}(7,8) = \int \left[\frac{km\eta}{r} \right] h_j^7 h_l^8 dr, \tag{C.60}$$

$$A_{jl}(8,2) = \int [B_\theta] h_j^8 h_l^2 dr, \tag{C.61}$$

$$A_{jl}(8,5) = \int \left[-\frac{1}{r} \frac{d\eta}{dT} \frac{d}{dr}(rB_\theta) \right] h_j^8 h_l^5 dr, \tag{C.62}$$

$$A_{jl}(8,6) = \int \left[kr \frac{d\eta}{dr} \right] h_j^8 h_l^6 dr + \int [kr\eta] \frac{dh_j^8}{dr} h_l^6 dr, \tag{C.63}$$

$$A_{jl}(8,7) = \int \left[\frac{mk\eta}{r} \right] h_j^8 h_l^7 dr, \tag{C.64}$$

$$A_{jl}(8,8) = \int \left[-\frac{m^2\eta}{r} \right] h_j^8 h_l^8 dr + \int \left[-r \frac{d\eta}{dr} \right] h_j^8 \frac{dh_l^8}{dr} dr + \int [-r\eta] \frac{dh_j^8}{dr} \frac{dh_l^8}{dr} dr, \tag{C.65}$$

where all unmentioned matrix elements are zero. Integration by parts has been used in the radial component of the momentum equation, the energy equation and in the angular and axial components of the induction equation. This yields the following surface terms

$$\left[-\frac{p}{\rho r} \hat{\rho} - \frac{p}{rT} \hat{T} + ga_1 - \frac{B_z}{r} \frac{da_2}{dr} + B_\theta \frac{da_3}{dr} \right]_b (v_1^*)_b, \tag{C.66}$$

$$\left[\frac{1}{r} \frac{dT}{dr} \frac{\partial \kappa_\perp}{\partial \rho} \hat{\rho} + \frac{1}{r} \frac{dT}{dr} \frac{\partial \kappa_\perp}{\partial T} \hat{T} - 2g \frac{dT}{dr} \frac{\partial \kappa_\perp}{\partial B^2} a_1 - \frac{2m(\gamma-1)\eta}{r} \frac{dB_z}{dr} a_1 + \frac{2B_z}{r} \frac{dT}{dr} \frac{\partial \kappa_\perp}{\partial B^2} \frac{da_2}{dr} \right.$$

$$+ \kappa_\perp \frac{d}{dr}\left(\frac{\hat{T}}{r} \right) + \frac{2(\gamma-1)\eta}{r} \frac{dB_z}{dr} \frac{da_2}{dr} + \frac{2kr\eta}{\mu r^2} \frac{d}{dr}(rB_\theta) a_1$$

$$\left. - \left(B_\theta \frac{dT}{dr} \frac{\partial \kappa_\perp}{\partial B^2} + \frac{2(\gamma-1)\eta}{r} \frac{d}{dr}(rB_\theta) \right) \frac{da_3}{dr} \right]_b (\hat{T}^*)_b, \tag{C.67}$$

$$\eta \left[\frac{1}{r} \frac{da_2}{dr} - \frac{ma_1}{r} \right]_b (a_2^*)_b, \tag{C.68}$$

$$\eta \left[r \frac{da_3}{dr} - kra_1 \right]_b (a_3^*)_b. \tag{C.69}$$

The boundary conditions are then applied to these surface terms which are then added to the matrix elements ('natural conditions'). If the boundary conditions require some variable to be zero at the boundary, this needs to be explicitly imposed ('essential conditions'). For more details, see Van der Linden (1991). Also, the projection functions need to be evaluated at the boundaries.

C.1.3   Boundary Conditions

The differential equations (3.15)-(3.23) in Chapter 3 must be supplemented by a set of boundary conditions. In the numerical work the effect of resistivity on the thermal continuum is investigated and hence perpendicular thermal conduction is neglected. This reduces the order of the system of differential equations from eight to six and so six boundary conditions are required. At the centre of the cylinder, the following three regularity conditions are used

$$\lim_{r \to 0} r v_r' \; = \; 0, \qquad \lim_{r \to 0} r A_\theta' \; = \; 0, \qquad A_z' \,|_{r=0} \; = \; 0. \tag{C.70}$$

These ensure that there are no singularities along the axis $r = 0$ of the cylinder. For the external boundary conditions, the plasma is considered to be terminated by a perfectly conducting rigid wall at $r = R$. At first this may be seen to be a bit unrealistic but it has been argued by Goedbloed (1990) that neighbouring coronal loops may act in a similar manner. In any case one may eliminate the influence of this condition by making R sufficiently large. Thus the external boundary conditions used are

$$r v_r' \,|_{r=R} \; = \; 0, \qquad r A_\theta' \,|_{r=R} \; = \; 0, \qquad A_z' \,|_{r=R} \; = \; 0. \tag{C.71}$$

For these rigid wall boundary conditions, the surface terms given by Equations (C.66), (C.68) and (C.69) vanish and the conditions are explicitly implemented by setting the appropriate expansion coefficients equal to zero.

C.1.4   The Finite Elements

An appropriate choice of finite elements now has to be made for each component of $\mathbf{u}\,(r)$. To avoid poor discretisation (Kerner, 1985), cubic Hermite Spline functions are chosen for v_1, a_2 and a_3 and quadratic finite elements for $\hat\rho$, v_2, v_3, $\hat T$ and a_1. The quadratic elements are defined as

$$h_{j,1}^k \,(r) \; = \; \begin{cases} \dfrac{4\,(r - r_{j-1})\,(r_j - r)}{(r_j - r_{j-1})^2} & r \in [r_{j-1}, r_j] \\[4mm] 0 & r \notin [r_{j-1}, r_j], \end{cases} \tag{C.72}$$

$$h_{j,2}^k \,(r) \; = \; \begin{cases} \dfrac{(2r - r_j - r_{j-1})\,(r - r_{j-1})}{(r_j - r_{j-1})^2} & r \in [r_{j-1}, r_j] \\[4mm] \dfrac{(2r - r_{j+1} - r_j)\,(r - r_{r+1})}{(r_{j+1} - r_j)^2} & r \in [r_j, r_{j+1}] \\[4mm] 0 & r \notin [r_{j-1}, r_{j+1}], \end{cases} \tag{C.73}$$

while the cubic elements are defined by

$$h_{j,1}^k \,(r) \; = \; \begin{cases} 3\left(\dfrac{r - r_j}{r_j - r_{j-1}}\right)^2 - 2\left(\dfrac{r - r_{j-1}}{r_j - r_{j-1}}\right)^3 & r \in [r_{j-1}, r_j] \\[5mm] 3\left(\dfrac{r_{j+1} - r}{r_{j+1} - r_j}\right)^2 - 2\left(\dfrac{r_{j+1} - r}{r_{j+1} - r_j}\right)^3 & r \in [r_j, r_{j+1}] \\[5mm] 0 & r \notin [r_{j-1}, r_{j+1}], \end{cases} \tag{C.74}$$

$$h_{j,2}^k(r) = \begin{cases} (r - r_j) \left(\dfrac{r - r_{j-1}}{r_j - r_{j-1}} \right)^2 & r \in [r_{j-1}, r_j] \\[3mm] (r - r_j) \left(\dfrac{r - r_{j+1}}{r_{j+1} - r_j} \right)^2 & r \in [r_j, r_{j+1}] \\[3mm] 0 & r \notin [r_{j-1}, r_{j+1}]. \end{cases} \qquad \text{(C.75)}$$

Since two finite elements are use for each gridpoint, the size of the matrices $\mathbf{A}$ and $\mathbf{B}$ increases to $16n \times 16n$. The general eigenvalue problem (C.16) is then solved by two different algorithms. The first, the QR method (Kerner, 1989) gives all the eigenvalues of the matrix considered and hence an indication of what the spectrum looks like. Once a global view of the spectrum is known, the separate branches and individual modes can then be studied using the Inverse Vector Iteration algorithm (Kerner, 1989) which calculates and plots specific eigenfunctions.

Appendix D

D.1 WKB analysis in the ideal case

In this Appendix, a detailed description of the WKB analysis carried out in Chapter 4 for the ideal case is given. The Gold-Hoyle equilibrium equations (4.13) with $\lambda = 0$ are substituted into the Hain-Lüst equation (4.25) which is then expanded for $r \ll 1$, but $kr \gg 1$, to give

$$\frac{d}{dr}\left[F(r,s)\frac{d\chi}{dr}\right] + G(r,s)\chi = 0, \tag{D.1}$$

where

$$F = \frac{r\left(\frac{1}{2}s^2 + m^2\right)}{(1+r^2)^2\left(m^2+k^2r^2\right)}, \tag{D.2}$$

and

$$G = \frac{1}{r(1+r^2)^2}\left\{-\left(\frac{1}{2}s^2+m^2\right) - 4r^2 + \frac{4m^2k^2r^2}{(m^2+k^2r^2)^2} + \frac{8m^2r^2}{(m^2+k^2r^2)}\right.$$
$$\left. + \frac{4k^2r^2}{(m^2+k^2r^2)\left(\frac{1}{2}s^2+m^2\right)}\left[m^2 + \frac{s^2r^2}{\gamma}\left(1 - \frac{m^2}{\left(\frac{1}{2}s^2+m^2\right)}\right)\right]\right\}. \tag{D.3}$$

Setting $\chi = F^{-\frac{1}{2}}y$, the differential equation (D.1) becomes

$$\frac{d^2y}{dr^2} + \left[\frac{G}{F} + \frac{1}{4F^2}\left(\frac{dF}{dr}\right)^2 - \frac{1}{2F}\frac{d^2F}{dr^2}\right]y = 0. \tag{D.4}$$

After some algebra, it can be shown that

$$\frac{G}{F} + \frac{1}{4F^2}\left(\frac{dF}{dr}\right)^2 - \frac{1}{2F}\frac{d^2F}{dr^2} = \frac{(m^2+k^2r^2)}{r^2}\left[-1 - \frac{4r^2}{\left(\frac{1}{2}s^2+m^2\right)}\right.$$
$$+ \frac{4k^2r^2}{(m^2+k^2r^2)\left(\frac{1}{2}s^2+m^2\right)^2}\left\{m^2 + \frac{s^2r^2}{\gamma}\left(1 - \frac{m^2}{\left(\frac{1}{2}s^2+m^2\right)}\right)\right\}$$
$$+ \frac{4m^2k^2r^2}{(m^2+k^2r^2)^2\left(\frac{1}{2}s^2+m^2\right)} + \frac{8m^2r^2}{(m^2+k^2r^2)\left(\frac{1}{2}s^2+m^2\right)}\right]$$
$$+ \frac{1}{4r^2} + \frac{k^2r^2\left(2m^2-k^2r^2\right)}{r^2\left(m^2+k^2r^2\right)^2} \equiv Q. \tag{D.5}$$

Expanding s as

$$s = s_0 + \frac{s_1}{k} + \frac{s_2}{k^2} + \dots, \tag{D.6}$$

and setting $s_0 = \sqrt{2}$ and $m = 1$, Equation (D.5) becomes

$$Q = \frac{1}{4r^2} + \frac{k^2 r^2 \left(2 - k^2 r^2\right)}{r^2 \left(1 + k^2 r^2\right)^2} + \frac{\left(1 + k^2 r^2\right)}{r^2}\left[-1 - 2r^2 \left(1 - \frac{\sqrt{2}s_1}{2k}\right)\right.$$

$$+ \; \frac{k^2 r^2}{\left(1 + k^2 r^2\right)}\left(1 - \frac{\sqrt{2}s_1}{k}\right)\left\{1 + \frac{r^2}{\gamma}\left(\sqrt{2} + \frac{s_1}{k}\right)^2 \left(1 - \frac{1}{2}\left[1 - \frac{\sqrt{2}s_1}{2k}\right]\right)\right\}$$

$$+ \; \frac{2k^2 r^2}{\left(1 + k^2 r^2\right)^2}\left(1 - \frac{\sqrt{2}s_1}{2k}\right) + \frac{4r^2}{\left(1 + k^2 r^2\right)}\left.\left(1 - \frac{\sqrt{2}s_1}{2k}\right)\right]. \tag{D.7}$$

To leading order in r^2 and s_1, Equation (D.7) becomes

$$Q = \frac{1}{r^2}\left[\frac{-\frac{3}{4} + \frac{5}{2}k^2 r^2 + \frac{1}{4}k^4 r^4}{\left(1 + k^2 r^2\right)^2} + k^2 r^2 \left(-\frac{\sqrt{2}}{k}s_1 - \frac{7}{5}r^2\right)\right]. \tag{D.8}$$

Hence the differential equation (D.4) can be written as

$$\frac{d^2 y}{dr^2} + \left[k^2 q\left(r, s\right) + p\left(r\right)\right] y = 0, \tag{D.9}$$

where

$$q = -\frac{\sqrt{2}}{k}s_1 - \frac{7}{5}r^2, \tag{D.10}$$

and

$$p = \frac{-\frac{3}{4} + \frac{5}{2}k^2 r^2 + \frac{1}{4}k^4 r^4}{r^2 \left(1 + k^2 r^2\right)^2}. \tag{D.11}$$

In Equation (D.10), it can be seen that q predicts a one turning point problem. However, in Equation (D.11), p is singular at $r = 0$, but is negligible elsewhere. This gives a second turning point. Hence this problem is a two turning point problem. The next stage in this calculation is to work out two solutions to the differential equation (D.9), one corresponding to the situation when $k^{\frac{1}{2}}r \ll 1$ and one when $kr \gg 1$. These two solutions are then asymptotically matched to yield a value for s_1.

D.1.1 The solution for $k^{\frac{1}{2}}r \ll 1$

The transformation given by $z = \phi\left(r\right)$ and $v = \psi\left(r\right)y\left(r\right)$ is then applied to the differential equation (D.9), (see Nayfeh, 1973) yielding

$$\frac{d^2 v}{dr^2} + \frac{1}{\left(d\phi/dr\right)^2}\left[\frac{d^2 \phi}{dr^2} - \frac{2}{\psi}\frac{d\psi}{dr}\frac{d\phi}{dr}\right]\frac{dv}{dz} + \frac{1}{\left(d\phi/dr\right)^2}\left[k^2 q + p + \frac{2}{\psi^2}\left(\frac{d\psi}{dr}\right)^2 - \frac{1}{\psi}\frac{d^2 \psi}{dr^2}\right]v = 0. \tag{D.12}$$

Setting $\psi^2 = d\phi/dr$ to eliminate the first derivative term dv/dz, and

$$\left(\frac{d\phi}{dr}\right)^2 = q \quad \Rightarrow \quad z = \int_0^r \sqrt{q\left(\tau\right)}\, d\tau. \tag{D.13}$$

Putting $\left(d\phi/dr\right)^2 = q$ into Equation (D.12) gives

$$\frac{d^2 v}{dz^2} + \left[k^2 - \frac{3}{4z^2}\right]v = W\left(z\right)v, \tag{D.14}$$

where

$$W\left(z\right) = -\frac{3}{4z^2} - \frac{1}{\left(d\phi/dr\right)^2}\left[p + \frac{2}{\psi^2}\left(\frac{d\psi}{dr}\right)^2 - \frac{1}{\psi}\frac{d^2 \psi}{dr^2}\right]. \tag{D.15}$$

Equation (D.14) has the correct form of the singularity at $r = 0$ since W is non singular (see, for example, Heading, 1962; Nayfeh, 1973). This can be seen by letting $r \to 0$

$$W \to \frac{\psi}{q_0} \frac{d}{dr} \left(\frac{1}{\psi^2} \frac{d\psi}{dr} \right). \tag{D.16}$$

Therefore for small r, W is negligible. Hence for $r \ll 1$ Equation (D.14) becomes

$$\frac{d^2 v}{dz^2} + \left[k^2 - \frac{3}{4z^2} \right] v = 0. \tag{D.17}$$

Letting $v = z^{\frac{1}{2}} \alpha(z)$, it is found that the differential equation (D.17) becomes

$$z^2 \frac{d^2 \alpha}{dz^2} + z \frac{d\alpha}{dz} + \left(k^2 z^2 - 1 \right) \alpha = 0. \tag{D.18}$$

Equation (D.18) is Bessel's equation and has a solution

$$\alpha = b_1 J_1(kz) \quad \Rightarrow \quad v = b_1 z^{\frac{1}{2}} J_1(kz), \tag{D.19}$$

where b_1 is an arbitrary constant. Hence, for $r \ll 1/k^{\frac{1}{2}}$, the non singular solution to the differential equation (D.4) is

$$y_1 = \frac{b_1}{q^{\frac{1}{4}}} \left(\int_0^r \sqrt{q(\tau)} \, d\tau \right)^{\frac{1}{2}} J_1 \left(k \int_0^r \sqrt{q(\tau)} \, d\tau \right). \tag{D.20}$$

D.1.2 The solution for $kr \gg 1$

The solution for large kr is obtained next. For $kr \gg 1$ the differential equation (D.9) becomes

$$\frac{d^2 y}{dr^2} + k^2 q y = 0. \tag{D.21}$$

$$\Rightarrow \frac{d^2 v}{dz^2} + \frac{1}{(d\phi/dr)^2} \left[k^2 q - \psi \frac{d}{dr} \left(\frac{1}{\psi^2} \frac{d\psi}{dr} \right) \right] v = 0, \tag{D.22}$$

where $z = \phi(r)$, $v = \psi(r) y(r)$ and $\psi^2 = d\phi/dr$. Letting

$$\frac{k^2 q}{(d\phi/dr)^2} = -z = -\phi, \tag{D.23}$$

and neglecting the term

$$-\psi \frac{d}{dr} \left(\frac{1}{\psi^2} \frac{d\psi}{dr} \right)$$

from Equation (D.22) yields

$$\frac{d^2 v}{dz^2} - z v = 0. \tag{D.24}$$

The differential equation (D.24) is Airy's equation and has a solution given by $v = a_1 \text{Ai}(z)$ where a_1 is an arbitrary constant. Since

$$k^2 q = -\phi \left(\frac{d\phi}{dr} \right)^2 = -\phi \left(\frac{d(-\phi)}{dr} \right)^2,$$

$$\Rightarrow k\sqrt{q} = \sqrt{-\phi} \frac{d(-\phi)}{dr},$$

$$\Rightarrow k \int_{r_1}^{r} \sqrt{q(\tau)} \, d\tau = \frac{2}{3} (-\phi)^{\frac{3}{2}},$$

$$\Rightarrow \phi = -\left[\frac{3}{2} k \int_{r_1}^{r} \sqrt{q(\tau)} \, d\tau \right]^{\frac{2}{3}} = z, \tag{D.25}$$

where r_1 satisfies $q(r_1) = 0$. Hence for $kr \gg 1$ the solution is given by

$$y_2 = \frac{v}{\psi} = a_1 \left[-\frac{z}{k^2 q} \right]^{\frac{1}{4}} \text{Ai}(z), \quad \text{where} \quad z = -\left[\frac{3}{2} k \int_{r_1}^{r} \sqrt{q} \, dz \right]^{\frac{2}{3}}, \tag{D.26}$$

or

$$y_2 = \frac{a_1}{\sqrt{k} q^{\frac{1}{4}}} \left[\left(\frac{3}{2} k \int_{r_1}^{r} \sqrt{q} \, dz \right)^{\frac{2}{3}} \right]^{\frac{1}{4}} \text{Ai} \left(-\left[\frac{3}{2} k \int_{r_1}^{r} \sqrt{q} \, dz \right]^{\frac{2}{3}} \right). \tag{D.27}$$

D.1.3 The asymptotic matching of y_1 and y_2

The arguements of the two solutions y_1 and y_2 are asymptotically expanded to give

$$y_1 \sim \frac{\sqrt{2} b_1}{k^{\frac{1}{2}} q^{\frac{1}{4}} \pi^{\frac{1}{2}}} \sin \left[k \int_0^r \sqrt{q(\tau)} d\tau - \frac{\pi}{4} \right], \tag{D.28}$$

and

$$y_2 \sim \frac{a_1}{k^{\frac{1}{2}} q^{\frac{1}{4}} \pi^{\frac{1}{2}}} \sin \left[k \int_{r_1}^r \sqrt{q(\tau)} d\tau + \frac{\pi}{4} \right]. \tag{D.29}$$

Setting $a_1 = \sqrt{2} b_1 (-1)^n$ and matching, yields

$$k \int_0^{r_1} \sqrt{q(\tau)} d\tau = \left(n + \frac{1}{2} \right) \pi, \tag{D.30}$$

where r_1 is the zero of q given by Equation (D.10). Hence, it can be seen that

$$r_1 = \sqrt{-\frac{5\sqrt{2}}{7k} s_1}, \tag{D.31}$$

where s_1 is negative for r_1 to be real. Using Equation (D.30) it can be shown that

$$s_1 = -\frac{4 \left(n + \frac{1}{2} \right)}{\sqrt{2}} \sqrt{\frac{7}{5}}, \tag{D.32}$$

so that for the fundamental mode $n = 0$,

$$s_1 = -\sqrt{\frac{14}{5}}. \tag{D.33}$$

Thus

$$s = \sqrt{2} - \frac{\sqrt{(14/5)}}{k} + \ldots \tag{D.34}$$

Appendix E

E.1 WKB analysis in the non-ideal case

In this Appendix, the zeroth-order and first-order correction terms to the growth rate found numerically for large k in Chapter 4 for the non-ideal case are obtained analytically. Equation (4.50) can be written as

$$
|\nabla S|^2 = \frac{2\beta p}{r(\gamma-1)C_A C_t}\left\{-\frac{\epsilon\rho}{\beta}\left[(B^2+\gamma p\beta)\frac{dp}{dr}+\frac{2\gamma p B_\theta^2}{r}\right]s^3 \right.
$$
$$
\left. + \frac{\sigma_R \gamma \rho p}{\beta}\left[\frac{2B_\theta^2}{r}+\frac{1}{p}(\beta p+B^2)\frac{dp}{dr}\right]s^2+\frac{\gamma p m^2 B_\theta^2}{r^2}(\sigma_R-\epsilon s)\frac{dp}{dr}\right\}, \tag{E.1}
$$

where

$$
C_A = s^2\rho+\frac{m^2 B_\theta^2}{r^2}, \tag{E.2}
$$

and

$$
C_t = \frac{\epsilon p s}{\gamma-1}\left[s^2\rho\left(\gamma p+\frac{B^2}{\beta}\right)+\frac{\gamma p m^2 B_\theta^2}{r^2}\right]-\left[s^2\rho+\frac{m^2 B_\theta^2}{r^2}\right]p\rho\left(\frac{\partial\widehat{\mathcal{L}}}{\partial\rho}\right)_T
$$
$$
+ \left[\left(\frac{\partial\widehat{\mathcal{L}}}{\partial T}\right)_\rho+\frac{\widehat{R}m^2 B_\theta^2}{r^2 B^2}\right]\left[\frac{m^2 B_\theta^2 p}{r^2}+s^2\rho\left(p+\frac{B^2}{\beta}\right)\right]. \tag{E.3}
$$

Equation (E.2) represents the Alfvén continuum, while Equation (E.3) represents the slow and thermal continua. After some algebra

$$
|\nabla S|^2-\frac{B^2}{B_\theta^2} = \frac{pB_\theta^2}{\beta C_A C_t}\left\{-\frac{\epsilon\rho^2(\gamma\beta p+B^2)B^2}{B_\theta^2(\gamma-1)B_\theta^2}s^5+\frac{\rho^2 B^4}{B_\theta^4}\left[-\left(\frac{\partial\widehat{\mathcal{L}}}{\partial p}\right)_T+\frac{(\beta p+B^2)\gamma}{(\gamma-1)B^2}\sigma_R\right]s^4\right.
$$
$$
- \frac{\epsilon\rho}{r^2(\gamma-1)}\left[\gamma\beta p\left(\frac{B^2 m^2}{B_\theta^2}+4\right)+\frac{(\gamma\beta p+B^2)}{B_\theta^2}\left(m^2 B^2+2r\beta\frac{dp}{dr}\right)\right]s^3
$$
$$
+ \frac{\rho}{r^2}\left[\frac{\gamma\beta p}{(\gamma-1)}\sigma_R\left(\frac{m^2 B^2}{B_\theta^2}+4+\frac{(\beta p+B^2)}{\beta p B_\theta^2}\left(m^2 B^2+2r\beta\frac{dp}{dr}\right)\right)-\frac{B^2}{B_\theta^2}m^2 B^2\left(\frac{\partial\widehat{\mathcal{L}}}{\partial p}\right)_T\right]s^2
$$
$$
- \frac{m^2\gamma\beta p}{(\gamma-1)r^4}\left(m^2 B^2+2r\beta\frac{dp}{dr}\right)(\epsilon s-\sigma_R)\right\}
$$
$$
= q. \tag{E.4}
$$

Notice that the expression in the curly brackets is the same as the dispersion relation given by Equation (4.56). Setting

$$|\nabla S|^2 - \frac{B^2}{B_\theta^2} \;\rightarrow\; -\frac{1}{k^2}\frac{d^2}{dr^2}, \tag{E.5}$$

the following differential equation is obtained

$$\frac{d^2 y}{dr^2} + k^2 q y \;=\; 0. \tag{E.6}$$

A WKB analysis is now performed on Equation (E.6). For further details of WKB theory, see Bender and Orszag (1978). This problem can be reduced to a two turning point problem, as in Appendix D. Hence the Bohr-Sommerfield condition for a two turning point problem is used

$$k \int_0^{r_1} q^{\frac{1}{2}} dr \;=\; \left[n + \frac{1}{2} \right] \pi, \tag{E.7}$$

where n is an integer and r_1 is the zero of q. Substituting the Gold-Hoyle equilibrium equations (4.13) with $\partial\widehat{\mathcal{L}}/\partial p = p_0$, $\partial\widehat{\mathcal{L}}/\partial T = (\alpha - 1)p_0^2$, $\beta = 1$, $\widehat{R} = 0$ and $\alpha = -1$, into Equation (E.4) and then setting $m = 1, \gamma = 5/3$, the following equation for q is obtained

$$q \;=\; \frac{\beta_1}{r^2 \left(1 + r^2\right)\left(s^2\left(1 - \lambda^2\right) + 2\right)\beta_2}, \tag{E.8}$$

where

$$
\begin{aligned}
\beta_1 \;=\; & - \left(1 - \lambda^2\right)\left(r^2 + \lambda^2\right)\left(1 + r^2\right)^3\left(5 + 6r^2 + \lambda^2\right)\epsilon s^5 \\
& + \; 2\left(1 - \lambda^2\right)^2\left(r^2 + \lambda^2\right)\left(1 + r^2\right)^2 s^4 \\
& - \; 2\epsilon\left(1 + r^2\right)^2\left[5\left(1 - \lambda^2\right)\left(1 + r^2\right)\left(5r^2 + \lambda^2\right) + \left(5 + 6r^2 + \lambda^2\right)\left(\lambda^2 + \left(-3 + 5\lambda^2\right)r^2 + r^4\right)\right]s^3 \\
& + \; 4\left(1 - \lambda^2\right)\left[\left(1 - \lambda^2\right)\left(1 + r^2\right)\left(5r^2 + \lambda^2\right) \right. \\
& + \; \left(1 + 2r^2 + \lambda^2\right)\left(\lambda^2 + \left(-3 + 5\lambda^2\right)r^2 + r^4\right) - \left(r^2 + \lambda^2\right)^2\left(1 + r^2\right)\bigr]s^2 \\
& - \; 20\left(1 + r^2\right)^2\left(\lambda^2 + \left(-3 + 5\lambda^2\right)r^2 + r^4\right)\epsilon s + 8\left(1 - \lambda^2\right)\left(\lambda^2 + \left(-3 + 5\lambda^2\right)r^2 + r^4\right),
\end{aligned} \tag{E.9}
$$

and

$$\beta_2 \;=\; \epsilon\left(1 + r^2\right)^2\left(5 + 6r^2 + \lambda^2\right)s^3 - 2\left(1 - \lambda^2\right)\left(1 + r^2\right)s^2 + 10\epsilon\left(1 + r^2\right)^2 s - 4\left(1 - \lambda^2\right). \tag{E.10}$$

E.1.1   WKB analysis for $\lambda = 0$

Setting $\lambda = 0$ in Equation (E.8) yields

$$q \;=\; \frac{\alpha_1}{\left(1 + r^2\right)\left(s^2 + 2\right)\alpha_2}, \tag{E.11}$$

where

$$
\begin{aligned}
\alpha_1 \;=\; & - \left(5 + 6r^2\right)\left(1 + r^2\right)^3\epsilon s^5 + 2\left(1 + r^2\right)^2 s^4 - 4\epsilon\left(1 + r^2\right)^2\left(5 + 6r^2 + 3r^4\right)s^3 \\
& + \; 4\left(2 - r^2 + r^4\right)s^2 - 20\left(1 + r^2\right)^2\left(r^2 - 3\right)\epsilon s + 8\left(r^2 - 3\right),
\end{aligned} \tag{E.12}
$$

and

$$\alpha_2 \;=\; \epsilon\left(1 + r^2\right)^2\left(5 + 6r^2\right)s^3 - 2\left(1 + r^2\right)s^2 + 10\epsilon\left(1 + r^2\right)^2 s - 4. \tag{E.13}$$

Expanding r about $r = 0$ and s about s_0 ($s = s_0 + s_1 + \ldots$) yields

$$\alpha_1 \;=\; (-5\epsilon s_0 + 2)\left(s_0^2 + 6\right)\left(s_0^2 - 2\right) + \chi r^2 + \psi s_1 + O\left(s_1^2, r^4\right), \tag{E.14}$$

where

$$\chi \;=\; -21\epsilon s_0^5 + 4s_0^4 - 64\epsilon s_0^3 - 4s_0^2 + 100\epsilon s_0 + 8, \tag{E.15}$$

and

$$\psi \;=\; -25\epsilon s_0^4 + 8s_0^3 - 60\epsilon s_0^2 + 16s_0 + 60\epsilon. \tag{E.16}$$

The first expression in Equation (E.14) is zero if $s_0 = \sqrt{2}$. Substituting in Equation (E.11) it is found that q becomes

$$q \;=\; \frac{\left(1 - 7\sqrt{2}\epsilon\right) r^2 + \left(2\sqrt{2} - 10\epsilon\right) s_1}{\left(5\sqrt{2}\epsilon - 2\right)}. \tag{E.17}$$

It can be seen that q has a zero r_0 at

$$r_0^2 \;=\; -\left(\frac{2\sqrt{2} - 10\epsilon}{1 - 7\sqrt{2}\epsilon}\right) s_1. \tag{E.18}$$

Substituting Equations (E.17) and (E.18) into the Bohr-Sommerfield condition given by Equation (E.6) and performing the integration gives

$$s_1 \;=\; -\frac{2\left(n + \frac{1}{2}\right)}{k} \sqrt{\left(\frac{14\epsilon - \sqrt{2}}{5\epsilon - \sqrt{2}}\right)}. \tag{E.19}$$

Hence the expansion for s is given by

$$s \;=\; \sqrt{2} - \frac{2\left(n + \frac{1}{2}\right)}{k} \sqrt{\left(\frac{14\epsilon - \sqrt{2}}{5\epsilon - \sqrt{2}}\right)} + \ldots. \tag{E.20}$$

References

An, C. H.: 1986, *Astrophys. J.* **304**, 532.

Appert, K., Gruber, R. and Vaclavik, J.: 1974, *Phys. Fluids* **17**, 147.

Babcock, H. W. and Babcock, H. D.: 1955, *Astrophys. J.* **121**, 349.

Bender, C. M. and Orszag, S. A.: 1978, *Advanced Mathematical Methods for Scientists and Engineers*, McGraw-Hill, New York.

Braginskii, S. I.: 1965, *Rev. Plasma Phys.* **1**, 205.

Bray, R. J. and Loughhead, R. E.: 1964, *Sunspots*, Chapman and Hall, London.

Bray, R. J. and Loughhead, R. E.: 1967, *The Solar Granulation*, Chapman and Hall, London.

Cargill, P. J. and Hood, A. W.: 1989, *Solar Phys.* **124**, 101.

Cargill, P. J., Hood, A. W. and Migliuolos, S.: 1986, *Astrophys. J.* **309**, 402.

Connor, J. W., Hastie, R. J. and Taylor, J. B.: 1979, *Proc. Roy. Soc. London* **A365**, 1.

Cook, J. W., Cheng, C. C., Jacobs, V. L. and Antiochos, S. K.: 1989, *Astrophys. J.* **338**, 1176.

Dewar, R. L. and Glasser, A. H.: 1983, *Phys. Fluids* **26**, 3039.

Dunn, R. B.: 1960, Ph.D. Thesis, Harvard University.

Einaudi, G. and Van Hoven, G.: 1981, *Phys. Fluids* **24**, 1092.

Einaudi, G. and Van Hoven, G.: 1983, *Solar Phys.* **88**, 163.

Engvold, O.: 1976, *Solar Phys.* **49**, 283.

Engvold, O., Tandberg-Hanssen, E. and Reichmann, E.: 1985, *Solar Phys.* **96**, 35.

Field, G. B.: 1965, *Astrophys. J.* **142**, 531.

Foukal, P.: 1971a, *Solar Phys.* **19**, 59.

Foukal, P.: 1971b, *Solar Phys.* **20**, 298.

Goedbloed, J. P.: 1983, *Lecture Notes on Ideal Magnetohydrodynamics*, Rijnhuizen Report 83-145.

Goedbloed, J. P.: 1984, *Physica* **12D**, 107.

Goedbloed, J. P.: 1990, *Comp. Phys. Comm.* **59**, 39.

Goedbloed, J. P. and Sakanaka, P. H.: 1974, *Phys. Fluids* **17**, 908.

Gold, T. and Hoyle, F.: 1960, *Monthly Notices Roy. Astron. Soc.* **120**, 89.

Goossens, M., Poedts, S. and Hermans, D.: 1985, *Solar Phys.* **102**, 51.

Grad, H.: 1973, *Proc. Natl. Acad. Sci. USA* **70**, 3277.

Hain, K. and Lüst, R.: 1958, *Naturforsch* **13a**, 936.

Hardie, I. S., Hood, A. W. and Allen, H. R.: 1991, *Solar Phys.* **133**, 313.

Heading, J.: 1962, *An Introduction to Phase-Integral Methods*, Methuen, London.

Henshaw, D. and Henshaw, P.: 1990, *Apex: the inside story of the Hillman Imp*, Bookmarque Publishing, Minster Lovell, Oxford.

Hermans, D., Goossens, M., Kerner, W. and Lerbinger, K.: 1988, *Phys. Fluids* **31**, 547.

Heyvaerts, J.: 1974, *Astron. Astrophys.* **34**, 65.

Holingsworth, M.: 1994, Imp Club Magazine, April.

Hollweg, J. V.: 1987a, *Astrophys. J.* **312**, 880.

Hollweg, J. V.: 1987b, *Astrophys. J.* **320**, 875.

Hood, A. W.: 1986a, *Solar Phys.* **103**, 329.

Hood, A. W.: 1986b, *Solar Phys.* **105**, 307.

Hood, A. W., Van der Linden, R. A. M. and Goossens, M.: 1989, *Solar Phys.* **120**, 261.

Ionson, J. A.: 1978, *Astrophys. J.* **226**, 650.

Ireland, R. C., Van der Linden, R. A. M., Hood, A. W. and Goossens, M.: 1992, *Solar Phys.* **142**, 265.

de Jager, C.: 1959, *Handbuch der Physik* **52**, 80.

Kerner, W.: 1989, *J. of Comp. Phys.* **85**, 1.

Kerner, W., Lerbinger, K., Gruber, R. and Tsunematsu, T.: 1985, *Comp. Phys. Comm.* **36**, 225.

Kim, I. S.: 1990, in Ruždjak, V. and Tandberg-Hanssen, E. (eds), *Dynamics of Quiescent Prominences*, Springer-Verlag, Berlin Heidelberg, Germany.

Leighton, R. B., Noyes, R. W. and Simon, G. W.: 1962, *Astrophys. J.* **135**, 474.

Leroy, J. L.: 1977, *Astron. Astrophys.* **60**, 79.

Leroy, J. L., Bommier, V. and Sahal-Brechot, S.: 1983, *Solar Phys.* **83**, 135.

Leroy, J. L., Bommier, V. and Sahal-Brechot, S.: 1984, *Astron. Astrophys.* **131**, 33.

Llewellyn, R.: 1994, Imp Club Magazine, June.

Malville, J. M.: 1976, *Solar Phys.* **50**, 79.

Martin, S. F.: 1990, in Ruždjak, V. and Tandberg-Hanssen, E. (eds), *Dynamics of Quiescent Prominences*, Springer-Verlag, Berlin Heidelberg, Germany.

McWhirter, R. W. P., Thonemann, P. C. and Wilson, R.: 1975, *Astron. Astrophys.* **40**, 63.

Menzel, D. H. and Evans, J. W.: 1953, *Accad. Naz. Lincei. Convegno Volta* **11**, 119.

Michard, R.: 1974, in Athay, R. G. (ed), *Chromospheric Fine Structure*, IAU Symposium No. 56, D. Reidel Publ. Co., Dordrecht, Holland.

Millington, T. C.: 1989, *Hillman Imps: tuning-overhaul-servicing*, Bookmarque Publishing, Minster Lovell, Oxford.

NAG Ltd.: 1988, *The NAG Fortran Library Manual-Mark 13*, Numerical Algorithms Group, Oxford.

Nayfeh, A. H.: 1973, *Perturbation Methods*, John Wiley and Sons, New York, 339.

Orrall, F. Q. and Zirker, J. B.: 1961, *Astrophys. J.* **134**, 72.

Parker, E. N.: 1953, *Astrophys. J.* **117**, 431.

Poedts, S., Goossens, M. and Kerner, W.: 1989, *Solar Phys.* **123**, 83.

Poedts, S., Goossens, M. and Kerner, W.: 1990, *Astrophys. J.* **360**, 279.

Prata, S. W.: 1971, *Solar Phys.* **20**, 310.

Priest, E. R.: 1982, *Solar Magnetohydrodynamics*, D. Reidel Publ. Co., Dordrecht, Holland.

Raadu, M. A.: 1972, *Solar Phys.* **22**, 425.

Raymond, J. C. and Smith, B. W.: 1977, *Astrophys. J. Suppl.* **35**, 419.

Rosner, R., Tucker, W. H. and Vaiana, G. S.: 1978, *Astrophys. J.* **220**, 643.

Rust, D. M.: 1967, *Astrophys. J.* **150**, 313.

Sakurai, T., Goossens, M. and Hollweg, J. V.: 1990, *Solar Phys.* **133**, 227.

Schmidt, H. U.: 1974, in Athay, R. G. (ed), *Chromospheric Fine Structure*, IAU Symposium No. 56, D. Reidel Publ. Co., Dordrecht, Holland.

Schmieder, B.: 1990, in Ruždjak, V. and Tandberg-Hanssen, E. (eds), *Dynamics of Quiescent Prominences*, Springer-Verlag, Berlin Heidelberg, Germany.

Schmieder, B., Poland, A. I., Thompson, B. and Démoulin, P.: 1988, *Astron. Astrophys.* **197**, 281.

Simon, G. W. and Leighton, R. B.: 1964, *Astrophys. J.* **140**, 1120.

Simon, G., Schmieder, B., Démoulin, P. and Poland, A. I.: 1986, *Astron. Astrophys.* **166**, 319.

Tandberg-Hanssen, E.: 1974, *Solar Prominences*, D. Reidel Publ. Co., Dordrecht, Holland.

Tandberg-Hanssen, E. and Anzer, U.: 1970, *Solar Phys.* **15**, 158.

Van der Linden, R. A. M.: 1991, Ph.D. Thesis, Katholieke Universiteit Leuven.

Van der Linden, R. A. M.: 1993, *Geophys. Astrophys. Fluid Dynamics* **69**, 183.

Van der Linden, R. A. M. and Goossens, M.: 1991, *Solar Phys.* **134**, 247.

Van der Linden, R. A. M., Goossens, M. and Goedbloed, J. P.: 1991, *Phys. Fluids B* **3**, 866.

Van der Linden, R. A. M., Goossens, M. and Hood, A. W.: 1988, *Solar Phys.* **115**, 235.

Van der Linden, R. A. M., Goossens, M. and Hood, A. W.: 1992, *Solar Phys.* **140**, 317.

Velli, M. and Hood, A. W.: 1986, *Solar Phys.* **106**, 353.

Velli, M. and Hood, A. W.: 1987, *Solar Phys.* **109**, 351.

Wormell, T. W.: 1936, *Mon. Not R.A.S.* **96**, 736.

Zirker, J. B.: 1989, *Solar Phys.* **119**, 341.

Zirker, J. B. and Koutchmy, S.: 1990, *Solar Phys.* **127**, 109.